Observation of selective enhancement of the capture of ultracold neutrons by nuclei

S. S. Arzumanov, L. N. Bondarenko, E. I. Korobkina, V. I. Morozov, Yu. N. Panin, A. I. Fomin, S. M. Chernyavskiĭ, and S. V. Shilkin
Kurchatov Institute Russian Science Center, 123182 Moscow, Russia

P. Geltenbort and W. Drexel
Institute Laue–Langevin, 38042 Grenoble Cedex 9, France

J. Pendlebury
University of Sussex, Brighton BN1 9QH, Sussex, U.K.

K. Schreckenbach
Technical University, D-85747 Garching, Germany

(Submitted 22 November 1996)
Pis'ma Zh. Éksp. Teor. Fiz. **65**, No. 1, 3–8 (10 January 1997)

The subbarrier reflection of ultracold neutrons (UCNs) from stainless steel (an alloy of iron, nickel, chromium, and titanium) is investigated by means of neutron-radiation analysis. It is found that the increase in the probability of capture of UCNs by nuclei is large compared to the standard theory. The effect is selective, the enhancement factor varying From 3 for iron to 90 for titanium. © *1997 American Institute of Physics.* [S0021-3640(97)00101-1]

PACS numbers: 78.70.Nx, 28.20.−v

We have investigated the capture of ultracold neutrons (UCNs) during their subbarrier reflection from the surface of a multicomponent medium. The measurements were made by the method of neutron-radiation analysis with the use of UCNs.[1] This method makes it possible to determine both the partial capture probabilities for different nuclei and the inelastic scattering probability.

For media containing several elements j uniformly distributed over the volume with a relative nuclear concentration c_i, the total interaction probability of UCNs with the surface is the sum of the partial capture probabilities μ_c^I for a specific element of the medium and the inelastic scattering probability μ_{ie}:

$$\mu = \mu_{ie} + \sum_{i=1}^{j} \mu_c^i, \tag{1}$$

where $\mu_{ie} = \eta_{ie} f(v)$ and $\mu_c^i = \eta_c^i f(v)$ are given by the relations

$$f(v) = 2y^{-2}[\sin^{-1}(y) - y\sqrt{1-y^2}], \quad \eta_{ie} = k\sigma_{ie}/4\pi\overline{b}, \quad \eta_c^i = k\sigma^i c_i/4\pi\overline{b}.$$

Here v is the neutron velocity, $y = v/v_{\lim}$, $v_{\lim} = \sqrt{2E_{\lim}/m}$ is the limiting velocity in the medium, m is the neutron mass, $E_{\lim} = 2\pi\hbar^2 Nb/m$ is the limiting energy in the medium,

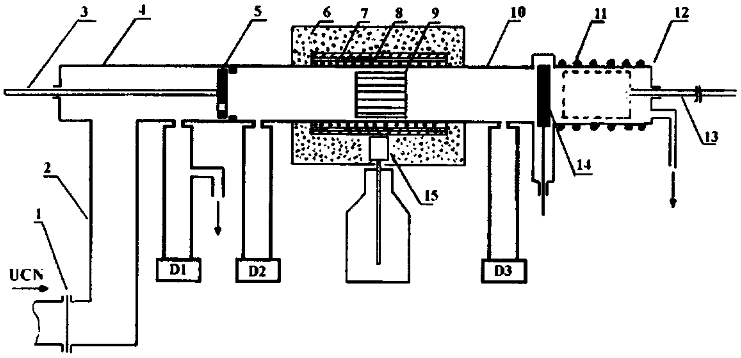

FIG. 1. Diagram of the apparatus: *1* — Al entrance foil, *2* — vertical neutron guide, *3* — rod, *4* — entrance chamber, *5* — movable entrance diaphragm, *6* — lead shield, *7* — B^{10} converter, *8* — casing with a heater and heat screen, *9* — sample, *10* — UCN vessel, *11* — heater, *12* — annealing chamber, *13* — rod for moving the sample, *14* — vacuum slide valve, *15* — Ge(Hp) detector, D_1, D_2, D_3 — UCN detectors.

N is the number of nuclei per unit volume, $\overline{b} = \Sigma_{i=1}^{j} c_i b_i$ is the composition-averaged coherent-scattering length, b_i is the coherent scattering length for the ith element, averaged over the natural isotope abundances, k is the wave number, σ_{ie} is the inelastic scattering cross section, and σ_c^i is the capture cross section for the ith element, averaged over the natural isotope abundances.

The sample, made of electropolished 1Kh18N9T stainless steel foil 200 μm thick, was in the form of a helix 10 cm wide, with an outer diameter of 8 cm. The total area S of the sample was equal 3120 cm^2. A diagram of the apparatus is displayed in Fig. 1. The sample was irradiated with UCNs in a cylindrical stainless steel vessel 112 cm long and 8.8 cm in diameter. Neutrons from an UCN source entered the vessel along a vertical neutron guide either through an entrance diaphragm with an opening with area $S_0 = 0.785$ cm^2 or, when the diaphragm was removed, through the entire cross section of the vessel. The spectrum of the UCN flux in the vessel was concentrated in the range from 0 to 4.4 m/s, with an average velocity of $\overline{v} = 3.8(2)$ m/s. The UCN flux density inside and at the entrance of the vessel was measured with the aid of three slotted proportional detectors D_1, D_2, and D_3, connected to the vessel via an opening with area $S_0 = 0.785$ cm^2. The γ rays produced as a result of the capture of UCNs on the surface of the sample were detected with a Ge(Hp) detector with a resolution of 2 keV for 1-MeV γ rays. The elastically scattered UCNs were detected with the aid of a 1-cm thick B^{10} converter placed between the vessel and the entrance window of the detector. A Li^7 nucleus in the excited state is formed with probability 0.96 in the reaction $n + B^{10} = \alpha + Li^7$ and emits a 477-keV γ-ray which is detected by the detector.

For measuring the background or degassing the sample, the sample was removed from the vessel and placed in a special chamber separated from the vessel by a vacuum slide valve. A vacuum of $2 \cdot 10^{-5}$–$5 \cdot 10^{-6}$ torr was maintained in the vessel, and the vacuum in the chamber was $\approx 10^{-3}$ torr. For measurements of the total loss factor the UCNs entered the vessel through a diaphragm. The quantity

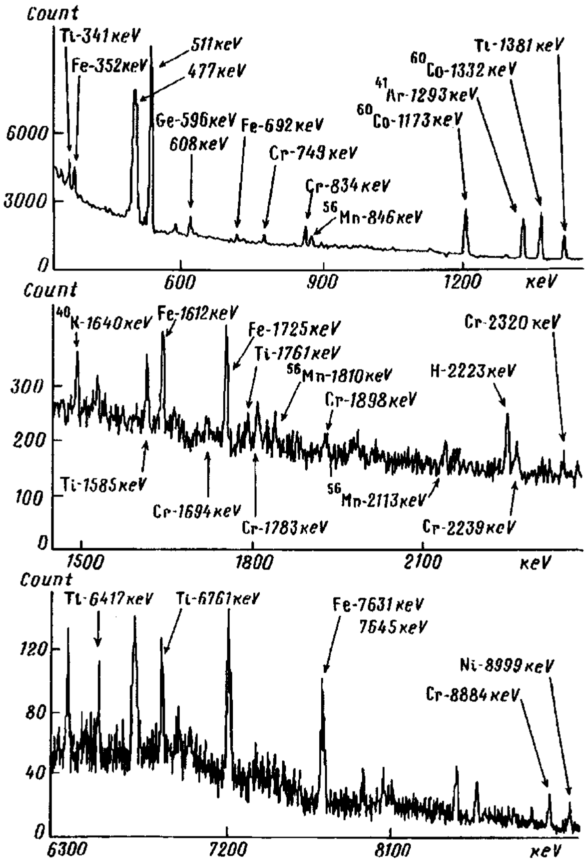

FIG. 2. Fragments of the γ-ray spectrum produced during the irradiation of the sample with ultracold neutrons.

$$\overline{\mu}S+\overline{\mu_t}S_t=\frac{2(J_1-2J_2-J_3)}{(J_2+J_3)}, \tag{2}$$

was determined from the counting rates J_1, J_2, and J_3 of the detectors D_1, D_2, and D_3.

Here $\overline{\mu}$ and $\overline{\mu_t}$ are the total loss factors, averaged over the UCN flux, for the surface of the sample and the vessel, respectively, and S_t is the area of the vessel. The quantity $\overline{\mu_t}S_t$ was determined with the sample removed from the vessel. The value of $\overline{\mu}$ for the sample was calculated by the difference method as the result of two measurements.

To measure the inelastic scattering probability and the partial capture coefficients of the UCNs the diaphragm was removed, permitting the UCNs to enter the vessel through the entire cross section. The flux-averaged value of the inelastic scattering probability was determined as

$$\overline{\mu_{ie}}=\frac{2J_{ie}S_0\epsilon}{(J_2+J_3)S\epsilon_{ie}}, \tag{3}$$

where J_{ie} is the counting rate in the total absorption peak of the 477-keV γ rays, ϵ_{ie} is the detection efficiency for UCNs scattered inelastically by the sample surface and detected according to the counting rate J_{ie}, and ϵ is the detection efficiency for UCNs which have passed through the entrance openings of the detectors. The ratio ϵ_{ie}/ϵ was determined in an additional measurement with a polyethylene reference sample.

The flux-averaged UCN capture probability for the ith element was determined as

$$\overline{\mu_c^i}=\frac{2J_i(E)\epsilon S_0}{(J_2+J_3)S\epsilon_\gamma(E)\beta_i}, \tag{4}$$

where $J_i(E)$ is the counting rate in the total-absorption peak of γ rays with energy E, β_i is the yield of photons with energy E per neutron capture event for the natural isotope abundance of the ith element, and $\epsilon_\gamma(E)$ is the detection efficiency of γ rays with energy E which are emitted from the surface of the sample. The energy dependence of the ratio $\epsilon_\gamma(E)/\epsilon$ was determined in additional measurements performed with polyethylene, titanium, and aluminum reference samples.

For measurement of the inelastic scattering probability and the partial capture coefficients of the UCNs the diaphragm was removed, permitting the UCNs to enter through the entire cross section of the vessel.

The measurements were performed after the sample surface was chemically cleaned by acid etching in H_3PO_4 and vacuum annealing at 100 K for 2 h. Fragments of the γ-ray spectra are displayed in Fig. 2. Total absorption peaks for 477-keV and 2.22-MeV γ rays, which are due to inelastic scattering and capture of UCNs on surface hydrogen, are seen in the spectrum. Peaks due to the capture of UCNs by nuclei of constituent elements of the stainless steel are also present in the spectrum. The spectra obtained were analyzed with allowance for the external γ-ray background and the γ-ray background due to the interaction of UCNs with the surface of the vessel.

The measurements yielded the following values: $\overline{\mu}=6.44(57)\cdot 10^{-4}$, $\overline{\mu}=1.57(26)\cdot 10^{-4}$, and $\overline{\mu_c^H}=2.2(3.8)\cdot 10^{-6}$. The total $(\overline{\mu})$ and combined $(\overline{\mu_{ie}}+\overline{\mu_c^H})$ probabilities differ by the amount $4.85(62)\cdot 10^{-4}$, which determines the combined UCN capture probability for elements other than hydrogen.

Direct measurements of the partial capture probabilities were performed according to the strongest γ transitions accompanying the capture of UCNs by Fe, Ni, Cr, and Ti isotopes. To compare with the theory, the values of the parameters $\eta_c^i=\overline{\mu_c^i}/f(v)$ in the approximation $f(v)=f(\overline{v})=0.96$ were determined from the values obtained for $\overline{\mu_c^i}$ The results are presented in Table I.

The observed enhancement could have been due to an admixture of neutrons with $v \geqslant v_{\mathrm{lim}}=6$ m/s in the UCN spectrum for stainless steel. These neutrons could have increased the partial capture probabilities as a result of above-boundary penetration of UCNs into the volume of the sample. Control measurements for a copper sample with $v_{\mathrm{lim}}=5.65$ m/s showed that the experimental value of μ_c^{Cu} is not more than 2–2.5 times greater than the theoretical value. If this excess is due to neutron penetration into the

TABLE I. Results of measurements of $\overline{\mu_c^i}$ and calculations of η_c^i.

Element	Ni	Ti	Fe	Cr
$\overline{\mu_c^i}\cdot 10^4$	0.83(10)	1.23(4)	1.74(1)	1.19(9)
$\eta_c^i\cdot 10^4$, experiment	0.86(11)	1.28(5)	1.81(11)	1.24(10)
$\eta_c^i\cdot 10^4$, theory	0.128	0.014	0.60	0.207
Ratio of experiment/theory	6.7	91	3	6

copper sample, then for stainless steel this effect can explain in part the increase in the capture by Fe, but it will have little effect on the observed enhancement for other elements. One can see from Table I that $\Sigma_{i=1}^4 \overline{\mu_c^i} = 4.99(18)\cdot 10^{-4}$, which agrees with independent measurements of $\overline{\mu}$, $\overline{\mu_{ie}}$, and $\overline{\mu_c^H}$ A comparison of the experimental and theoretical values of η_c^i shows that the experimental capture probabilities are much higher than the theoretical values. The enhancement effect is selective and is strongest for titanium.

The hypothesis that a titanium-enriched layer is present on the surface is likewise not confirmed. Since $b < 0$ for titanium, in such a model the potential at the surface consists of a potential well in front of a positive step of height E_{lim}. In this case a substantial enhancement of UCN capture by titanium nuclei could be possible. To check this possibility, an elementary analysis was performed of the volume of the sample (Table II) and the surface layer of the sample by the following methods: 1) volume neutron-radiation analysis, 2) x-ray-fluorescence analysis to a depth of 50 μm, 3) x-ray spectral electron microprobe analysis to a depth of 1 μm, and 4) x-ray photoelectron spectrometry to depth $\leqslant 100$ Å.

According to the data obtained by the first three methods, the content of the main elements corresponds to 1Kh18N9T steel, for which the values of η_c^i were calculated. No tendency for the Ti content to increase with increasing depth of the analyzed layer is seen. Furthermore, when the depth of the layer is of the order of the wavelength of the UCNs, the absolute content of Ti and the other constituent elements of the stainless steel is less than the volume content on account of the presence of oxygen and carbon atoms (data of method 4) and also of hydrogen atoms, to which method 4 is insensitive. The ratio of the Ti, Fe, Ni, and Cr concentrations corresponds to the volume ratio.

The smallness of the average titanium concentration at the surface does not rule out the existence of regions with a high titanium concentration. One possible explanation is that the titanium forms clusters emerging at the surface, with a size exceeding the wavelength of the UCNs. Then the neutrons pass freely into the clusters and move in them, reflecting From the boundaries, until they are captured or go back into the vacuum. If Fe, Ni, and Cr nuclei are present in the clusters, then the UCNs will also be efficiently captured by them. Clusters can also be formed in a subsurface layer by closed titanium pores, in which bound states are possible. When the energy of the UCNs equals the resonance energy, then the neutrons can, with a high probability, tunnel into the pores and be captured.

The observed enhancement shows that the standard theory of capture of UCNs does

TABLE II. Results of the elemental analysis of the sample.

Element	Ti	Fe	Ni	Cr	Si	C	O
Content, at.% by method 1	0.7	70.6	8.7	20			
Content, at.% by method 2	0.6	70.7	8.3	20.4			
Content, at.% by method 3	0.7	69.5	8.5	19.7	1.6		
Content, at.% by method 4	0.3	32.4	4.2	11.3		28.8	23.0

not always adequately describe this process for a real multicomponent medium. Further investigations in this area could be crucial for explaining the phenomenon of anomalously high UCN losses during storage in vessels and for performing precise measurements of the neutron lifetime using UCNs.

We are deeply grateful to S. T. Belyaev for assisting in the organization of this work and for some stimulating discussions of the results. We thank Professor A. Steirl for critical and helpful discussions.

We thank G. Just for assisting in the experiment, A. K. Churakov for providing the program for analyzing the γ-ray spectra, and S. A. Terin for performing the elemental analysis of the samples.

This work was performed with the support of the European Foundation INTAS (Grant 93-298), the Russian Fund for Fundamental Research (Grant 96-02-18528-a), and the Foundation for the Support of Young Researchers of the Kurchatov Institute Russian Science Center (Grant 20).

[1] S. V. Zhukov, V. L. Kuznetsov, V. I. Morozov *et al.*, JETP Lett. **57**, 464 (1993).

Translated by M. E. Alferieff

On phase ordering behind the propagating front of a second-order transition

T. W. B. Kibble
Blackett Laboratory, Imperial College, London SW7 2BZ, United Kingdom

G. E. Volovik
Low Temperature Laboratory, Helsinki University of Technology, 02150 Espoo, Finland; L. D. Landou Institute for Theoretical Physics, Russian Academy of Sciences, 117940 Moscow, Russia

(Submitted 9 December 1996)
Pis'ma Zh. Éksp. Teor. Fiz. **65**, No. 1, 96–101 (10 January 1997)

In a real system the heating is nonuniform, and a second-order phase transition to a broken-symmetry phase occurs by propagation of a temperature front. Two parameters, the cooling rate τ_Q and the transition front velocity v_T determine the nucleation of topological defects. Depending on the relation of these parameters, two regimes are found: in the regime of fast propagation defects are created according to the Zurek scenario for the homogeneous case, while in the slow-propagation regime vortex formation is suppressed. © *1997 American Institute of Physics.* [S0021-3640(97)01801-X]

PACS numbers: 11.27.+d, 67.40.Vs, 67.57.Fg, 98.80.Cq

1. INTRODUCTION

A common issue of particular interest both in cosmology and in condensed matter physics is the estimation of the initial defect density produced during a phase transition to a broken-symmetry state.[1,2] In cosmology this is an important issue so far as the later transitions are concerned—for example, in extended models where there are stable defects produced at the electroweak transition. It is probably not of much practical importance for the GUT transition (if our ideas about scaling are correct) because in that case so much time has elapsed that no trace of the initial conditions remains.[3,4] The same thing is true no doubt for some condensed matter systems, but it would be good to identify some situations in which predictions about the initial density (not just the later scaling value) could be tested. We really need to find cases (i) in which the transition is second-order, (ii) in which it is of first order and goes by bubble nucleation, and (iii) in which it goes by the 'false vacuum' becoming totally unstable, which has been called spinodal decomposition. All these cases correspond to different scenarios of the phase ordering below the phase transition, and the creation and evolution of the defects prior to the final establishment of long-range order (phase coherence, or generally the coherence of the Goldstone variables).

The great thing about superfluid helium-3 is that it allows such a wide range of possibilities. Most of these cases, or possibly all of them, may be represented in different regions of the parameter space: the normal ^{3}He to ^{3}He-B or normal ^{3}He to ^{3}He-A tran-

© 1997 American Institute of Physics

sition is second-order, while the A-to-B transition is first-order and proceeds in different ways depending on the pressure (and magnetic field) and the extent of supercooling.[5] Also, of course, it adds another example to the list of possible systems, including nematics,[6] helium-4 (Ref. 7), and high- and low-temperature superconductors, but this example is in important ways more relevant, since the fermion–boson interaction in ^{3}He shares many properties of the quantum field theory in high-energy physics.[8] This is why it is so valuable as an analog of the early universe.

One of the most interesting experiments, which can shed light on the phase ordering is the''mini Big Bang'' produced by thermal neutrons.[9,10] There the exothermic nuclear reaction $n+{}^3_2\mathrm{He}\rightarrow p+{}^3_1\mathrm{H}+0.76$ MeV produces a local Big Bang in ^{3}He-B—a region of high temperature, $T>T_c$, where the symmetry is restored. The subsequent cooling of this region back through the second-order superfluid transition results in the creation of a network of vortex lines. These seeds of vortex lines are grown by the applied rotation and measured with the NMR technique.[9]

Theoretically, the formation of defects in a second-order transition into a broken-symmetry state, discussed in Refs. 1 and 2, corresponds to a homogeneous phase transition. In real experiments the heating is never uniform. For example, in the neutron experiments the heating above T_c by the neutron and the subsequent cooling occur locally in a region of about 10 μm size. This results in a temperature gradient and thus in a propagating boundary of the second-order transition. The temperature gradient is present also in other experiments where defect formation is influenced by the details of the cooling through T_c; see, e.g., Ref. 11, where the type of ^{3}He-A vortices created depends on the cooling rate. One might think that the phase of the order parameter would be determined by the ordered state behind the propagating boundary and that vortex formation would be suppressed in this geometry. On the other hand, in the limit of very rapid motion of the boundary one comes to the situation of an instantaneous transition, and the Kibble–Zurek mechanism should be restored. Here we discuss the criterion on the propagation velocity of a second-order phase transition which separates the two regimes. We shall illustrate it with the example of the experimentally studied transitions from normal ^{3}He to ^{3}He-A and from normal ^{3}He to ^{3}He-B.

2. PHASE ORDERING IN A SPATIALLY HOMOGENEOUS TRANSITION

A nonequilibrium phase transition into the state in which the symmetry $U(1)$ is broken leads to the formation of an infinite cluster of the topological defects—vortices or strings.[1] As a result, when the temperature crosses T_c two length scales appear. One of them is the conventional coherence length, which diverges at T_c:

$$\xi\approx\xi_0\left(1-\frac{T}{T_c}\right)^{-\nu} \tag{2.1}$$

(for superfluid ^{3}He, where the Ginzburg–Landau theory is valid, one has $\nu=1/2$). Another one is the mean distance $\tilde{\xi}$ between the vortices in the infinite cluster; it defines the scale within which the phase of the order parameter is correlated. This scale diverges with time when the vortex cluster decays. We are interested in estimation of the initial defect density $\tilde{\xi}_{\mathrm{initial}}$, i.e., at the moment when these two scales become well defined.

According to Zurek,[2] $\tilde{\xi}_{\text{initial}}$ is determined by the cooling rate τ_Q, which characterizes the time dependence of the temperature in the vicinity of the phase transition:

$$\epsilon(t) \equiv 1 - \frac{T(t)}{T_c} \approx \frac{t}{\tau_Q}. \tag{2.2}$$

Well-defined vortices are formed at the time when the regions within the Ginzburg–Landau coherence length become causally connected. Causal connection is established by the propagation of the order parameter. In the case of superfluid ^{3}He the propagation velocity of the order parameter can be estimated as the velocity of spin waves, which just represent the propagating oscillations of some components of the order parameter. Thus one has that the corresponding velocity also depends on time and is given by

$$c(t) \approx c_0 \epsilon^{1/2}(t), \tag{2.3}$$

where c_0 is of order of the Fermi velocity $v_F \sim 10^4$ cm.

At the moment $t \approx t_{\text{coh}}$ when

$$\xi(t_{\text{coh}}) \approx \int_0^{t_{\text{coh}}} c(t')\,dt', \tag{2.4}$$

the regions within the coherence length $\xi(t_{\text{coh}})$ are already connected, while outside they are causally disconnected. So the phase of the order parameter is well defined within the coherence length, but the phases in regions outside ξ do not match each other. This corresponds to well-defined vortices with the separation $\tilde{\xi}_{\text{initial}} = \xi(t_{\text{coh}})$. The time t_{coh} after the transition when this happens is

$$t_{\text{coh}} \approx \sqrt{\tau_0 \tau_Q}, \quad \tau_0 \approx \frac{\xi_0}{v_F} \approx \frac{\hbar}{\Delta_0} \sim 10^{-9}\ \text{s}, \tag{2.5}$$

and thus the initial separation between the vortices in the infinite cluster is

$$\tilde{\xi}_{\text{initial}} = \xi(t_{\text{coh}}) \approx \xi_0 \left(\frac{\tau_Q}{\tau_0} \right)^{1/4}. \tag{2.6}$$

For the more general case, when the phase transition is not necessarily described by the Ginzburg–Landau theory, one has $\tilde{\xi}_{\text{initial}} \sim \xi_0 (\tau_Q / \tau_0)^{\alpha}$.

The further development of the infinite cluster, which leads to its final elimination, has been the subject of intensive investigations in phase ordering kinetics (see, e.g., the review in Ref. 12).

In the neutron experiments in ^{3}He-B one has the estimate $\tau_Q \sim R_b^2/D$, where R_b is the size of the bubble and D is the diffusion constant near T_c. This gives $\tau_Q \sim 10\ \mu$s and $\tilde{\xi}_{\text{initial}} \sim 10^{-4}$ cm. In the typical A-phase experiments the cooling of the A-phase through the transition from the normal liquid N occurs over a time $\tau_Q \sim 10^3 - 10^4$ s (Ref. 11), which gives $\tilde{\xi}_{\text{initial}} \sim 10^{-2}$ cm.

3. THE TWO REGIMES FOR A MOVING FRONT

In the presence of a temperature gradient two parameters characterize the nonequilibrium phase transition. In addition to τ_Q, which determines the time scale of the temperature change, one now has the characteristic length scale of the temperature

$$\frac{1}{\lambda} \approx \frac{|\nabla T|}{T_c} . \tag{3.1}$$

Combining this with τ_Q gives the velocity v_T of the propagating temperature front:

$$v_T \approx \frac{\lambda}{\tau_Q} , \tag{3.2}$$

which is thus the velocity of the propagating second-order transition.

The homogeneous result Eq. (2.6) is obtained when the velocity of the front is large compared to $c(t_{\mathrm{coh}})$, so the causality argument does work. This gives the estimation for the critical value of the velocity

$$v_{Tc} \approx \frac{\xi(t_{\mathrm{coh}})}{t_{\mathrm{coh}}} \approx c_0 \left(\frac{\tau_0}{\tau_Q} \right)^{1/4} . \tag{3.3}$$

If $v_T < v_{Tc}$, the slowly moving front dictates the phase of the order parameter, and the formation of vortices should be significantly suppressed compared to the case of a rapidly moving front. In ^{3}He-B neutron experiments one has $\lambda \sim R_b \sim 10$ μm (where R_b is the maximum radius of the bubble of normal fluid above T_c) and $v_T \sim 10^3$ cm/s. This is comparable with $c_0(\tau_0/\tau_Q)^{1/4} \sim 10^3$ cm/s, so vortex nucleation is not suppressed by the moving interface in this experiment.

In the A-phase experiments the typical $\lambda \sim 10^2$ cm and $v_T \approx \lambda \tau_Q \sim 10^{-2} - 10^{-1}$ cm/s, which is much less than $c(t_{\mathrm{coh}}) \sim 10$ cm/s. Thus at this low v_T Eq. (2.6) does not hold, since the phase correlation across the front occurs faster than that due to the temporal change of T. So the creation of vortices is markedly suppressed. However, even in this regime the formation of defects has been experimentally observed: the formation of planar solitons in ^{3}He-A (Ref. 13).

4. PHASE ORDERING BEHIND A SLOWLY MOVING FRONT

One may expect that in the whole range of v_T the initial density of vortices immediately behind the front is determined by the general scaling law

$$\frac{\tilde{\xi}_{\mathrm{initial}}(v_T, \tau_Q)}{\xi_0} = x^{\alpha} F(x^{\beta} y), \quad x = \frac{\tau_Q}{\tau_0}, \quad y = \frac{v_T}{c_0} , \tag{4.1}$$

where $F(u)$ is some function, which has different asymptotes in the two regimes discussed above. From the previous sections it follows that for ^{3}He one has $\alpha = \beta = 1/4$. The regime of fast propagation of the temperature front corresponds to the asymptote $F(u) \to 1$ when its argument $u \gg 1$. Let us find the asymptote in the regime of slow propagation, i.e., $F(u \ll 1)$.

Since the propagation velocity of the order parameter $c(t)$ slows down very near the transition, in some neighborhood of the front, in a layer of thickness $\Delta z \approx v_T \Delta t$, the situation becomes 'homogeneous.' Here Δt is obtained from

$$v_T \Delta t \approx \int_0^{\Delta t} c(t)\,dt \approx c_0 \frac{(\Delta t)^{3/2}}{\tau_Q^{1/2}}, \tag{4.2}$$

which gives

$$\Delta t \approx \tau_Q \frac{v_T^2}{c_0^2}. \tag{4.3}$$

Outside this layer the condensate phase is already fixed due to the phase correlations with the low temperature regions, which are transferred by order parameter waves propagating along the vertical axis. So the only source of the mismatch of the phase originates within this thin layer, which means that the magnitude of the coherence length $\xi(T)$ within the layer determines the initial distance between the vortices as a function of v_T at slow transition:

$$\tilde{\xi}_{\text{initial}}(v_T) \approx \xi(t \approx \Delta t) \approx \xi_0 \frac{c_0}{v_T}, \quad \frac{v_T}{c_0} < \left(\frac{\tau_0}{\tau_Q}\right)^{1/4}. \tag{4.4}$$

Thus in the limit $u \ll 1$, we find $F(u) \sim 1/u$, so the initial length scale is substantially larger than in the case of a rapidly propagating front, where:

$$\tilde{\xi}_{\text{initial}}(v_T) \approx \xi_0 \left(\frac{\tau_Q}{\tau_0}\right)^{1/4}, \quad \frac{v_T}{c_0} > \left(\frac{\tau_0}{\tau_Q}\right)^{1/4}. \tag{4.5}$$

5. DISCUSSION

Estimation of $\tilde{\xi}_{\text{initial}}$ for a slowly propagating front in the A-phase gives $\tilde{\xi}_{\text{initial}} \sim 0.01-0.1$ cm. This is significantly smaller than the size of the cell, ~ 1 cm, and thus well explains the appearance of solitons during the cooling into the A-phase in Ref. 13.

On the other hand, this is of order of the intervortex distance in the rotating cryostat and thus can influence the vortex texture which appears in the rotating cryostat when the superfluid transition occurs under rotation.[11] In a field of 10 mT two types of vortices are competing in the equilibrium rotating state: singular one-quantum vortices with the core radius $r_{\text{core}} \sim \xi(T)$, and continuous two-quantum vortices (textures) with $r_{\text{core}} \sim \xi_D$ (the dipole length $\xi_D \sim 10^{-3}$ cm). At low rotation velocities, $\Omega < 2$ rad/s (or in general at low vortex density), the array of singular one-quantum vortices has less energy. The experimental evidence is that well below 1 rad/s singular vortices are created after the superfluid transition under rotation, and no dependence on the cooling rate was observed. However, the experiment at higher velocity, $\Omega \approx 1.4$ rad/s, showed such dependence: at slow transition the equilibrium (singular) vortices dominate in the cell—their fraction is $n_s/(n_s + 2n_c) \sim 0.8$—while at fast transition the fraction of continuous vortices $2n_c/(n_s + 2n_c)$ increases sharply from 0.2 to 0.8. The change occurs in a jump-like manner at $\partial_t T \sim 6$ μK/min, which corresponds to $\tau_Q \sim 3 \cdot 10^4$ s. One may expect that this is related to the phase ordering process, which leads to an initial vortex density larger than the equilibrium one. The further relaxation of the initial network towards equilibrium may discriminate between textures and singular vortices, which have significantly different scales.

6. CONCLUSION

In a spatially inhomogeneous phase transition vortex formation depends on the velocity v_T of the propagating front of the second-order phase transition. There is a critical value of the front velocity, $v_{Tc} \approx c_0(\tau/\tau_Q)^{1/4}$, which separates two regimes. For a rapidly propagating front, with $v_T > v_{Tc}$, vortex formation is the same as in a spatially homogeneous phase transition. For a slowly propagating front, with $v_T < v_{Tc}$, vortex formation becomes less favorable with decreasing v_T.

We thank M. Krusius and Ü. Parts for numerous discussions of the ^{3}He experiments. This work was supported through the ROTA cooperation plan of the Finnish Academy and the Russian Academy of Sciences, by the Russian Fund for Fundamental Research, Grant No. 96-02-16072, and was carried out under the EU Human Capital and Mobility Programme (contract numbers CHGE-CT94-0069 and CHRX-CT94-0423).

[1] T. W. B. Kibble, J. Phys. A **9**, 1387 (1976).

[2] W. H. Zurek, Nature **317**, 505 (1985); Acta Phys. Polon. B **24**, 1301 (1993); Phys. Rep. **276**, 177 (1996).

[3] A. Vilenkin and E. P. S. Shellard, *Cosmic Strings and Other Topological Defects*, Cambridge University Press, Cambridge, 1993.

[4] M. B. Hindmarsh and T. W. B. Kibble, Rep. Progr. Phys. **58**, 477 (1995).

[5] D. Vollhardt and P. Wölfle, *The Superflujid Phases of* ^3He, Taylor & Francis, London, 1990.

[6] I. Chuang, R. Durrer, N. Turok, and B. Yurke, Science **251**, 1336 (1991).

[7] P. C. Hendry, N. S. Lawson, R. A. M. Lee *et al.*, Nature **368**, 315 (1994); J. Low Temp. Phys. **93**, 1059 (1993).

[8] G. Volovik, *Exotic Properties of Superfluid* ^3He, World Scientific, Singapore, 1992; M. Salomaa and G. Volovik, Rev. Mod. Phys. **59**, 533 (1987).

[9] V. M. H. Ruutu, V. B. Eltsov, A. J. Gill *et al.*, Nature **382**, 334 (1996).

[10] C. Bäuerle, Yu. M. Bunkov, S. N. Fisher *et al.*, Nature **382**, 332 (1996).

[11] Ü. Parts, V. M. H. Ruutu, J. H. Koivuniemi *et al.*, ''Measurements on quantized vortex lines with singular or continuous core structure in rotating ^{3}He-A,'' Report TKK-F-A736, 1995.

[12] A. J. Bray, Advances in Physics, **43**, 357 (1994).

[13] Ü. Parts, V. M. H. Ruutu, J. H. Koivuniemi *et al.*, Physica B **210**, 311 (1995).

Published in English in the original Russian journal. Edited by Steve Torstveit.

Capacitance spectroscopy investigation of the spin polarization of two-dimensional electronic systems

S. I. Dorozhkin[a] and M. O. Dorokhova
Institute of Solid-State Physics, Russian Academy of Sciences, 142432 Chernogolovka, Russia

R. J. Haug
Max-Planck-Institut für Festkörperforschung, D-70569 Stuttgart 80, Germany

K. Ploog
Paul-Drude Institut für Festkörperelektronik, 10117 Berlin, Germany

(Submitted 10 December 1996)
Pis'ma Zh. Éksp. Teor. Fiz. **65**, No. 1, 102–107 (10 January 1997)

It is shown that capacitance spectroscopy can be used to investigate the spin polarization of two-dimensional electronic systems (2DESs). We employed this method to investigate the spin polarization of 2DESs in a GaAs/AlGaAs heterojunction for filling factors of the magnetic-quantization levels $0.28<\nu<0.9$. It is proved that in the presence of states of the fractional quantum Hall effect with $\nu_f=1/3$ and 2/3 the ground state of a 2DES with $\nu>2/3$ is incompletely spin-polarized.

© *1997 American Institute of Physics.* [S0021-3640(97)01901-4]

PACS numbers: 73.20.Dx, 73.40.Hm, 84.37.+q

It is well known that the interelectronic Columb interaction energy can influence the magnitude of the spin of an electronic system. For two-dimensional electronic systems (2DES), a change of spin polarization compared with the case of noninteracting electrons was demonstrated by numerical calculations for systems with a small number of particles (see the review[1] and the references cited therein) and experiments[2–4] performed in the fractional quantum Hall effect (FQHE) regime. In the calculations, nontrivial spin configurations were discovered for both exact fractional values $\nu_f \equiv p/q$ of the filling factor of the magnetic levels $\nu=n/N_0$ as well as near them. Here p is an integer, q is an odd number, n is the surface electron density in the 2DES, $N_0=eH_n/hc$ is the degeneracy of a single level, and H_n is the component of the magnetic field H perpendicular to the 2DES. The ground state of the 2DES for ν close to ν_f is described as an excited state of the FQHE with charged quasiparticles whose number is proportional to $|\nu-\nu_f|$.[1] The change occurring in the spin polarization of the 2DES in this case as compared with $\nu=\nu_f$ is attributed to the spin of the quasiparticles. A recent prediction[5] of the existence of quasiparticles with high spin (skyrmions) as well as the advent of a theory of composite fermions[6] have additionally stimulated great interest in studying experimentally the spin polarization of 2DESs.[7–9] In most of these experiments[3,4,9,10] the temperature dependences of the magnetoresistance of a 2DES with $\nu=\nu_f$, a fixed value of H_n, and different magnitudes of the magnetic field component H_p parallel to the plane of the 2DES are measured. In so doing, the changes observed in the activation energy of the magnetoresistance,[3,4,9,10] assuming that H_p influences only the Zeeman splitting, give information about the change in the spin of the 2DES as a result of thermal excitation of quasielectron–quasihole pairs.[1] In some cases this permits judging the polarization of the ground state of the system for $\nu=\nu_f$.

This letter proposes a new method for investigating the spin polarization of 2DESs that is applicable for arbitrary values of ν and reports the results of such an investigation for $0.28<\nu<0.9$. The method is implemented in field-effect transistors and consists of measuring the change occurring in the capacitance between the 2DES and the transistor gate upon a change in the parallel component of the magnetic field. As is well known (see, for example, Refs. 11 and 12 and the references cited therein), the measured value of the capacitance C includes a derivative of the chemical potential μ of the 2DES with respect to the carrier density:

$$C\approx C_g\left(1-\frac{C_g}{e^2G}\frac{d\mu}{dn}\right)=C_g\left(1-\frac{C_g}{e^2G}\frac{d^2E}{dn^2}\right). \tag{1}$$

Here E is the total energy of the system (all energies of the 2DES are normalized to unit area), G is the sample area under the gate, $C_g=\kappa G/4\pi d$ is the geometric capacitance of the sample (κ is the permittivity of the material) determined by the effective distance $d=d_0+z_0(n)+n\,dz_0/dn$ between the 2DES and the gate.[12] Here d_0 is the distance between the gate and the GaAs/AlGaAs heterojunction and z_0 is the distance from the heterojunction to the centroid of the squared wave function of the electrons (for an ideally two-dimensional system $z_0=0$). In an ideal two-dimensional system with no spin–orbit interaction a change in H_p directly influences only the magnitude of the Zeeman energy $E_Z=-g\mu_B\,H\,S_z$, where S_z is the projection of the total spin S on the direction of the magnetic field (both quantities are given per unit area of the 2DES). In the ground state of the 2DES $E_Z=-|g\mu_B|HS$. Here the absolute value sign is used to avoid misunderstandings deriving from the negative sign of the electron g-factor in the experimental material ($g\approx-0.44$). If the spin of the system does not depend on H_p, then the expression for the change ΔC occurring in the capacitance when the parallel component of the field is switched on has the form

$$\Delta C(n,H_n)\equiv C(n,H_n,H_p)-C(n,H_n,0)\approx\frac{C^2}{e^2G}|g\mu_B|(H-H_n)\frac{d^2S}{dn^2}. \tag{2}$$

Therefore ΔC characterizes the spin polarization of the system. The absolute value of the polarization in the experimental range of n can be determined by integrating ΔC with respect to n, if the values of S and dS/dn are known at some point of this interval. It is obvious that the assumption that the spin of the 2DES is independent of H_p (i.e., independent of the Zeeman energy) holds for a completely spin-polarized state of the system, since an increase of the Zeeman splitting can only stabilize such a state. In the case of a unpolarized system, evidently, the Coulomb energy is greater than the Zeeman energy and a variation of the latter energy in some range cannot change the zero value of the polarization. In the case of an incompletely polarized state, the magnitude of the spin is determined by the competition between these two energies. It can be insensitive to the magnitude of the Zeeman energy, if the Coulomb energy, viewed as a function of the spin, possesses a narrow minimum in the interval of possible values of the spin

$[0,n/2]$. Calculations[13,14] show that this situation occurs in a number of cases. An especially graphic example is displayed in Fig. 4 of Ref. 14, where the magnitude of the partial spin polarization of the 2DES remains unchanged when the g-factor is varied by a factor of 3. We note that if and only if the spin of the system does not depend on the Zeeman energy, one can expect that the degree of spin polarization $S/S_{\max}=2S/n$ is a universal function of the filling factor ν. Indeed, it is believed (see, for example, Ref. 1) that the Coulomb energy for a given filling factor and degree of polarization varies as $e^2n^{3/2}$. As a result, the spin-dependent part E_S of the total energy for the ground state of a 2DES can be written in the form

$$E_S=e^2n^{3/2}\phi(n/N_0,S/n)-|g\mu_B|HS.$$

Here ϕ is a function of the variables $n/N_0\equiv\nu$ and S/n. The equilibrium value of the spin should be found from the condition $\partial E_S/\partial S=0$. It is easy to see that a universal function $S(\nu)/n$ arises in solving this equation if and only if the influence of the Zeeman energy can be neglected and the magnitude of the spin is found from the equation $\partial\phi/\partial S=0$. Therefore a linear relation between ΔC and $(H-H_n)$ (see Eq. (2)), which holds for large changes in the magnitude of the total magnetic field, and the observation of the universal function $S(\nu)/n$, measured for different ratios between the Coulomb and Zeeman energies, can serve as experimental confirmation of the validity of the assumption being discussed.

We investigated a 2DES arising in a GaAs/AlGaAs heterostructure grown by molecular-beam epitaxy. The sample had the form of a ''Hall rectangle'' with Ohmic contacts to the two-dimensional layer. A 0.4×2.3 mm metal gate, forming a Schottky barrier with the top layer of the heterostructure, was deposited on the surface of the sample. The electron density n in the two-dimensional layer varies linearly with the voltage applied between the 2DES and the gate. For zero gate voltage one has $n=1.4\cdot10^{11}$ cm^{-2}, and the electron mobility equals $1.2\cdot10^6$ cm^2/V$\cdot$s. The variable current flowing through the capacitance formed by the gate and the 2DES when a voltage with frequency 9.2 Hz and amplitude 30 mV is applied between them was measured in the experiment. To record small changes in the capacitance, the main part of the signal, corresponding to the capacitance $C_0=165$ pF, was compensated. As a result, a sensitivity of approximately 0.01 pF was attained. Under the experimental conditions (6 T $\leqslant H\leqslant$ 10 T, $T=0.5$ K) the Zeeman splitting is much greater than the temperature; this makes it possible to assume[14] that the spin effects which we measured are the same as the spin effects that would occur at $T=0$.

The quantity $C-C_0$ versus ν is displayed in Fig. 1 for different values of H_n. The minima for fractional filling factors $\nu_f=1/3$ and 2/3 correspond to jumps in the chemical potential of the electronic system in the FQHE.[11] The width of the minima is determined by the nonuniform distribution of the electron density in the sample.[15] The variance of this distribution for our samples was determined in Ref. 11 and equals $\sigma=4\cdot10^9$ cm^{-2}. The main effect of the parallel component H_p is a change in the capacitance for $\nu\gtrsim2/3$. Another effect is a small, virtually parallel, shift of the capacitance curves upwards (in Fig. 1 this shift is compensated). The magnitude of the shift increases with H_p and reaches 0.1 pF for $H=12$ T and $H_n=6$ T. It does not depend on the temperature and was determined for each curve From analogous measurements at $T=4.2$ K, where

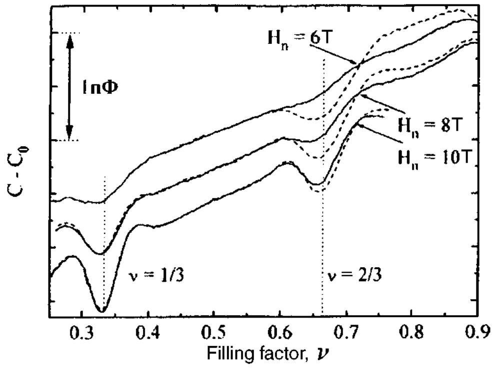

FIG. 1. $C - C_0$ versus the filling factor ν in a perpendicular field (solid curves) and an inclined field of 12 T (dashed curves) for different perpendicular field components H_n (indicated near the curves). $T = 0.5$ K. For clarity, pairs of curves measured with different values of H_n are shifted in the vertical direction relative to one another.

there are no FQHE capacitance minima. The absence of a temperature dependence of the shift shows that the shift is not associated with a change in the Zeeman energy in an inclined magnetic field. Indeed, since the characteristic Zeeman splitting equals ~ 2 K in the range of fields investigated, the polarization of the system should change substantially[14] as the temperature changes from 0.5 to 4.2 K, which would result in a change in d^2S/dn^2. The shift apparently arises because in an inclined magnetic field the electronic wave function is modified in a direction normal to the 2DES, and this changes z_0 and therefore C_g.[12,16]

Therefore we attribute the differences, demonstrated in Fig. 1, between the capacitance curves measured for the same value of H_n to a change in E_Z in an inclined field in accordance with Eq. (2). To determine from these data the magnitude of the spin polarization, we set $S(\nu = 1/3) = n(\nu = 1/3)/2$ in accordance with the generally accepted notion about the total polarization of the ground state of a 2DES with $\nu_f = 1/3$ (see, for example, Ref. 14). Under this assumption our result $\Delta C(\nu = 1/3) = 0$ means that near $\nu = 1/3$ the system remains completely polarized, i.e., $dS/dn(\nu = 1/3) = 1/2$. Having integrated ΔC twice with respect to dn with the boundary conditions $S(\nu = 1/3) = n(\nu = 1/3)/2$ and $dS/dn(\nu = 1/3) = 1/2$, we obtain finally the magnitude of the spin in the entire experimental range of values of ν. It is presented in Fig. 2 in the form of a normalized density of electrons with spins oriented antiparallel to the field $n_\downarrow(\nu)/N_0 \equiv (\nu/2 - S(\nu)/N_0)$. It follows From Fig. 2 that the 2DES remains completely polarized right up to $\nu = 2/3$ (taking account of the variance σ of the density). This result means that there are no skyrmions for $\nu_f = 1/3$ in our parameter range. For $\nu > 2/3$, electrons with spins oriented antiparallel to the field appear in the system, and the polarization decreases. For comparison, the change in the number $n_\downarrow/N_0$ in a 2DES with zero variance of the density is shown in Fig. 2 for the case $n_\downarrow = 0$ for $\nu \leqslant 2/3$, and for $\nu > 2/3$ all electrons entering the system possess a spin oriented antiparallel to the field, i.e., $dn_\downarrow/dn = 1$. Such a dependence is expected near $\nu = 2/3$ in accordance with the predictions[13] of quasihole excitations with spins parallel to the field and quasielectron excitations with spins antiparallel

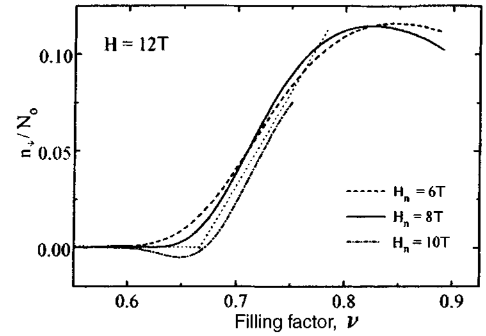

FIG. 2. Normalized density $n_\downarrow/N_0$ of electrons with spin antiparallel to the field as a function of the filling factor ν, determined from data measured with different values of H_n. The region of filling factors $0.28<\nu<0.55$, where $n_\downarrow=0$ to within the limits of the experimental error, is not shown in the plot. The dotted line shows the change in $n_\downarrow/N_0$ corresponding to the addition of electrons with flipped spin to a completely polarized state of FQHE with $\nu_f=2/3$ in the case of zero variance of the electron density in the sample.

to the field for a completely polarized state of FQHE with $\nu_f=2/3$. Therefore our data are an experimental confirmation of the results of numerical calculations[13] performed for systems with a small number of electrons. As ν increases further, the function $n_\downarrow(\nu)/N_0$ passes to a maximum, where it reaches approximately 10%. Although the presence of a maximum agrees qualitatively with the existence of skyrmions with $\nu=1$, the origin of spin depolarization in our experiment is apparently due to the state of FQHE with $\nu=2/3$, since the effect vanishes together with this state.

We now return to the assumption that the spin of the system does not change when a parallel field component H_p is switched on. The results of a check of the linearity of the function $\Delta C(H-H_n)$ are presented in Fig. 3. The normalized quantities $\Delta C/(H-H_n)$ do indeed follow a universal function practically within the limits of the experimental error. The curves of $n_\downarrow/N_0$ versus ν in Fig. 2, which were measured for different values of H_n, are also very close to one another; this means that there exists a universal function

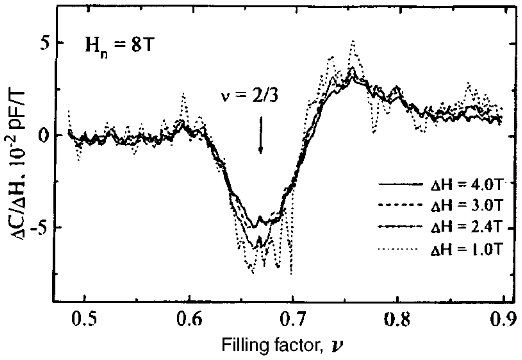

FIG. 3. $\Delta C/\Delta H \equiv \Delta C/(H-H_n)$ versus ν for inclined fields $H=9$, 10.4, 11, and 12 T with $H_n=8$ T.

of ν and that the degree of spin polarization $S/n = 1/2 - \nu^{-1} n_{\downarrow}/N_0$. We note that in real samples, in which a magnetic-field-independent variance σ of the electron density exists, the dependence of S/n on ν can be observed only to within the H_n-dependent variance σ/N_0 of the filling factor. It is obvious that the curves presented in Fig. 2 coincide to within this accuracy. The results of these two checks attest to the correctness of the determination of the spin polarization of the system in this work.

This work was supported by Russian Fund for Fundamental Research Foundation (Grant 95-02-06107). S.I.D. and M. O. D. are also grateful for support from Project INTAS-RFBR 95-0576, and M. O. D. is grateful to the Soros Foundation for a student stipend.

[a] e-mail: dorozh@issp.ac.ru

---

[1] T. Chakraborty and P. Pietiläinen, *The Fractional Quantum Hall Effect*, Springer Series in Solid-State Sciences, edited by K. von Klitzing, Springer-Verlag, Berlin, 1988.

[2] R. J. Haug, K. von Klitzing, R. J. Nicholas *et al.*, Phys. Rev. B **36**, 4528 (1987).

[3] R. G. Clark, S. R. Haynes, A. M. Suckling *et al.*, Phys. Rev. Lett. **62**, 1536 (1989).

[4] J. P. Eisenstein, H. L. Stormer, L. N. Pfeiffer, and K. W. West, Phys. Rev. Lett. **62**, 1540 (1989); J. P. Eisenstein, H. L. Stormer, L. N. Pfeiffer, and K. W. West, Phys. Rev. B **41**, 7910 (1990).

[5] S. L. Sondhi, A. Karlhede, S. A. Kivelson, and E. H. Rezayi, Phys. Rev. B **47**, 16419 (1993).

[6] J. K. Jain, Phys. Rev. Lett. **63**, 199 (1989).

[7] S. E. Barrett, G. Dabbagh, L. N. Pfeiffer *et al.*, Phys. Rev. Lett. **74**, 5112 (1995).

[8] R. R. Du, A. S. Yeh, H. L. Stormer *et al.*, Phys. Rev. Lett. **75**, 3926 (1995).

[9] A. Schmeller, J. P. Eisenstein, L. N. Pfeiffer, and K. W. West, Phys. Rev. Lett. **75**, 4290 (1995).

[10] L. W. Engel, S. W. Hwang, T. Sajoto *et al.*, Phys. Rev. B **45**, 3418 (1992).

[11] S. I. Dorozhkin, R. J. Haug, K. von Klitzing, and K. Ploog, Phys. Rev. B **51**, 14729 (1995).

[12] T. Jungwirth and L. Smrčka, Phys. Rev. B **51**, 10181 (1995).

[13] T. Chakraborty, Surf. Sci. **229**, 16 (1990).

[14] T. Chakraborty and P. Pietiläinen, Phys. Rev. Lett. **76**, 4018 (1996).

[15] F. G. Pikus and A. L. Efros, Phys. Rev. B **47**, 16395 (1993).

[16] J. Hampton, J. P. Eisenstein, L. N. Pfeiffer, and K. W. West, Solid State Commun. **94**, 559 (1995).

Translated by M. E. Alferieff

Weak disorder in a two-dimensional dipole magnet

D. É. Fel'dman
Landau Institute of Theoretical Physics, Russian Academy of Sciences, 142432 Chernogolovka, Moscow Region, Russia

(Submitted 19 November 1996; resubmitted 10 December 1996)
Pis'ma Zh. Éksp. Teor. Fiz. **65**, No. 1, 108–112 (10 January 1997)

The effect of ''random-field'' disorder and ''random-anisotropy-axis'' disorder on a two-dimensional dipole ferromagnet is investigated. It is shown that disorder results in instability of the ferromagnetic phase. The correlation function of the magnetization is calculated with the aid of a self-consistent harmonic approximation. It is found that in the presence of a random field the correlation function is a power-law function of the distance. In the presence of random anisotropy the correlation function decreases logarithmically slowly as a function of distance. © *1997 American Institute of Physics.*
[S0021-3640(97)02001-X]

PACS numbers: 75.10.Nr, 75.70.Ak, 71.45.Gm

Interest in dipole effects in thin magnetic films has intensified in recent years. A remarkable property of dipole forces is their capability of stabilizing long-range order in two-dimensional degenerate magnets.[1,2] It is expected that dipole stabilization of long-range order can be observed in magnetic films with hexagonal symmetry.[3] Recent progress in growing such films[4,5] and observing the domain structure induced by dipole forces[6] is stimulating theoretical investigations of dipole effects in two-dimensional systems.[3,7,8]

This letter studies the effect of weak disorder on the properties of a two-dimensional $X-Y$ dipolar ferromagnet at low temperatures. Since in a Heisenberg dipole magnet the magnetization component normal to the film dies out at large distances,[1,2] our results also pertain to the Heisenberg case. We examine two types of disorder: random field and random anisotropy axis. From symmetry considerations it can be expected that in the presence of other types of disorder with a finite correlation radius the two-dimensional dipole magnet falls into one of these two universality classes. We shall see that disorder destroys long-range order. In the presence of a random field the correlation function of the magnetization depends on the distance according to the same law as in a dirty magnet with no dipole interaction.[9–11] For disorder of the random anisotropy axis type, we shall find a logarithmically slow decay of correlations with distance.

The correlation function will be calculated with the aid of a self-consistent harmonic approximation.[9–14] In contrast to other methods (for example, the renormalization-group method), this procedure takes into consideration the characteristic features of the complicated energy relief of a disordered system and therefore makes it possible to obtain reasonable results.[14] At the same time, the self-consistent harmonic approximation yields accurate quantitative results only for systems in which the order parameter has a large

© 1997 American Institute of Physics

number of components.[14] For this reason, the present work is only a first step in the solution of this problem.

At low temperatures the fluctuations of the modulus of the local magnetization can be neglected and the Hamiltonian of the film can be expressed in terms of the angle $\phi(\mathbf{r})$ which the magnetization makes with some prescribed direction. In the continuous limit the Hamiltonian has the form

$$\begin{aligned} H=\int d^2r\frac{J}{2}(\nabla\phi)^2+\int\int d^2rd^2r'\,\frac{g}{|\mathbf{r}-\mathbf{r}'|^3}[\cos(\phi(\mathbf{r})-\phi(\mathbf{r}'))-3\cos(\phi(\mathbf{r})\\ -\theta(\mathbf{r}-\mathbf{r}'))\cos(\phi(\mathbf{r}')-\theta(\mathbf{r}-\mathbf{r}'))]+\int[h_x(\mathbf{r})\cos(p\phi(\mathbf{r}))\\ +h_y(\mathbf{r})\sin(p\phi(\mathbf{r}))]d^2r. \end{aligned} \tag{1}$$

Here $\theta(\mathbf{r}-\mathbf{r}')$ is the angle between a prescribed direction and an axis connecting the dipole-interacting spins at points $\mathbf{r}$ and $\mathbf{r}'$; the parameter p assumes the value $p=1$ for a random-field type of disorder and $p=2$ for a random-anisotropy-axis type of disorder; and, $h_x(\mathbf{r})$ and $h_y(\mathbf{r})$ are random fields. We assume that these fields are distributed according to a Gaussian distribution and are δ-correlated:

$$\overline{h_\alpha(\mathbf{r})h_\beta(\mathbf{r}')}=\frac{\Delta}{2}\delta_{\alpha\beta}\delta(\mathbf{r}-\mathbf{r}');\quad \alpha,\beta=x,y. \tag{2}$$

The dipole interaction constant g is assumed to be small. In this case the ground state of the pure system is ferromagnetic.

After averaging over the disorder with the aid of the method of replicas, the effective Hamiltonian assumes the form

$$\begin{aligned} H_R=\sum_a\int d^2r\frac{J}{2}(\nabla\phi^a)^2+\int\int d^2rd^2r'\,\frac{g}{|\mathbf{r}-\mathbf{r}'|^3}\sum_a[\cos(\phi^a(\mathbf{r})-\phi^a(\mathbf{r}'))\\ -3\cos(\phi^a(\mathbf{r})-\theta(\mathbf{r}-\mathbf{r}'))\cos(\phi^a(\mathbf{r}')-\theta(\mathbf{r}-\mathbf{r}'))]\\ -\frac{\Delta}{2T}\int\sum_{a,b}\cos[p(\phi^a(\mathbf{r})-\phi^b(\mathbf{r}))]d^2r, \end{aligned} \tag{3}$$

where a and b are the replica indices and T is the temperature.

The self-consistent harmonic approximation, which we employ to calculate the correlation function, consists of finding the extremum of the variation of the free energy

$$F_{VAR}=F_0+\langle H_R-H_0\rangle_0 \tag{4}$$

with respect to the quadratic trial Hamiltonian

$$H_0=\frac{1}{2}\int\frac{d^2q}{(2\pi)^2}\sum_{ab}G_{ab}^{-1}(\mathbf{q})\phi^a(\mathbf{q})\phi^b(-\mathbf{q}). \tag{5}$$

In Eq. (4) the Hamiltonian H_R is determined from Eq. (3); F_0 is the free energy corresponding to the Hamiltonian H_0; and, $\langle\ldots\rangle_0$ denotes averaging over a Gibbs distribution with Hamiltonian H_0. To simplify the formulas, we set the temperature of the system T equal to 1. Large values of J in the Hamiltonian (1) will correspond to the low-temperature limit.

To perform the averaging in Eq. (4), we employ the fact that for a self-consistent solution of the equations for G_{ab}, which we shall find, $\int G_{aa}(\mathbf{q})[d^2q/(2\pi)^2]$ diverges. As a result, we obtain (to within an unimportant constant) the variational free energy per unit volume

$$F_{VAR}=\frac{1}{2}\int\frac{d^2q}{(2\pi)^2}\left[Jq^2\sum_a G_{aa}(\mathbf{q})-\ln\det\hat{G}_{ab}(\mathbf{q})\right]-\frac{\Delta}{2}\sum_{a\neq b}\exp\left(-\frac{p^2}{2}B_{ab}\right)$$
$$-\frac{g}{2}\int\frac{d^2x}{|\mathbf{x}|^3}\sum_a\exp\left[-\frac{1}{2}\langle(\phi_a(\mathbf{x})-\phi_a(0))^2\rangle_0\right],\tag{6}$$

where

$$B_{ab}=\langle\phi_a(\mathbf{x})-\phi_b(\mathbf{x}))^2\rangle_0=\int\frac{d^2q}{(2\pi)^2}[G_{aa}(\mathbf{q})+G_{bb}(\mathbf{q})-G_{ab}(\mathbf{q})-G_{ba}(\mathbf{q})].\tag{7}$$

Varying expression (6) with respect to G_{ab}, we find

$$G^{-1}_{ab}(\mathbf{q})=Jq^2\delta_{ab}-\sigma_{ab}+g\,\delta_{ab}\int\frac{d^2x}{|\mathbf{x}|^3}(1-\exp(i\mathbf{q}\cdot\mathbf{x}))$$
$$\times\exp\left[-\int\frac{d^2q}{(2\pi)^2}(1-\exp(i\mathbf{q}\cdot\mathbf{x}))G_{aa}(\mathbf{q})\right],\tag{8}$$

where

$$\sigma_{ab}|_{a\neq b}=\Delta p^2\exp\left[-\frac{p^2}{2}B_{ab}\right];\quad \sum_b\sigma_{ab}=0.\tag{9}$$

The variational free energy (6) and the equation for the Green's function (8) are the same as in a system with long-range interaction of the form

$$E_{lr}\sim-\int d^2r\,d^2r'\,\frac{\cos(\phi(\mathbf{r})-\phi(\mathbf{r}'))}{|\mathbf{r}-\mathbf{r}'|^3}.$$

The fact that the correlation functions in a system with such long-range interactions and in a system with dipole forces are the same is apparently an artifact of the variational method. However, there is hope that the self-consistent harmonic approximation makes it possible to describe both systems qualitatively correctly.

For a random-field type of disorder ($p=1$) the solution $G_{ab}(\mathbf{q})$ of Eq. (8) remains the same (to within a small correction) as in the problem with no dipole force.[9–11] This can be verified by a direct substitution. Therefore the power-law behavior of the correlation function of the magnetization is preserved:

$$\langle\mathbf{m}(\mathbf{R})\cdot\mathbf{m}(\mathbf{0})\rangle=\langle\cos(\phi^a(\mathbf{R})-\phi^a(\mathbf{0}))\rangle\sim\frac{1}{R^s};\quad s\geqslant 2.\tag{10}$$

We now consider the case of a random-axis type of disorder. We shall have to rewrite the replica matrices with the aid of the Parisi parameterization.[15,16] The matrix $G_{ab}^{-1}(\mathbf{q})$is parameterized by the diagonal element $G_{aa}^{-1}(\mathbf{q})=T(\mathbf{q})-\tilde{\sigma}$ and the function $-\sigma(y),\ 0\leqslant y\leqslant 1$, where

$$T(\mathbf{q})=Jq^2+g\int\frac{d^2x}{|\mathbf{x}|^3}(1-\exp(i\mathbf{q}\cdot\mathbf{x}))\exp\left[-\int\frac{d^2q}{(2\pi)^2}(1-\exp(i\mathbf{q}\cdot\mathbf{x}))G_{aa}(\mathbf{q})\right], \tag{11}$$

and $\sigma(y)$ and $\tilde{\sigma}=\int_0^1\sigma(y)dy$ are a parameterization of the matrix σ_{ab} (9). Using the formulas for inverting the Parisi matrices,[13] we obtain for the correlation function $G_{aa}(\mathbf{q})$:

$$G_{aa}(\mathbf{q})=\frac{1}{T(\mathbf{q})}\left[1+\int_0^1\frac{dy\,\delta(y)}{y^2(\delta(y)+T(\mathbf{q}))}\right], \tag{12}$$

where

$$\delta(y)=\int_0^y dz\,\sigma'(z)z. \tag{13}$$

Introducing the auxiliary variable

$$g[\delta(y)]=\int\frac{d^2q}{(2\pi)^2}\frac{1}{T(\mathbf{q})+\delta(y)} \tag{14}$$

and proceeding similarly to Ref. 9, we obtain

$$\frac{d}{d\delta}\left(\frac{dg[\delta(y)]}{d\delta}\right)^{-1}=-\frac{p^2}{y}. \tag{15}$$

Equations (11), (12), (14), and (15) form a closed system which we must solve for $p=2$.

We seek $T(\mathbf{q})$ [Eq. (11)] in the form

$$T(q)=qf\left(\ln\frac{1}{q}\right), \tag{16}$$

where $f(\ln 1/q)$ is a slowly varying function of q, $f(\ln 1/q)\rightarrow 0$ as $q\rightarrow 0$, and the ultraviolet cutoff is taken to be 1. We are interested in the region of scales $q\ll 1$, where $f(\ln 1/q)\ll 1$. Calculating systematically according to Eqs. (14), (15), and (12), we find for the correlation function $G_{aa}(q)$ for small q

$$G_{aa}(q)\approx\frac{2\pi}{p^2q^2f^2\left(\ln\frac{1}{q}\right)}\left[\int^{\ln\frac{1}{q}}\frac{dz}{f^2(z)}\right]^{-1}. \tag{17}$$

Substituting expression (17) into Eq. (11), we obtain an equation for $f(\ln 1/q)$, whose asymptotic solution for small q has the form

$$f\left(\ln\frac{1}{q}\right)\sim\left(\ln\frac{1}{q}\right)^{-1/(p^2-2)}=\left(\ln\frac{1}{q}\right)^{-1/2}. \tag{18}$$

Hence we find the magnetization correlation function. To within a double-logarithmic factor

$$\langle \mathbf{m}(\mathbf{R})\cdot\mathbf{m}(\mathbf{0})\rangle=\langle\cos(\phi_a(\mathbf{R})-\phi_a(\mathbf{0}))\rangle\sim\frac{1}{\sqrt{\ln R}}. \tag{19}$$

We have arrived at the conclusion that there is no long-range order in a dirty magnetic film. This result agrees with Imry–Ma type arguments.[17] In the case when ferromagnetic order is destroyed in a region of size l, the loss in dipole energy is $\Delta E_d\sim l^{2D-3}$, where $D=2$ is the dimension of the space. On the other hand, the gain in the disorder energy is $\Delta E_i\sim l^{D/2}$. Since in the two-dimensional case $\Delta E_i\sim\Delta E_d$, behavior typical for the lower critical dimension can be expected, i.e., no long-range order.

In writing the Hamiltonian in the continuous form (1), we have neglected the possibility of vortex creation. This approximation is valid if the correlation function decays slowly with distance. Therefore it can be expected that the contribution of vortices to the correlation function of a dipole magnet with a random-axis type of disorder at low temperatures is very small. The question of the role of vortices in a system with a random-field type of disorder requires further investigation.

In closing, we note that the behavior which we found for a dipole magnet with random anisotropy (19) for a system which is not too large can be interpreted as the presence of long-range ferromagnetic order. In the absence of a dipole force the correlation function of the $X-Y$ model with random anisotropy decreases according to a power law in a space of dimension $D<4$ (Refs. 9–11). Therefore we can conclude that the capability of a dipole force to stabilize long-range order, as discovered in Refs. 1 and 2, remains in the dirty case also, but only if the disorder does not destroy symmetry with respect to a change in the sign of the spin.

I thank V. S. Dotsenko, A. B. Kashuba, S. E. Korshunov, V. L. Pokrovskiĭ, and M. V. Feĭgel'man for many helpful discussions. This work was supported by the Russian Fund for Fundamental Research (Grant 96-02-18985).

[1] S. V. Maleev, Zh. Éksp. Teor. Fiz. **70**, 2374 (1976) [Sov. Phys. JETP **43**, 1240 (1976)].

[2] V. L. Pokrovskiĭ and M. V. Feĭgel'man, Zh. Éksp. Teor. Fiz. **72**, 557 (1977) [Sov. Phys. JETP **45**, 291 (1977)].

[3] Ar. Abanov, A. Kashuba, and V. L. Pokrovsky, to be published.

[4] Z. Q. Qiu, J. Pearson, and S. P. Barder, Phys. Rev. Lett. **67**, 1646 (1991).

[5] R. Plandzelter, G. Steierl, and C. Rau, Phys. Rev. Lett. **74**, 3467 (1995).

[6] R. Allenspach and A. Bishof, Phys. Rev. Lett. **69**, 3385 (1992).

[7] A. Kashuba, Phys. Rev. Lett. **73**, 2264 (1994).

[8] A. Kashuba, Ar. Abanov, and V. L. Pokrovsky, Phys. Rev. Lett. **77**, 2554 (1996).

[9] S. E. Korshunov, Phys. Rev. B **48**, 3969 (1993).

[10] T. Giamarchi and P. Le Doussal, Phys. Rev. Lett. **72**, 1530 (1994).

[11] T. Giamarchi and P. Le Doussal, Phys. Rev. B **52**, 1242 (1995).

[12] E. I. Shakhnovich and A. M. Gutin, J. Phys. A **22**, 1647 (1989).

[13] M. Mezard and G. Parisi, J. Phys. A **23**, L1229 (1990).

[14] M. Mezard, Preprint LPTENS 95/10.
[15] M. Mezard, G. Parisi, and M. Virasoro, *Spin Glass Theory and Beyond*, World Scientific, Singapore, 1987.
[16] V. S. Dotsenko, Usp. Fiz. Nauk **163**, 1 (1993).
[17] Y. Imry and S. K. Ma, Phys. Rev. Lett. **35**, 1399 (1975).

Translated by M. E. Alferieff

Transformation of a soliton at a point of zero nonlinearity

T. G. Talipova[a)] and E. N. Pelinovskiĭ
Institute of Applied Physics, Russian Academy of Sciences, 603600 Nizhniĭ Novgorod, Russia

R. Grimshaw
Monash University, Clayton, Victoria 3168, Australia

(Submitted 25 November 1996)
Pis'ma Zh. Éksp. Teor. Fiz. **65**, No. 1, 113–117 (10 January 1997)

The transformation of a soliton in a zone with a sign-changing nonlinearity has been investigated on the basis of the Korteweg–de Vries equation. It is shown that after passage through the critical zone a soliton with opposite polarity is formed in the wave field and, together with the previously known mechanism of secondary-soliton generation as a result of a pedestal formed at the adiabatic stage, there also exists another mechanism which is associated with the transformation of the wave in a zone of variable nonlinearity after the critical point. It is shown that both mechanisms make approximately the same contribution to the secondary-soliton energetics. © *1997 American Institute of Physics.* [S0021-3640(97)02101-4]

PACS numbers: 05.45.+b

Soliton dynamics under the influence of weak disturbances has been well studied: A soliton changes adiabatically and a pedestal appears behind it. An interesting example of the breakdown of adiabaticity of soliton transformation is the transformation of a soliton in a zone where a nonlinearity changes sign. This problem appears, for example, in the theory of internal waves in a stratified ocean, when an inclined pycnocline is located approximately midway between the bottom and the free surface. The sign of the nonlinear coefficient in the Korteweg–de Vries equation depends on the position of the pycnocline: The sign is negative if the pycnocline lies closer to the surface and positive in the opposite case. Soliton transformation on an inclined pycnocline was analyzed quite a long time ago: Even in the analysis of the adiabatic stage, it was shown that the amplitude of the soliton approaches zero as the critical point (where the nonlinearity vanishes) is approached, and it was concluded that the soliton is destroyed at this point.[1–3] The latter fact appeared obvious since the mass of the wave field is conserved: A new soliton, which can exist after the critical point, possesses a different polarity and cannot contribute to this integral. Numerical experiments performed later confirmed the destruction of the initial soliton, but they showed that a soliton with opposite polarity still forms after passage through the critical point.[4,5] This effect was attributed to the appearance of a shelf with opposite polarity behind the soliton, still at the adiabatic stage, that could become a source for the generation of a new soliton (see also Ref. 6). In this case, essentially only ''half'' of the transformation of the wave — only as it moves toward the critical point — is taken into account. However, the nonlinear transformation of the wave can also occur after passage through the critical point, when the modulus of the nonlinearity returns to its initial value. It will be shown below that both stages of the transformation of the wave (before and after the critical point) make an equal contribution to the generation of a secondary soliton. It is important to underscore that this effect is also important for practical applications, since direct proofs of a change in sign of the nonlinearity for internal waves transformed on a shelf have recently been obtained.[7]

Let us consider the following simplified form of the Korteweg–de Vries equation with a variable nonlinear coefficient

$$\frac{\partial u}{\partial t}+\alpha(t)u\frac{\partial u}{\partial x}+\frac{\partial^3 u}{\partial x^3}=0. \tag{1}$$

We shall assume in addition that the nonlinear coefficient changes sign over a characteristic time τ and that its asymptotic values are

$$\alpha(t\rightarrow-\infty)=-1, \quad \alpha(t\rightarrow\infty)=+1. \tag{2}$$

In the case $\alpha=-1$ the soliton is described by the well-known expression

$$u(x,t)=-12\,\mathrm{sech}^2(x-4t), \tag{3}$$

where we have adopted an appropriate normalization of the wave amplitude so that the width of the transitional zone is also normalized to the width of the soliton. We note that Eq. (1) possesses two conservation laws: conservation of mass

$$M=\int_{-\infty}^{\infty}u(x,t)dx=\text{ const}, \tag{4}$$

and conservation of energy

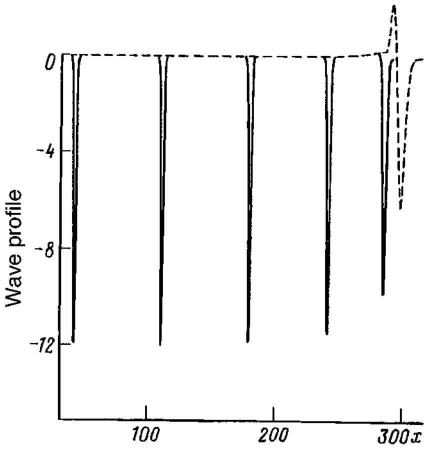

FIG. 1. Soliton transformation in the zone of negative α at different times ($\tau=30$). The interval between the traces is 0.2τ. The dashed line shows the form of the wave at the critical point.

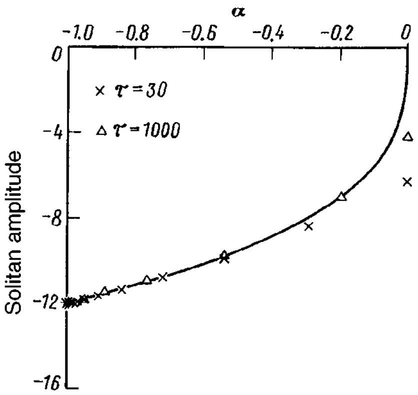

FIG. 2. Variation of the soliton amplitude for different values of τ. The solid line shows the adiabatic dependence (6).

$$E=\int_{-\infty}^{\infty} u^2(x,t)dx = \text{const.} \tag{5}$$

If the transitional zone is sufficiently wide, then at the first stage of decrease of the nonlinear coefficient the soliton retains its form, and its amplitude is determined from the law of conservation of energy (5):

$$a(t)=-12|\alpha(t)|^{1/3}. \tag{6}$$

As one can see from Eq. (6), the amplitude of the soliton approaches zero as the critical point is approached, and therefore a negative-polarity soliton should vanish at this point. At the same time, as a result of the law of conservation of mass, it is easy to show that there forms a mass deficit which results in the appearance of a positive-polarity pedestal behind a ''negative'' soliton. The explicit form of this pedestal can be found in a perturbation theory[8,9]

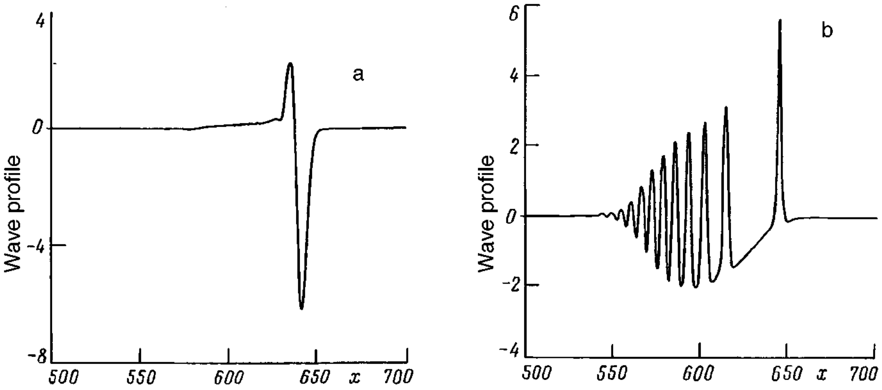

FIG. 3. Transformation of the wave in the zone of positive α, a) $\alpha=0$, b) $\alpha=1$.

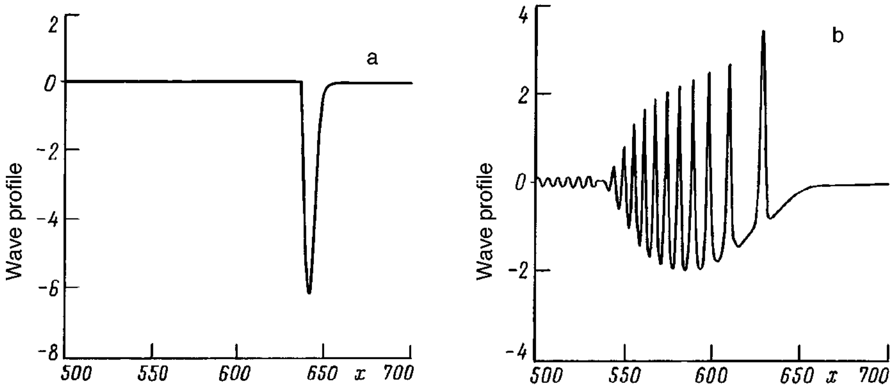

FIG. 4. Transformation of the wave in the zone of positive α as a function of the negative perturbation at the critical point, a) $\alpha=0$, b) $\alpha=1$.

$$u_s=2\frac{d\alpha/dt}{|\alpha|^{8/3}}\ . \tag{7}$$

The height of the pedestal increases without bound as the critical point is approached.

The character of the evolution of the soliton at the adiabatic stage is demonstrated in Figs. 1 and 2, which display the wave profiles at different times and the relation between the amplitude of the wave and the local value of the nonlinear coefficient. These figures were obtained by integrating Eq. (1) numerically for different values of the width τ of the transitional zone. We can see that the adiabatic formula (6) describes the amplitude of the soliton well except in a neighborhood of the critical point.

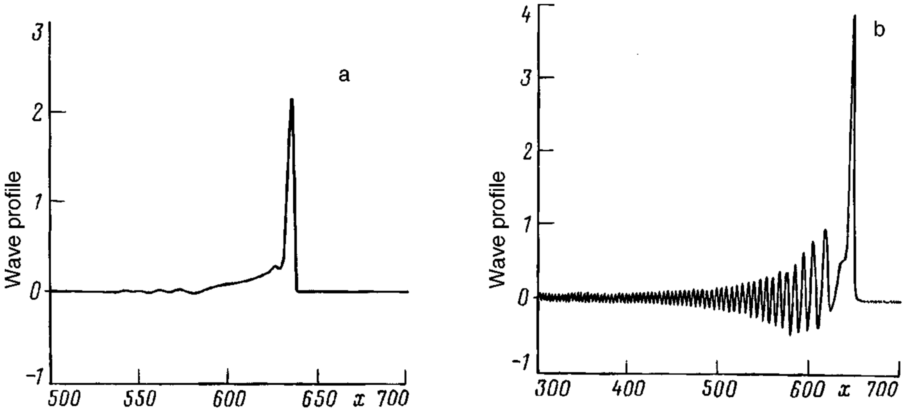

FIG. 5. Transformation of the wave in the zone of positive α as a function of the positive perturbation at the critical point, a) $\alpha=0$, b) $\alpha=1$.

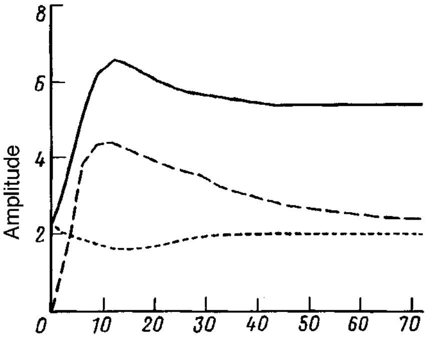

FIG. 6. Variation of the amplitude of the positive pulse in the zone $\alpha > 0$ for different perturbations at the critical point. The solid line shows the actual perturbation; the dashed line, a negative perturbation; and, the dotted line, a positive perturbation.

After passage through the critical point, we have a complicated process of transformation of a nonlinear wave: destruction of the initial negative soliton, formation of an oscillating packet, and generation of secondary solitons of positive polarity; this process is illustrated in Fig. 3 for $\tau = 30$.

In Refs. 4 and 5 the positive part of the wave field (pedestal) was treated as the main source for the generation of secondary solitons. To understand the mechanisms of secondary-soliton generation in numerical experiments, the wave field at the critical point was divided into two parts. In the first experiment only the negative part of the wave field, corresponding to the main wave at the critical point, was used, and the Korteweg–de Vries equation with a corresponding initial condition was solved (Fig. 4). In the second experiment the initial condition is only a pedestal at the critical point (Fig. 5). As one can see, in both cases a secondary soliton with approximately the same amplitude is formed; the temporal evolution of the amplitude of the positive pulse, which transforms into a soliton, is displayed in Fig. 6 for all three variants.

In summary, both the formation of a pedestal behind a soliton at the adiabatic stage and the transformation of the leading (negative) wave in the zone of variable nonlinearity after passage through the critical point have an identical influence on the formation of a secondary soliton generated after passage through the critical point.

This work was performed with the support of the Russian Fund for Fundamental Research (Grants 96-05-64108 and 96-05-64111) and in collaboration between the Institute of Applied Physics of the Russian Academy of Sciences and Monash University (Australia).

[a] e-mail: tata@appl.sci-nnov.ru

---

[1] E. N. Pelinovskiĭ and S. Kh. Shavratskiĭ, Izv. Akad. Nauk SSSR, Fiz. Atmosfery i Okeana **12**, 86 (1976).
[2] V. Djordjevic and L. Redekopp, J. Phys. Oceanogr. **8**, 1016 (1978).
[3] E. N. Pelinovsky and S. Kh. Shavratsky, Physica D **2**, 410 (1981).
[4] C. J. Knickerbocker and A. C. Newell, Phys. Lett. A **75**, 326 (1980).

[5] K. Helfrich, W. Melville, and J. Miles, J. Fluid Mech. **149**, 385 (1984).
[6] B. Malomed and V. Shrira, Physica D **53**, 1 (1991).
[7] P. Holloway, E. Pelinovsky, T. Talipova *et al.*, J. Phys. Oceanogr. (1997) (in press).
[8] Y. Kodama and M. Ablowitz, Stud. Appl. Math. **64**, 225 (1981).
[9] R. Grimshaw and H. Mitsudera, Stud. Appl. Math. **90**, 75 (1993).

Translated by M. E. Alferieff

Resonance luminescence of a nonuniformly heated dense vapor

Yu. K. Zemtsov, A. Yu. Sechin, and A. N. Starostin
Troitsk Institute of Innovational and Thermonuclear Studies, 142092 Troitsk, Moscow District, Russia

A. G. Leonov and D. I. Chekhov
Moscow Physicotechnical Institute, 141700 Dolgoprudnyĭ, Moscow District, Russia

(Submitted 15 November 1996)
Pis'ma Zh. Éksp. Teor. Fiz. **65**, No. 1, 15–19 (10 January 1997)

The thermal luminescence spectra of a dense, nonuniformly heated resonance medium (sodium vapor) are investigated experimentally under conditions when the resonance corrections to the relative permittivity are not small compared to unity and the photon mean free path is comparable to the wavelength of the radiation. The shape of the recorded spectra agrees well with a previously developed general theory of resonance radiation transfer which predicts a strong asymmetry of the spectra. The prospects for performing more-sensitive measurements in order to make a quantitative check of the theoretically predicted anomalous intensity (an order of magnitude higher than in the standard theory of resonance radiation transfer) of the radiation from a dense nonuniform medium are discussed. © *1997 American Institute of Physics.* [S0021-3640(97)00301-0]

PACS numbers: 33.50.Dq, 44.40.+a

In the theory of resonance radiation transfer in gases and plasmas, increasing attention in the last few years has been devoted to the case of a dense medium, for which the resonance correction to the relative permittivity of the medium is not small compared to unity. Under this condition the standard theory[1,2] developed for resonance radiation transfer at low gas densities becomes inapplicable, since the well-known Biberman criterion[1] ($\epsilon' - 1 \ll 1$, where ϵ' is the real part of the relative permittivity $\epsilon = \epsilon' + i\epsilon''$ of the medium) no longer holds, the photon mean free path is comparable to the wavelength of the radiation, and a photon is itself a poor quasiparticle, since the dispersion relation $(\epsilon')^{1/2}\omega = ck$ no longer holds (ω is the photon frequency, c is the speed of light, and k is the wave vector). In Ref. 3 an attempt was made to construct a theory of resonance radiation transfer without the restriction $\epsilon' - 1 \ll 1$ for the case of a dense gaseous medium. In Ref. 3 it was shown that the approach developed there made it possible to predict the existence of fundamentally new effects in resonance radiation transfer processes in dense media. For example, it was shown that the intensity J_ω of the equilibrium radiation in an equilibrium dense strongly absorbing medium can be much higher than the Planckian intensity J_ω^{Pl}:

$$J_\omega=\frac{\hbar\omega^3 n(\omega)}{4\pi^3c^2}\,\frac{\epsilon'}{2}\left(1+\frac{2}{\pi}\,\arctan\,\frac{\epsilon'}{\epsilon''}+\frac{4\epsilon''}{\epsilon'}\ln\left(\frac{\Gamma}{\omega v_T/c}\right)\right)\equiv J_\omega^{\mathrm{Pl}}\psi(\omega)\epsilon', \tag{1}$$

where $n(\omega)$ are the equilibrium photon occupation numbers expressed by Planck's formula $n(\omega)=(\exp(\hbar\omega/kT)^{-1}$ and v_{T} is the thermal velocity of the atoms. Since in media with high densities N the width Γ of a spectral line is determined by resonance collisions in accordance with the Vlasov–Fursov mechanism ($\Gamma\sim N$), the presence of the logarithmic contribution in Eq. (1), which increases with the density, means that within the spectral line contour at detunings $|\omega-\omega_0|\lesssim\Gamma$ (ω_0 is the resonance frequency) the intensity J_ω can be almost an order of magnitude greater than J_ω^{Pl}

Another important effect obtained in Ref. 3 is that the spontaneous emission probability A, given by the expression

$$A\simeq A_0\ \mathrm{Re}(\epsilon^{1/2}), \tag{2}$$

where A_0 is the spontaneous emission probability in vacuum, depends on the properties of the dense medium. Numerical calculations for a sodium resonance doublet show that this formula is accurate and gives values of A which differ from A_0 by approximately a factor of 1.3 on the red wing of the line and by a factor of 0.6 on the blue wing, so that in these two cases the difference of the emission probabilities within the linewidth is more than a factor of two. We note that the Lamb shift in the medium is also determined by the quantity $\mathrm{Re}(\epsilon^{1/2})$. Besides the mechanism considered above, another circumstance which intensifies even more the asymmetry of the absorption and emission lines is the large role of the exponential factor $\exp(-\hbar(\omega-\omega_0)/T)$ in the expressions for the absorption coefficient and the generalized spectral intensity of the volume spontaneous emission in the case of wide lines, which are characteristic for a dense medium (the necessity of allowing for this factor was substantiated in Refs. 3 and 4).

The effects under discussion could be important in observations of thermal radiation from a dense, nonuniformly heated medium. This makes it possible to check experimentally the theory set forth in Ref. 3. In the present work we attempted to observe experimentally the effects predicted in Ref. 3 for the example of dense sodium vapor. We note that for the D_2 lines of sodium at $N\simeq10^{18}$–10^{19} cm^{-3}, one has $|\epsilon'-1|\simeq0.68$ and $\epsilon''\simeq1.36$ (see Ref. 3), irrespective of the vapor density.

The experimental apparatus consisted of a cylindrical cell of the ''heat-pipe'' type, filled with sodium vapor, and a system of highly sensitive detecting devices. Prior to the experiments, the cell (with water-cooled flanges separated by 30 cm and the inner diameter of the pipe equal to 2.8 cm) containing metallic sodium was evacuated to pressure $\sim10^{-5}$ torr, filled with an inert gas (argon) at a pressure of 1 atm, and then heated to a temperature $T_{\mathrm{cen}}\simeq1200$ K (at the center of the cell), at which the sodium vapor density equals $\sim10^{19}$ cm^{-3}. The temperature distribution $T(z)$ along the cell, measured by several thermocouples, is displayed in Fig. 1. We note that the yellow radiation from the Na vapor at the indicated temperature is clearly observed visually through the exit window at the end of the cell. A system of objective lenses collected this radiation from the paraxial zone of the pipe and directed it onto the entrance slit of a diffraction monochromator. The entering light flux was modulated at a frequency ~1000 Hz by a mechanical copper installed in front of the slit. A photomultiplier, whose spectral sensitivity was

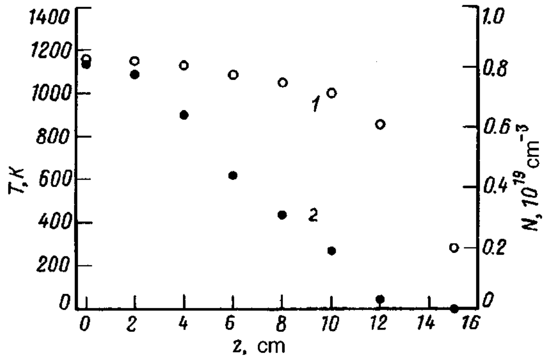

FIG. 1. Temperature (*1*) and density (*2*) distributions along the heat pipe. $z=0$ corresponds to the center of the pipe.

calibrated according to a standard SI-8-200 tungsten lamp, was placed behind the exit slit of the monochromator. The signal from the photomultiplier was amplified with a narrow-band amplifier and then directed into a synchronous detector, the dc voltage from which was fed into a high-precision analog-to-digital converter connected to a computer. The spectral resolution of this system was, as a rule, equal to 0.5 nm.

The characteristic self-inverted spectrum of the thermal radiation of the sodium vapor in the wavelength range 0.5–0.7 μm, as obtained with the apparatus described above, is presented in Fig. 2 for two different scales. The theoretical curve calculated according to the equations from Ref. 3 is also shown in Fig. 2. We note that, according to the calculations, the spectral intensity of the radiation at the center of the layer for the given experimental conditions is much higher than the intensity calculated according to the standard transfer theory (see Fig. 3). In the numerical modeling it was assumed that the distribution of the sodium atoms along the cell is determined by the temperature distribution in accordance with the saturated vapor pressure curve^5 (see Fig. 1). In view of the high density of the vapor and the buffer gas and the high length-to-diameter ratio

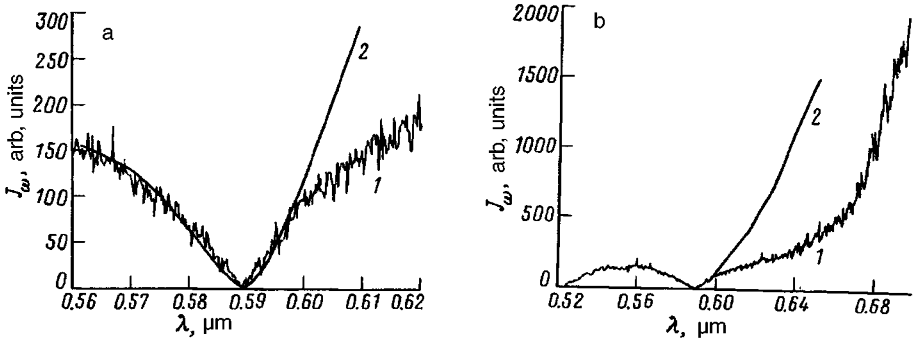

FIG. 2. Experimentally measured (*1*) and theoretically computed (*2*) spectra of the radiation from dense sodium vapor in a heat pipe for two different scales of the spectral intensity of the radiation.

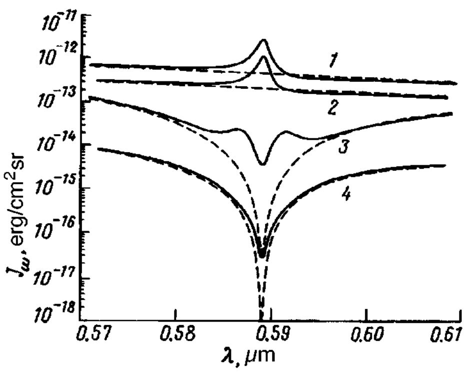

FIG. 3. Radiation spectra of dense sodium vapor computed according to the general transfer theory of Ref. 3 (solid lines) and according to the standard theory (dashed lines): *1,2* — Spectral intensity of the radiation at the center of the layer, *3,4* — spectral intensity at the exit from the layer; *2,4* — for the conditions of the present experiment; *1,3* — for $l = 1$ cm, $T_{\text{cen}} = 1200$ K, $T_0 = 600$ K.

of the cell (~ 10), this approximation is completely correct. Since the experiments measured the relative intensity of the radiation, for comparison with the experimental data the theoretical curve in Fig. 2 was normalized with respect to the intensity of the radiation on the short-wavelength wing of the measured spectrum.

A comparison of the experimental data with the computational results shows that the theoretical curve describes the experimental data well in the region 0.5–0.6 μm. The discrepancy at long wavelengths is apparently due to the effect of the emission and absorption (which was neglected in the calculations) on the electronic–vibrational transitions of molecular sodium Na_2, which is present in quite high quantities (of the order of several percent of the density of atomic sodium) in the volume of the cell.

The most important factor in both the theory and the experiment is the strong asymmetry of the spectrum of the thermal radiation emitted from the resonance medium. This asymmetry cannot be obtained in the standard transfer theory. On account of the inadequate sensitivity of the detecting apparatus, another predicted effect — the fact that the outgoing intensity at line center is much higher than the intensity determined according to the standard theory — is difficult to check quantitatively in the present version of the experiment, since according to the theory of Ref. 3 the radiation flux from the resonance medium remains extremely low at the center of the self-inverted dip. Nonetheless, as the calculations showed, a sizable increase in the intensity of the radiation emanating from a dense resonance medium can be expected upon a decrease (by an order of magnitude or more) in the length of the vapor column and, correspondingly, in the optical thickness τ of the resonance medium; however, this entails substantial technical difficulties. Figure 4 displays the spectral intensity of the radiation from a flat layer of dense, nonuniformly heated sodium vapor as a function of the thickness l of the layer. The curves were calculated according to the theory of Ref. 3 (curve *1*) and according to the standard theory of resonance radiation transfer (curve *2*). It was assumed that the temperature distribution over the thickness of the layer is parabolic, falling from $T_{\text{cen}}(z=0) = 1200$ K at the center of the layer to $T_0(z=l) = 600$ K at the boundary. It

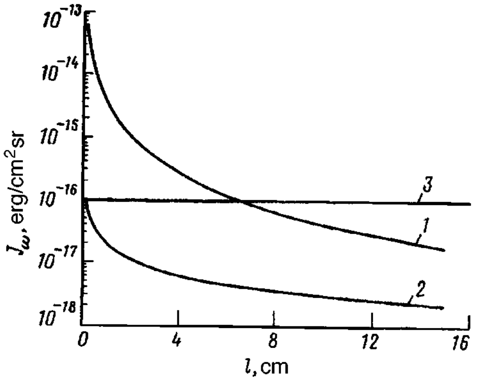

FIG. 4. Spectral intensity of the radiation (under the conditions of exact resonance) emanating from a layer of nonuniformly heated vapor as a function of the thickness l of the layer for a parabolic temperature profile $T(z)$ with $T_{\text{cen}}=1200$ K and $T_0=600$ K: *1* — calculation according to the general transfer theory,[3] *2* — calculation according to the standard theory, *3* — estimated sensitivity of the recording apparatus in the present experiments.

follows from the data presented that as l decreases, the intensity of the radiation at the line center grows rapidly, and the disagreement between the standard theory and the theory of Ref. 3 increases substantially. We note that in our experiments the absolute sensitivity of the detecting apparatus is $\sim 10^{-16}$ ergs/cm^{2}sr (in Fig. 4 the sensitivity is indicated by the line *3*).

Furthermore, as τ decreases, characteristic features in the form of a nonmonotonic dependence of the intensity on the detuning appear in the spectrum at the center of the self-inverted dip. This behavior is a reflection of the spectral properties of the radiation at the center of the vapor (see Fig. 3, where the computed curves of the spectral intensity of the radiation at the center of the layer and the outgoing intensity for $l=1$ cm and a parabolic temperature profile with $T_{\text{cen}}=1200$ K and $T_0=600$ K are displayed). For long lengths of the resonance medium, these features are substantially smoothed out on account of the high absorption (compare the solid curves *3* and *4* in Fig. 3). However, it should be underscored that to observe these effects it is of fundamental importance to have a quite smooth density gradient in order to prevent reflection at the boundary, and for this reason they cannot be observed in cells where a thin uniform layer of a resonance medium with a sharp boundary is produced.

In closing, we note that the appreciable increase of the radiation intensity inside a heated medium as compared to the Planckian intensity can be exploited for resonance pumping of a trace impurity having a resonance transition frequency close to a resonance frequency of the main component of the medium. This can be achieved not only in vapors, but also, for example, in a plasma of multiply charged ions (to increase the pumping efficiency of x-ray lasers with photoresonance excitation).

We thank A. V. Brazhnikov and A. A. Rudenko for assisting in the experiments. This work was supported by the Russian Fund for Fundamental Research (Grant 96-02-17390) and the International Scientific-Technical Center (Project 076/95).

[1] L. M. Biberman, V. S. Vorob'ev, and I. T. Yakubov, *Kinetics of Nonequilibrium Low-Temperature Plasmas*, Plenum Press, New York, 1987 [Russian original: Nauka, Moscow, 1982].
[2] L. A. Apresyan and Yu. A. Kravtsov, *Theory of Radiation Transfer* [in Russian], Nauka, Moscow, 1983.
[3] Yu. K. Zemtsov, A. Yu. Sechin, and A. N. Starostin, Zh. Éksp. Teor. Fiz. **110**, 1654 (1996) [JETP **83**, 909 (1996)].
[4] Yu. K. Zemtsov and A. N. Starostin, Zh. Éksp. Teor. Fiz. **103**, 345 (1993) [JETP **76**, 186 (1993)].
[5] *Physical Quantities* [in Russian], Énergoatomizdat, Moscow, 1986.

Translated by M. E. Alferieff

Interference between spontaneous two-photon radiation from two macroscopic regions

A. V. Burlakov, D. N. Klyshko, S. P. Kulik, A. N. Penin,
and M. V. Chekhova
M. V. Lomonosov Moscow State University, 119899 Moscow, Russia

(Submitted 29 November 1996)
Pis'ma Zh. Éksp. Teor. Fiz. **65**, No. 1, 20–25 (10 January 1997)

Interference is observed between the spontaneous parametric radiation from two nonlinear crystals separated by a macroscopic air gap and excited in series by a common pump beam. The phase of the interference depends on the phase shifts at three frequencies. A simple quantum model agrees well with the experimental results and makes it possible to interpret the effect in terms of general vacuum fluctuations which give rise to the spontaneous emission of mutually coherent radiation from the two crystals. © *1997 American Institute of Physics.* [S0021-3640(97)00401-5]

PACS numbers: 61.80.Ed, 42.25.Hz

Spontaneous parametric scattering (SPS) can be interpreted as being the result of the decay of pump photons with frequency ω_p into a pair of correlated photons (biphotons) with frequencies ω and ω' according to the scheme $\hbar\omega\rightarrow\hbar\omega+\hbar\omega'$ on account of the quadratic nonlinearity χ of a crystal. In the case of a homogeneous crystal and a monochromatic plane pump wave the spontaneous emission of photon pairs occurs predominantly in directions determined by the conditions of stationarity $\omega+\omega'-\omega_p=0$ and spatial homogeneity $\Delta\equiv\mathbf{k}+\mathbf{k}'-\mathbf{k}_p=0$ (here $\mathbf{k}$ are the wave vectors inside the crystal). Together with the dispersion law $\omega(\mathbf{k})$ of the crystal, these equalities, called synchronism conditions, determine the specific form of the frequency–angular spectrum of SPS: A field with a given frequency ω is emitted mainly at a definite scattering angle $\theta=\theta(\omega)$ with respect to $\mathbf{k_p}$. The probability of the emission of a pair of photons in conjugate modes $\mathbf{k}$ and $\mathbf{k}'$ has the form $P(\mathbf{k},\mathbf{k}')=|F(\mathbf{k},\mathbf{k}')|^2$, where the probability amplitude $F(\mathbf{k},\mathbf{k}')$ can be regarded as a two-photon wave packet or as a biphoton state vector in the space $\mathbf{k}\otimes\mathbf{k}'$ (Ref. 1).

It is well known that the standard spontaneous emission of atoms and molecules can be influenced through the use of mirrors, which change the spectral density of the field modes. A characteristic feature of the experiments described below is that the spontaneous emission is controlled not by means of mirrors but rather by means of interference between the fields emitted by two crystals having a common coherent pump and which are separated in space by macroscopic distances (this effect was predicted in Ref. 2 and analyzed in detail in Refs. 3 and 4). In our experiments, the three-wave interaction occurs in two stages in two crystals arranged in series (Fig. 1). Such a configuration is analogous to the well-known method of separated Ramsey fields in beam spectroscopy (see Ref. 3). We also note the analogy to the standard Mach–Zehnder interferometer (Fig. 1a). In the

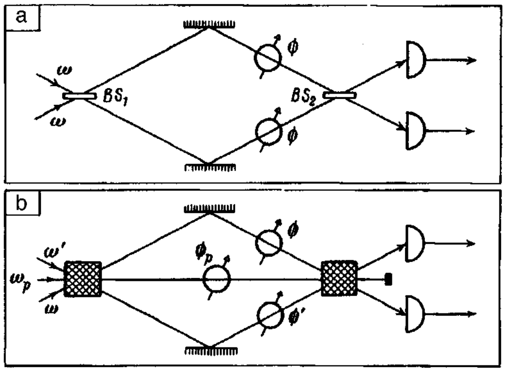

FIG. 1. Mach–Zehnder type scheme for observations of standard (a) and three-frequency (b) interference. In the three-frequency case, the nonlinear crystals play the role of beam splitters (BS) which mix the fields. ϕ, ϕ', ϕ_p—phase shifters at the frequencies ω,ω', and ω_p, respectively.

scheme shown in Fig. 1b the phase of the observed interference depends on three phase delays at three frequencies in the three arms of the interferometer, $\Delta\phi=\phi+\phi'-\phi_p$, so that this effect can be defined as *third-order interference* or *three-frequency interference*. Other possible names are: *two-photon interference of the Ramsey type* or *spontaneous* $SU(1,1)$ *interference*.[5] (We recall that the mixing of two waves by a standard beamsplitter is described by the $SU(2)$ group and the parametric interaction of two waves on account of a fixed pump is described by the $SU(1,1)$ group; see Ref. 5). Actually, in our experiments, the mirrors shown in Fig. 1b were not used, since the scattering angles were quite small (not exceeding several degrees). In this case, the phase shift $\Delta\phi$ was proportional to the length l_1 of the air gap between the crystals. Furthermore, the antiparallel arrangement of the optic axes of the polar crystals employed gave an additional phase shift equal to π.

In the scheme displayed in Fig. 1b the spontaneous emission is suppressed at some frequencies and scattering angles and intensified at others as a result of the presence of the two crystals. This effect at first glance appears to be somewhat paradoxical: It is incomprehensible how the first crystal in the path of the pump beam (left-hand crystal) can suppress or intensify the spontaneous emission from the second crystal. After all, one would think that the spontaneous processes occurring at spatially separated points should be independent of one another, and their intensities and not their amplitudes should add. The paradox is formally resolved by taking account of the fact that the spontaneous emission from both crystals is radiated into a definite pair of output modes $(\mathbf{k},\mathbf{k}')_{\text{out}}$ as a result of quantum fluctuations in the same pair of input modes $(\mathbf{k},\mathbf{k}')_{\text{in}}$. To describe spontaneous effects clearly in the classical theory, it is sufficient to add ''half a photon'' to each input mode of a linear optical system and to subtract it from each output mode.[4] As a result, it can be assumed that the observed spontaneous effects are caused by vacuum fluctuations of the field which are incident on the crystal from all sides. Therefore the fluctuations in the two crystals shown in Fig. 1b comprise a single coherent source. Another interpretation of the quantum formalism is also possible: The interfer-

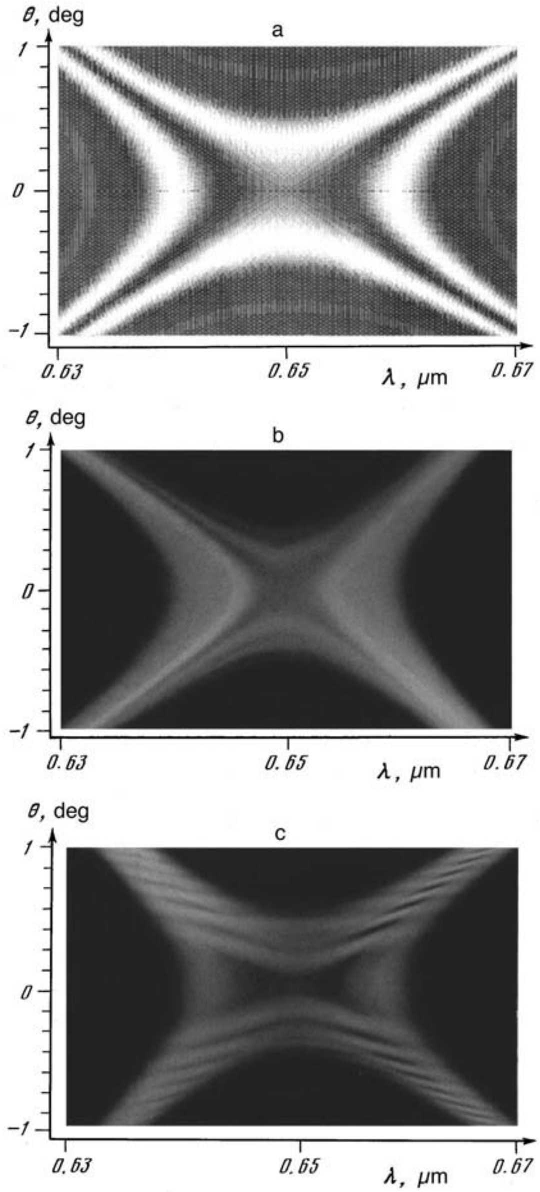

FIG. 2. Three-frequency Mach–Zehnder interference: a) Computed diagram of the frequency–angular distribution of the intensity of the scattered light for $l_1=0$; b, c) photographs of the frequency–angular SPS spectrum near the region of degenerate synchronism with $l_1=0$ (b) and $l_1=10$ mm (c).

ence is due to the fact that there is no information indicating the particular crystal in which the decay of the pump photon occurs.

Let us mention some well-known similar effects. In Ref. 6 interference was observed between two beams with frequency ω which were emitted from two crystals with a common pump (ω_p). An idler wave with frequency $\omega' = \omega_p - \omega$ was directed from one crystal into the second crystal. Additional structure of the frequency–angular SPS spectrum in a multidomain crystal was observed in Ref. 7. In Ref. 8 a single crystal was also used but in this case the interference was caused by mirrors directing all three waves back into the crystal (such effects were analyzed previously in Refs. 9 and 10; they are the basis of the operation of parametric light generators.) In Ref. 11 SPS was observed in a thin nonlinear layer oriented parallel to $\mathbf{k_p}$, and the periodic modulation of the frequency–angular spectrum of the SPS as a result of multiple total internal reflection of idler polariton waves (with frequencies in the far-IR region) was observed.

We shall study SPS in a two-dimensional model in which a mode is given by the frequency ω and the transverse wave vector $q \equiv k_x$ (the z axis is directed parallel to the pump wave vector $\mathbf{k_p}$). In the zero-diffraction approximation the interacting modes are coupled strictly pairwise, $q' = -q$. Let there be two identical nonlinear layers of thickness l separated by a linear transparent material of thickness l_1. The probability that a photon is emitted in the mode (ω, q) has the form (we drop the unimportant constants; see Ref. 3 for a more detailed discussion)

$$P_1(\omega,q) = [\mathrm{sinc}(\delta)\cos(\delta+\delta_1)]^2, \tag{1}$$

where

$$\delta = \Delta_z l/2, \quad \delta_1 = \Delta_{1z} l_1/2,$$

$$\Delta_z = [k^2(\omega) - q^2]^{1/2} + [k^2(\omega') - q^2]^{1/2} - k_p,$$

$$\Delta_{1z} = [k_1^2(\omega) - q^2]^{1/2} + [k_1^2(\omega') - q^2]^{1/2} - k_{1p}.$$

Here the index 1 refers to the intermediate layer. The function $\mathrm{sinc}(\delta)$ in Eq. (1) describes the standard SPS on a single layer of thickness l and the function $\cos(\delta+\delta_1)$ describes the additional frequency–angular structure produced by the interference between the spontaneously emission from the two layers; see Fig. 2. For $l_1 = 0$ the expression (1) becomes $P_1 = \mathrm{sinc}^2(2\delta)$, i.e., it describes scattering by a layer of twice the thickness $2l$. When two crystals with oppositely oriented polar axes are used, the function cos in Eq. (1) is replaced by sin.

Suppose that collinear synchronization, $q_0 = 0$, occurs for the degenerate frequency $\omega_p/2 \equiv \omega_0$. Then the frequency–angular spectrum of the scattered field in the region next to the point (ω_0, q_0) has the characteristic cross shape (see Fig. 2). Let us now transform to the exterior scattering angles θ, which we assume to be small: $q = \omega \sin\theta \approx \omega\theta$ (we set $c = 1$). To within quadratic terms in $\Omega \equiv \omega - \omega_0$ and θ, we find

$$k_z(\Omega,\theta) = k_{0z} + \Omega/u_0 + A\Omega^2 - B\theta^2,$$

$$k_z'(\Omega,\theta) = k_z(-\Omega,\theta), \quad \Delta_z(\omega,\theta) = A\Omega^2 - B\theta^2, \tag{2}$$

$$A \equiv [d^2k/d\omega^2]_0 = 2[dn/d\omega]_0 + \omega_0[d^2n/d\omega^2]_0, \quad B \equiv \omega_0/n_0$$

($u_0 \equiv [d\omega/dk]_0$ is the group velocity and $n(\omega)$ is the refractive index). The slope of the tuning characteristic and the frequency and angular widths of the lines (in the case of a single crystal) are given by

$$d\theta/d\omega = (A/B)^{1/2}, \quad \Delta\omega = C(2/Al)^{1/2}, \quad \Delta\theta = C(2/Bl)^{1/2}. \tag{3}$$

Here $C \equiv 4\sqrt{\pi}/3 = 2.363$ is the integral of the function $[\mathrm{sinc}(x^2)]^2$ from $-\infty$ to $+\infty$; the total width at half-height and the effective (over the area) width of this function are virtually identical. For our experiments

$$\lambda_0 = 2\pi/\omega_0 = 0.65\ \mu\mathrm{m}, \quad n_0 = 1.88, \quad A/2\pi = 0.151\ \mu\mathrm{m}, \quad 2\pi B = 0.818\ \mu\mathrm{m}^{-1}$$

$$\Delta\nu \equiv \Delta\omega/2\pi = 0.028\ \mu\mathrm{m}^{-1}, \quad \Delta\theta = 0.69^\circ, \quad d\theta/d\nu = 24.6\ \mathrm{deg}\cdot\mu\mathrm{m}.$$

In the case of a vacuum gap one has $\Delta_{1z} \approx -\omega_0\theta^2$, so that, with allowance for the antiparallel arrangement of the polar axes, Eq. (1) assumes the form

$$P_1(\Omega,\theta) = \{\mathrm{sinc}[(A\Omega^2 - B\theta^2)l/2]\sin[(A\Omega^2 - B\theta^2)l/2 + \omega_0\theta^2 l_1/2]\}^2. \tag{4}$$

Let Ω and θ be related by the synchronism conditions, i.e., $\theta(\Omega) = \pm(d\theta/d\omega)\Omega$. Then, according to Eq. (4), the intensity of the signal exhibits beats: $P_1(\theta) = \sin^2(\omega_0\theta^2 l_1/2)$. The signal vanishes at the points

$$\theta_m = (2\pi m/\omega_0 l_1)^{1/2} = (m\lambda_0/l_1)^{1/2} = 0.46^\circ\sqrt{m}, \quad m = 0,1,2,\ldots \tag{5}$$

(the numerical estimate is given for $l_1 = 1$ cm). According to Eqs. (3) and (5), the ratio of the position θ_1 of the first minimum to the half-width of the line at center equals $2\theta_1/\Delta\theta = (3/2)(l/n_0 l_1)^{1/2} = 1.33$. These predictions agree well with the experimental results.

A helium–cadmium laser with wavelength $\lambda_p = 0.325\ \mu\mathrm{m}$ and two identical lithium iodate crystals, each 1.5 cm long, separated by a an adjustable distance l_1 were employed for observing the interference. The directions of the optic axes of the crystals made an angle $\theta_p = 59.2^\circ$ with the pump wave vector $\mathbf{k_p}$ inside the crystal. The optic axes of the crystals were oriented antiparallel to one another, so that the effective quadratic susceptibilities had different signs, $\chi_1 = -\chi_2$.

The light emitted by the crystals passed through a lens, at the focal point of which was placed the entrance slit of a spectrograph. Such an optical system makes it possible to observe in the output plane of the spectrograph the two-dimensional distribution of the light intensity in coordinates of the wavelength λ versus the scattering angle θ (crossed dispersions[11]). Detection was performed photographically as well as with the aid of a detector scanned in the output plane of the spectrograph.

The photographs obtained and the patterns calculated according to Eq. (4) are displayed in Fig. 2. We note that the spontaneous emission is suppressed in the directions and at the frequencies of exact synchronism for $l_1 = 0$ on account of the antiparallel arrangement of the polar axes. For $l_1 \neq 0$ the frequency–angular spectrum of the signal acquires a complicated interference structure which depends on l_1. In accordance with Eq. (4), the interference period decreases with increasing gap width l_1 between the nonlinear crystals and with increasing scattering angle θ.

The observed dependence of the intensity of the signal with $\lambda = 0.63\ \mu\mathrm{m}$ on l_1 for fixed scattering angle $\theta = 1.2^\circ$ is displayed in Fig. 3. The period Δl_1 of the oscillations equals 1.6 mm, which agrees well with the value calculated from formula (4): $\Delta l_1 = \lambda/\theta^2 = 1.5$ mm. We note that Δl_1 depends sharply on the scattering angle for a given wavelength $\theta(\lambda)$; the scattering angle can be varied over a wide range, by varying the orientation angle θ_p of the optic axis of the crystal with respect to the pump beam.

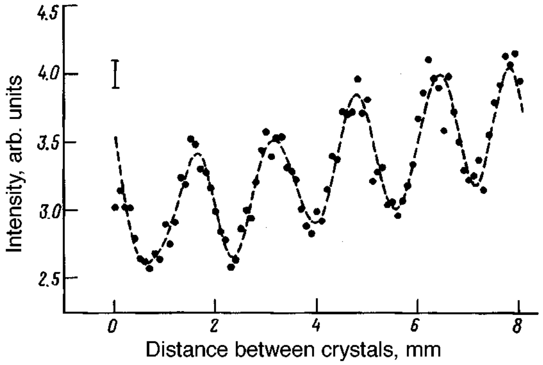

FIG. 3. Radiation intensities at a wavelength of 0.63 μm in the direction of exact synchronism versus the width l_1 of the air gap between the two crystals.

We underscore the fact that the period Δl_1 of the oscillations is determined by a combination of the phase shifts at the three frequencies $\phi+\phi'-\phi_p$ and is of the order of 1 mm. Therefore three-frequency Mach–Zehnder interferometers do not require precise tuning to within a fraction of a wavelength.

The experiments performed demonstrate new possibilities for interferometry and show that the simple phenomenological model employed to describe SPS is adequate. The new type of interference observed here can apparently find practical applications for performing measurements over a wide range of frequencies and a wide rage of optical parameters of materials placed between the crystals.

This work was performed as part of the topic ''Fundamental metrology. Multiphoton interferometry and its applications in precision quantum measurements.''

[1] A. V. Belinsky and D. N. Klyshko, Laser Phys. **4**, 664 (1994).
[2] D. N. Klyshko, Phys. Lett. A **132**, 299 (1988).
[3] D. N. Klyshko, Zh. Éksp. Teor. Fiz. **104**, 2676 (1993) [JETP **77**, 222 (1993)]; Zh. Éksp. Teor. Fiz. **105**, 1574 (1994) [JETP **78**, 848 (1994)].
[4] A. V. Belinsky and D. N. Klyshko, Phys. Lett. A **166**, 303 (1992).
[5] B. Yurke, S. L. McCall, and J. R. Klauder, Phys. Rev. A **33**, 4033 (1986).
[6] Z. Y. Ou, L. J. Wang, X. Y. Zou, and L. Mandel, Phys. Rev. Lett. **41**, 566 (1990).
[7] A. L. Aleksandrovskiĭ, G. Kh. Kitaeva, S. P. Kulik, and A. N. Penin, Zh. Éksp. Teor. Fiz. **90**, 1051 (1986) [Sov. Phys. JETP **63**, 613 (1986)].
[8] T. J. Herzog, J. G. Rarity, H. Weinfurter, and A. Zeilinger, Phys. Rev. Lett. **72**, 629 (1994).
[9] G. Kh. Kitaeva, D. N. Klyshko, and I. V. Taubin, Kvant. Élektron. **9**, 561 (1982) [Sov. J. Quantum Electron. **12**, 333 (1982)].
[10] G. Kh. Kitaeva, A. N. Penin, and A. V. Sergienko, Dokl. Akad. Nauk SSSR **293**, 848 (1987) [Sov. Phys. Dokl. **32**, 293 (1987)].
[11] M. V. Chekhova, S. P. Kulik, and A. N. Penin, Opt. Commun. **114**, 301 (1995).

Translated by M. E. Alferieff

New regions of transparency for intermediate-frequency waves in an inhomogeneous magnetoactive plasma

E. Z. Gusakov, M. A. Irzak, and A. D. Piliya
A. F. Ioffe Physicotechnical Institute, Russian Academy of Sciences, 194021 St. Petersburg, Russia

(Submitted 1 October 1996; resubmitted 15 November 1996)
Pis'ma Zh. Éksp. Teor. Fiz. **65**, No. 1, 26–31 (10 January 1997)

It is shown that in an inhomogeneous plasma there exist new regions of transparency which are absent in the traditional geometrical-optics approach. A more general dispersion relation which adequately describes the propagation of electromagnetic waves in these regions is proposed.
© *1997 American Institute of Physics.* [S0021-3640(97)00501-X]

PACS numbers: 52.35.Bj, 42.25.−p

The geometrical-optics approach is effective in the analysis of wave propagation in an inhomogeneous plasma.[1] In the case when the plasma is inhomogeneous in only one direction, the method is based on an asymptotic expansion of the electric field

$$E_i(x)=\{E_i^{(0)}(x)+E_i^{(1)}(x)+E_i^{(2)}(x)+\dots\}\exp\left[i\frac{\omega}{c}\left(\int^x N_x(x')dx'+N_y y+N_i z\right)\right], \tag{1}$$

where it is assumed that the terms $E_i^{(n)}(x)$ decay as $(k_x L)^{-n}$ (L is the scale size of the inhomogeneity of the plasma). To determine the terms in the series, one must substitute expansion (1) into the wave equation

$$\nabla^2\mathbf{E}-\nabla(\nabla\cdot\mathbf{E})+\frac{\omega^2}{c^2}\hat{\epsilon}\mathbf{E}=0 \tag{2}$$

and equate terms with like powers of the small parameter. In the zeroth approximation $E_i^{(0)}(x)$ can be neglected, and both the dispersion relation

$$D_0(\omega,\mathbf{k},x)=0, \tag{3}$$

which gives the dependence of the wave vector on the frequency and the coordinates, and the polarization of the wave can be determined. These results agree with the corresponding expressions obtained in the theory of a uniform plasma. In the next orders of the approximation, $E_i^{(0)}(x)$ and then $E_i^{(n)}(x)$ are found. The geometrical-optics approach is valid only for a weakly inhomogeneous plasma. Ordinarily, by analogy with the case of a nonmagnetized plasma, it is assumed that the criterion for applicability of the approximation is the condition

$$\frac{1}{k_x^2}\frac{dk_x}{dx}\ll 1, \tag{4}$$

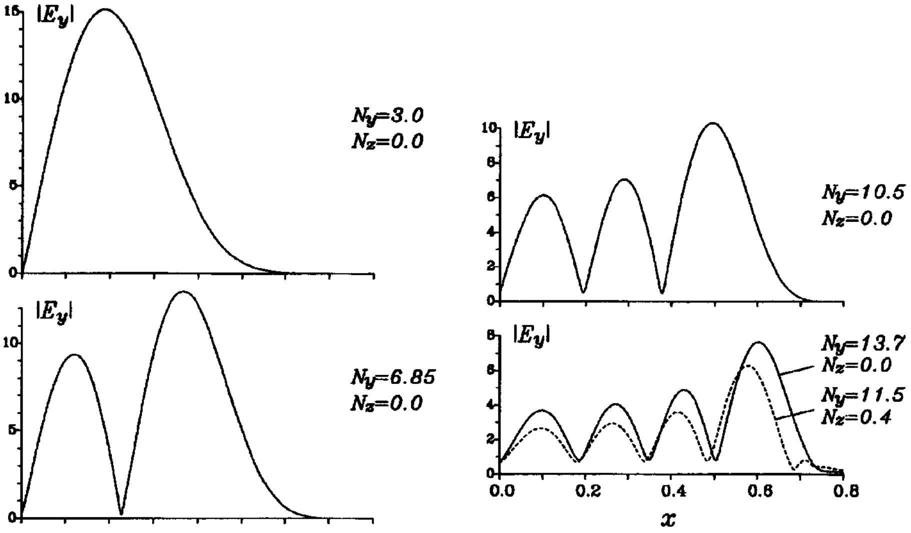

FIG. 1. Structure of the electric fields in a plasma: $f=500$ MHz, $B=18$ kG, $\nabla n=10^{12}$ cm^{-4}. The coordinate x is normalized to c/ω.

though, strictly speaking, the necessary condition for the geometrical-optics to be applicable is

$$|E_i^{(0)}|\gg|E_i^{(1)}|. \tag{5}$$

The importance of this remark can be illustrated for the following example. In the case when the plasma is inhomogeneous in a direction transverse to the external magnetic field ($\mathbf{B}=B_0\mathbf{e}_z$) the dispersion relation (3) has an especially simple form for transversely propagating waves $N_z=0$. For the extraordinary wave in the model of a cold plasma this equation is

$$N_x^2=\frac{\epsilon^2-g^2}{\epsilon}-N_y^2;\quad \epsilon\cong 1+\frac{\omega_{pe}^2}{\omega_{ce}^2}-\frac{\omega_{pi}^2}{\omega^2},\quad g\cong\frac{\omega_{pe}^2}{\omega\omega_{ce}}. \tag{6}$$

It follows from this equation that the lower-hybrid (LH) resonance with transverse propagation is inaccessible from the periphery of the plasma and that waves with $N_y>1$ (i.e., slowed in a direction perpendicular to both the density gradient and the magnetic field) do not propagate. In the latter case, in accordance with Eq. (6), the electric field of a wave decays exponentially in the direction into the plasma according to the law

$$E_y\propto\exp\left(-\frac{\omega}{c}\int^x\sqrt{N_y^2-1+g^2}dx\right), \tag{7}$$

which holds, according to Eq. (4), if $|g'|\ll(\omega/c)N_y^2$ (here and below a prime designates a spatial derivative d/dx).

In some cases, however, this result is strikingly at variance with the results obtained by solving Eq. (2) numerically. As an example, Fig. 1 shows the spatial distribution of the electric field component E_y excited at a frequency of 500 MHz from the periphery of the plasma. At a magnetic field $B = 18$ kG and density gradient $\nabla n_e = 10^{12}$ cm^{-4} the LH resonance lies approximately 7 cm from the surface of the plasma. One can see that for some values $N_y \gg 1$ satisfying the criterion (4) a set of characteristic modes is excited in the plasma. As N_y increases, the field of the wave penetrates deeper and deeper into the plasma and the wavelength decreases. For $N_y > 16$ the propagation region reaches the LH resonance, where strong absorption occurs. This contradiction between the geometrical-optics description (7) and the numerical results is due to the breakdown of the necessary condition for applicability of geometrical optics (5), which in our case has the form $|g'| \ll (\omega/c) N_y$.

The possibility of strong damping of LH waves in the case of transverse propagation was noted in Ref. 2, where the absorption of LH waves in an inhomogeneous cylindrical plasma column was investigated. The accessibility of the LH resonance was confirmed qualitatively in Ref. 2 by an analysis of a differential equation describing the extraordinary wave, and it was concluded that this effect cannot be described in the geometrical-optics approximation and that Eq. (2) must be solved numerically.

We note, however, that the solutions of equation (2), which are presented in Fig. 1 for different values of N_y, possess the ‘‘geometrical-optics form,’’ i.e., they can be represented with the aid of a sinusoidal function with continuously varying wavelength and amplitude. In the case $N_z = 0$ the form of this function can be determined from an equation describing the behavior of the field component E_y:

$$E_y'' + \left[\frac{\epsilon'}{\epsilon} + \frac{\epsilon'}{N_y^2 - \epsilon} \right] E_y' + \frac{\omega^2}{c^2} \left[\frac{\epsilon^2 - g^2}{\epsilon} - N_y^2 - \frac{N_y}{\epsilon} \frac{c}{\omega} g' - \frac{\epsilon'}{\epsilon} \frac{g N_y}{(N_y^2 - \epsilon)} \right] E_y = 0, \tag{8}$$

which is a second-order differential equation. Solving this equation in the WKB approximation, which is a particular case of the geometrical-optics approximation, the field E_y can be expressed in the form (1), with the difference, however, that the refractive index N_x must then satisfy not the condition (6) but a relation which includes terms that are neglected in the classical geometrical-optics analysis:

$$N_x^2 = \frac{\epsilon^2 - g^2}{\epsilon} - N_y^2 - \frac{N_y}{\epsilon} \frac{c}{\omega} \frac{dg}{dx}. \tag{9}$$

The derivation of Eq. (9) employed the condition $|g'| \gg |\epsilon'|$, which holds in the intermediate frequency range. From this relation, whose region of applicability is determined by the criterion (4), it follows that the LH resonance becomes accessible for waves with positive $N_y > 0$ satisfying the following conditions:
$N_y \frac{c}{\omega} \left| \frac{dg}{dx} \right| > N_y^2$ at the plasma boundary and $N_y \frac{c}{\omega} \left| \frac{dg}{dx} \right| > g^2$ near the LH resonance.

According to Eq. (9), the maximum size $\mathcal{L} = c/2\omega$ of the region of wave propagation is reached for $N_y = (c/2\omega_{ce})(\nabla n_e / n_{cr})$. The LH resonance becomes accessible for $L_n = (n_e'/n_{e0})^{-1} < c/\omega$.

The non-geometrical-optics terms can result in fundamentally new effects even for $N_z \neq 0$. The criterion for selecting the important terms can be illustrated for the example of the potential case $E = -\nabla \varphi$, described by the equation $\nabla \cdot \mathbf{D} = 0$. In this case the equation for the electric field potential has the form

$$\epsilon \varphi'' + \epsilon' \varphi' - \left(\frac{\omega}{c} N_y g' - \frac{\omega^2}{c^2} N_y^2 \epsilon - \frac{\omega^2}{c^2} N_z^2 \varphi \right) = 0. \tag{10}$$

Performing a geometrical-optics substitution of the type (1) and neglecting the terms $\epsilon'_{ik} \ll (\omega/c) N_x \epsilon_{ik}$, we obtain the dispersion relation

$$\epsilon (N_x^2 + N_y^2) + \eta N_z^2 + \frac{c}{\omega} N_y g' = 0. \tag{11}$$

Here the term $(c/\omega) N_y g'$ was retained, since in Eq. (10) the terms proportional to $N_y N_x g$ cancelled one another. The condition $(\omega/c) N_x L_n \gg 1$ in this case is not sufficient grounds for neglect. We note that a local dispersion relation of a closely similar form for the potential oscillations of a plasma was obtained in the theory of drift instabilities.[3] In this letter the equations containing the gradient terms are used not for a local analysis of stability but rather for investigating the propagation of stable waves in an inhomogeneous plasma.

We proceed in a similar manner in the general case also. We represent the electric field as a sum of potential and solenoidal parts, $E_i = -\nabla_i \varphi + E_i$. Next, we substitute the geometrical-optics representation of these fields (1) into Eq. (2) and obtain an equation for the potential. We shall retain terms containing spatial derivatives of the components of the permittivity tensor only in the case when the corresponding principal (classical) terms, proportional to the tensor components themselves, vanish. We shall, however, always neglect the derivatives of the amplitude of the electric fields. As a result, we obtain a modified dispersion relation in the form

$$D_0(N, \omega, x) + \delta D = 0, \tag{12}$$

where

$$\delta D = \frac{\epsilon - N^2}{N^2} (\eta - N^2) \left\{ \frac{c}{\omega} \nabla g \left[\mathbf{N} \times \frac{\mathbf{B}}{|\mathbf{B}|} \right] - g \mathbf{N} \frac{c}{\omega} \nabla \times \frac{\mathbf{B}}{|\mathbf{B}|} \right\}; \quad \mathbf{N} = N_x \mathbf{e}_x + N_y \mathbf{e}_y + N_z \mathbf{e}_z .$$

This relation differs from the local dispersion relation for nonpotential plasma oscillations which was obtained in Ref. 3 in an analysis of the low-frequency drift instabilities, by the facts that the curvature of the magnetic field has been taken into account and the imaginary terms giving fictitious exponential growth are absent. It appears that to allow for the latter terms in the dispersion relation is to exceed the first-order accuracy of the geometrical-optics approximation.

The dispersion curves $N_x(x)$ obtained from Eq. (12) with $N_z = 0.4$ and different values of N_y for the parameters of the numerical calculation presented above are displayed in Fig. 2. One can see that for large values of $|N_y|$ a region of transparency appears only for $N_y > 0$. The excitation condition for the characteristic modes which are localized in this region and are the analog of the modes shown in Fig. 1 has the form of a quantization rule:

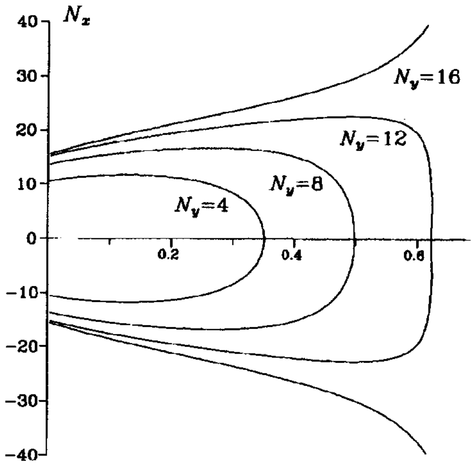

FIG. 2. Dispersion curves for the same plasma parameters. $N_z=0.4$.

$$\frac{\omega}{c}\oint N_x dx=\frac{3\pi}{2}+n\pi, \tag{13}$$

relating the values of the refractive indices N_y and N_z.

A similar relation can be obtained from the results of solving Eq. (2) numerically from the condition that the components of the surface impedance matrix of the plasma vanish. These two predictions are compared in Fig. 3, whence one can see that they are in good agreement.

The inhomogeneity of the plasma can also have a strong effect on the dispersion characteristics of fast magnetosonic waves with frequency equal to several ion-cyclotron frequencies. Figure 4 shows the comparative position of the zeros of the surface impedance of the plasma and the curves corresponding to excitation of the characteristic modes calculated for a wave frequency of 20 MHz, a magnetic field of 500 G, and $\nabla n_e=10^{12}$ cm^{-4} with the aid of the quantization rule (13), into which were substituted the values of N_x calculated both from the classical dispersion relation (3) and from the modified relation (12). A reflecting metallic wall placed 4.8 cm from the surface of the plasma produced the required configuration for excitation of the characteristic modes of the plasma waveguide. One can see that the results obtained with the modified dispersion relation agree very well with the numerical results, while the classical formula is strikingly at variance with them.

The good agreement of the predictions of the modified dispersion relation (12) and the numerical results makes it possible to use this relation for analyzing the ray trajectories of LH waves in a tokamak when modeling current generation in plasma. The radial profiles of the rf current density which were calculated using the dispersion relations (3) (curve *1*) and (12) (curves *2* and *3*) for co- and counterinjection of current in the FT-2 tokamak ($a=8$ cm, $R=55$ cm, $n_e(0)=3\cdot 10^{13}$ cm^{-3}, $T_e(0)=450$ eV, $I_p=30$ kA,

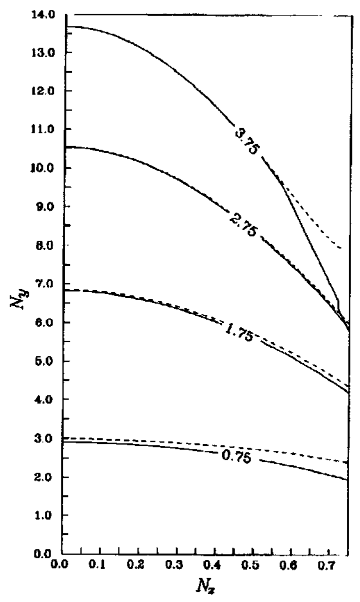

FIG. 3. Position of the zeros of the surface impedance E_y/B_z of the plasma (dashed curves) and values of the phase integrals calculated along the geometrical-optics loops (solid curves).

$B=20$ kG, $P_{\mathrm{rf}}=400$ kW, $2<N_z<4$) are displayed in Fig. 5. The large difference in the

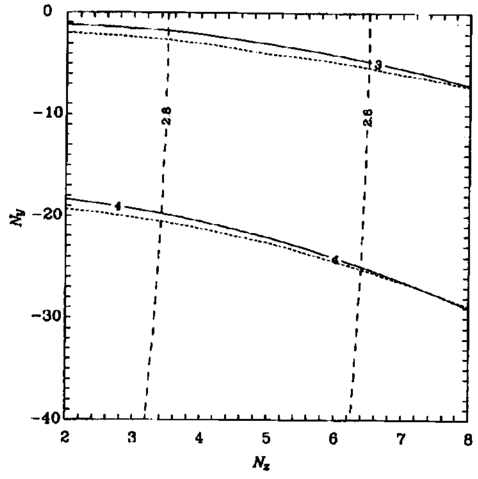

FIG. 4. Position of the zeros of the surface impedance E_y/B_z of the plasma (dotted curves) and values of the phase integrals calculated along the geometrical-optics loops according to the classical (dashed curves) and modified (solid curves) equations: $f=20$ MHz, $B=0.5$ kG (26-th cyclotron harmonic of hydrogen), $\nabla n=10^{12}$ cm^{-4}. The reflecting wall is located 4.8 cm from the plasma boundary.

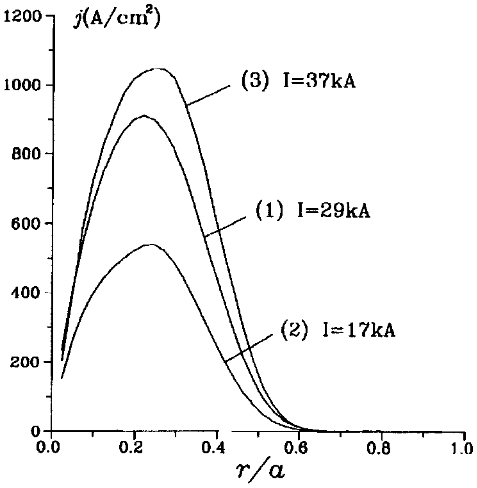

FIG. 5. Radial profiles of the rf current in the FT-2 tokamak. The profiles were calculated on the basis of Eq. (3) (curve *1*) and Eq. (12) (curves *2* and *3*) for co- and counterinjection, respectively.

magnitude and localization of the rf current is due to the different conditions of accessibility for waves with opposite sign of N_y.

In summary, the non-geometrical-optics terms, which are due to the presence of plasma inhomogeneity, can substantially change the dispersion characteristics of intermediate-frequency waves. These terms appreciably influence the form of the ray trajectories and the profiles of the rf entrainment currents in small tokamaks. Furthermore, they may be important in calculations of the conditions of accessibility of some parts of the spectrum of the waves introduced into plasma.

[1] V. L. Ginzburg, *The Propagation of Electromagnetic Waves in Plasma*, Pergamon Press, N. Y., 1970, 2nd edition [Russian original, 2nd edition, Nauka, Moscow, 1967].

[2] Yu. N. Dnestrovskiĭ, D. P. Kostomarov, G. V. Pereverzev *et al.*, Fiz. plazmy **1**, 623 (1975) [Sov. J. Plasma Phys. **1**, 344 (1975)].

[3] A. B. Mikhaĭlovskiĭ, *The Theory of Plasma Instabilities* [in Russian], Atomizdat, Moscow, 1977, Vol. 2, Chaps. 5 and 11.

Translated by M. E. Alferieff

Critical current of a nonuniform Josephson junction at an intergrain boundary with a random distribution of dislocations

E. Z. Meĭlikhov and R. M. Farzetdinova
Kurchatov Institute Russian Science Center, 123182 Moscow, Russia

(Submitted 6 November 1996; resubmitted 27 November 1996)
Pis'ma Zh. Éksp. Teor. Fiz. **65**, No. 1, 32–37 (10 January 1997)

The critical current of a nonuniform intergrain Josephson junction is calculated on the assumption that the superconductivity is suppressed by local stresses produced by randomly distributed boundary dislocations. © *1997 American Institute of Physics.*
[S0021-3640(97)00601-4]

PACS numbers: 74.50.+r, 74.60.Jg, 61.72.Bb

It is well known that the low value of the critical current in high-T_c superconducting ceramics is determined by a set of intergrain weak links at the boundaries between neighboring superconducting granules. The weak links appear as a result of a decrease of the superconducting order parameter near such boundaries. This can happen for many reasons, but on clean boundaries with no impurities and no structural imperfections the decrease of the order parameter is ordinarily attributed to mechanical stresses σ_{ik} (i, $k=x, y, z$) generated by dislocations at grain boundaries.[1–3]

In the theory of dislocations, intergrain boundaries are ordinarily associated with a *periodic* system of edge dislocations (for a tilt boundary) or screw dislocations (for a twist boundary),[4] whose density is higher for larger misorientation angles θ of the neighboring grains. The dislocation density is ordinarily characterized by the distance D between dislocations, which is related to the angle θ by the relation $D=b/[2\sin(\theta/2)]$, where b is the magnitude of Burgers vector and does not differ much from the crystal lattice constant a in the direction of this vector (in the simplest cases b simply equals a).

As the distance between dislocations decreases, the stresses generated by the dislocations compensate one another and the width of the high-stress region near the boundaries decreases.[3] An intergrain link should become progressively weaker and the intergrain critical current should increase. This result contradicts numerous experiments which demonstrate that the intergrain critical current decreases rapidly with increasing misorientation angle θ for all types of boundaries (tilt, twist, and mixed) in high-T_c superconducting films[5,6] and crystals.[7]

We assume that this discrepancy is due not to a deficiency of the model but rather an incorrect assumption about the periodicity of the system of boundary dislocations. Indeed, there are various reasons why such a periodicity can be destroyed. It is sufficient to mention thermal fluctuations, which displace dislocations over a distance of the order of the lattice constant, as well as the fact that in the general case the period D of the dislocation structure and the lattice constant are unavoidably incommensurate with one another. For this reason, it is physically more correct to regard the system of boundary dislocations as being *random*, making the assumption that each dislocation can be randomly displaced relative to its ''regular'' position by a distance of the order of a. Therefore the problem largely reduces to calculating the stresses generated by a system of random dislocations near an intergrain boundary. *Numerical* calculations of this kind[3] demonstrate a qualitative agreement with experiment and confirm the fruitfulness of such a ''random'' model. This letter develops an *analytical* method for solving the stated problem. Since the exact stress dependence of the superconducting order parameter is unknown, a simple approximation is used to calculate the intergrain critical current. According to this approximation the order parameter vanishes in regions where $\sigma_{ik} \geqslant \sigma_c$ and remains unchanged in regions where $\sigma_{ik} < \sigma_c$.

PROBABILITY-THEORETIC MODEL OF A RANDOM STRESS FIELD AT A BOUNDARY.

We proceed below from the well-known expression[4] for the tensor components σ_{xx} of the stresses which are produced by a single edge dislocation located at the origin of the coordinates and characterized by Burgers vector **b** directed along the x axis:

$$\sigma_{xx} = -b\sigma_0 y(3x^2+y^2)/(x^2+y^2)^2, \tag{1}$$

where $\sigma_0 = G/[2\pi(1-\mu)]$, G is the shear modulus, and μ is Poisson's ratio.

Consider a straight line (we call it the x line) parallel to and located at a distance x from the boundary. Along the x line the stress σ_{ik} does not remain constant and can be described with the aid of a distribution function $f_x(\sigma_{ik})$, whose index signifies that the function introduced refers to the x line. At some points of the x line $|\sigma_{ik}| > \sigma_c$ and at other points $|\sigma_{ik}| < \sigma_c$. The probability w_x that an arbitrary point on the x line is ''good'' (i.e., at this point $|\sigma_{ik}| < \sigma_c$) is determined by the relative fraction of ''good'' segments of this line and equals

$$w_x = \int_{-\sigma_c}^{\sigma_c} f_x(\sigma_{ik})\, d\sigma_{ik}, \tag{2}$$

and the probability that some point of the x line is ''bad'' (i.e., at this point $|\sigma_{ik}| > \sigma_c$) is, of course, equal to $(1-w_x)$.

Now consider an x strip — a region bounded by an intergrain boundary and the x line. The probability that a portion of this strip is bad and the corresponding region outside it is good is proportional to the product of two probabilities: the probability that even the internal points of this part of the x strip which are located farthest away from the boundary are still bad and the probability that all points bordering this part of the x band on the ''outside'' are already good. It is obvious that these two probabilities equal w_x and $(1-w_x)$, respectively. Therefore the probability $p(x)$ that the width of the bad layer on the portion of the boundary under consideration equals x is determined by the simple relation

$$p(x) = p_0 w_x(1-w_x), \tag{3}$$

where p_0 is a normalization factor, determined by the condition $\int_0^\infty p(x)dx=1$. Essentially, $p(x)$ is the *probability that the width of the bad strip measured along a randomly chosen normal to the boundary equals* x.

Now we can easily find the average (over a boundary with nonuniform stress 20 σ_{ik}) value of any physical quantity that depends on the width of the bad strip. Specifically, the most probable width of such a strip equals $\langle x\rangle=\int_0^\infty xp(x)dx$.

The critical current of a Josephson junction on a uniform boundary can be written in the form $i_c=i_0\exp(-d/\xi_N)$, where i_0 is the critical current in the volume and d is the thickness of the bad layer (which is not a superconductor but rather, for example, a normal metal) at the boundary, and ξ_N is the electronic correlation length in the normal metal. The extension of this expression to the nonuniform case has the form

$$\langle i_c\rangle=i_0\int_0^\infty \exp(-2x/\xi_N)p(x)dx, \tag{4}$$

where the factor of 2 takes account of the fact that the bad strip is present on both sides of the boundary.

Therefore the problem of determining the critical current of an intergrain boundary treated as a Josephson junction whose properties are nonuniform as a result of boundary dislocations reduces to finding the above-introduced distribution function $p(x)$ for some given distribution of dislocations along the boundary.

The total stress produced at an arbitrary point of the crystal is a sum of random quantities — the stresses from individual dislocations — and is itself a random quantity. In principle, there exists a method for finding the distribution function of a sum of random quantities with a known distribution law: Markov's method.[8] However, in the case at hand this method does not yield a sufficiently simple analytical expression for this function. Therefore, to get an idea of the form of this function, we shall employ the results of a numerical calculation of the stresses for some realization of a random distribution of dislocations (see Ref. 3). The distribution functions $f_x(\sigma_{xx})$ of the stress at a distance $x=5a$ from a boundary with misorientation angle $\theta=10°$ and different values of the parameter Δ, which is a measure of randomness of the arrangement of the dislocations (Δ equals the rms deviation of the dislocations from their ''regular'' positions) are displayed in Fig. 1.[a)] Similar results were also obtained for other values: $\theta\gtrsim 1°$, $x\gtrsim a$, and $\Delta\gtrsim 0.02$. One can see that to good accuracy the ratio $f_x(\sigma_{xx})/\sigma_{xx}$ is a linear function of the stress. This means that the distribution function can be written in the form

$$f_x(\sigma_{xx})\propto|\sigma_{xx}[\sigma_1(x,\Delta,\theta)-\sigma_{xx}]|, \tag{5}$$

where $\sigma_1(x,\Delta,\theta)$ is the only parameter of the distribution that determines all of its properties, specifically, the variance $D(x,\ \Delta,\ \theta)$, which for a parabolic distribution of the type (5) equals $D=(3/10)\sigma_1^2$. Therefore it is sufficient to know the variance in order to give a complete description of the distribution $f_x(\sigma_{xx})$.

The variance can be estimated with the aid of the following arguments. The total stress field is a result of the superposition of random disturbances, associated with displacements of dislocations from their equilibrium positions, on a periodic ''background'' (corresponding to the equilibrium periodic configuration of the dislocations). Such dis-

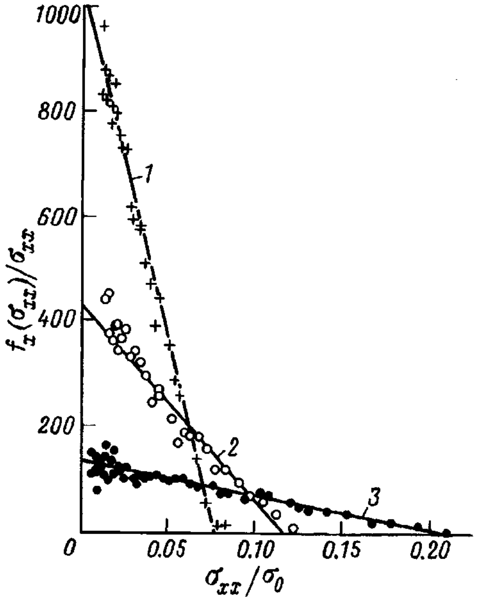

FIG. 1. Results of a numerical calculation (dots)[3] of the distribution function $f_x(\sigma_{xx})$ of the stress at a distance $x=5a$ from an intergrain boundary with misorientation angle $\theta=10°$ for different values of the parameter Δ/a: *1* — 2, *2* — 1, *3* — 0.05. The coordinates were chosen so as to reveal the form of the functional dependence $f_x(\sigma_{xx})$. The straight lines are the corresponding linear approximations.

turbances are produced by dislocation dipoles, which are located on an intergrain boundary and possess a characteristic size $\sim\Delta$ (the distance between dislocations of positive sign). If the variance in the values of Δ is large, then the stresses from the dipoles are compensated only at a large distance from the boundary ($x\gg\Delta$). At such distances one may neglect the weak periodic ''background'' and take into account only the stresses from the system of dipoles. The largest contribution to the stress at this point comes from those dipoles which are located in a boundary segment with a length of the order of x which are located closest to the point of interest. The effective number of such dipoles is $N_{\text{eff}}\sim x/D$. The average random (in magnitude and sign) contribution of each such dipole can easily be estimated with the aid of relation (1): $\delta\sigma_{xx}\approx 3\sigma_0 b\Delta/x^2$. Then the quantity σ_1 determining the variance of the stresses produced by the dipoles equals $\sim\delta\sigma_{xx}\sqrt{N_{\text{eff}}}\sim(b\Delta/x^{3/2}D^{1/2})\sigma_0$. Setting $b=a$ and taking account of the relation between the misorientation angle θ and the period D of the system of edge dislocations ($D=a/[2\sin(\theta/2)]$), we obtain

$$\sigma_1(x,\Delta,\theta)=C\sigma_0\sqrt{\sin(\theta/2)}(a^{1/2}\Delta/x^{3/2}), \tag{6}$$

where $C\sim 1$. A more accurate calculation gives $C\approx 3.5$.

Finally, we can now write down an explicit expression for the distribution function $f_x(\sigma_{xx})$ of the stresses near a boundary and use it, in accordance with the scheme described above, to calculate the critical current of an intergrain Josephson contact. The normalized (on the segment $-\sigma_1<\sigma<\sigma_1$) distribution function has the form $f_x(\sigma)=(3/\sigma_1^3)\sigma(\sigma_1-\sigma)$. This makes it possible to write down the probability $p(x)$, introduced above, as follows:

$$p(x)=3p_0(\sigma_c/\sigma_1)^2(1-(\sigma_c/\sigma_1))^2[1+(4/3)(\sigma_c/\sigma_1)(1-\sigma_c/\sigma_1)], \tag{7}$$

where σ_1 is determined by relation (6).

CRITICAL CURRENT OF A BOUNDARY WITH A RANDOM SYSTEM OF DISLOCATIONS.

The critical current of a nonuniform Josephson junction is determined by relation (4). Substituting into it the function $p(x)$ found above, we obtain the intergrain critical current at a boundary with a random system of edge dislocations:

$$\langle i_c\rangle/i_0=27\left[\tilde{\gamma}(4,\mu)-\frac{2}{3}\tilde{\gamma}(11/2,\mu)-3\tilde{\gamma}(7,\mu)+4\tilde{\gamma}(17/2,\mu)-\frac{4}{3}\tilde{\gamma}(10,\mu)\right], \tag{8}$$

where

$$\tilde{\gamma}(\nu,\mu)=\int_0^1 x^{\nu-1}e^{-\mu x}dx, \quad \mu=\mu_0[\sin(\theta/2)]^{1/3}, \quad \mu_0=4.6(a/\xi_N)[(\Delta/a)/(\sigma_c/\sigma_0)]^{2/3}.$$

For $\theta \geqslant 5°$ and a reasonable choice of the parameter μ_0 (see below) one has $\mu \geqslant 10$. Then the first term $\tilde{\gamma}(4,\mu)\approx 6/\mu^4$ makes the main contribution to the sum in Eq. (8). This makes it possible to write the expression (8) in the following approximate but simple form:

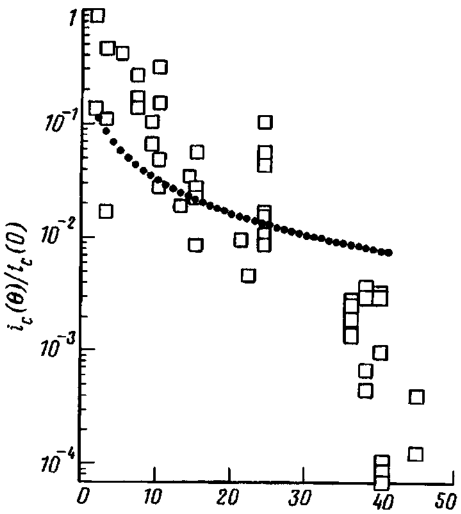

FIG. 2. Comparison of the theoretical angular dependence of the critical current of an intergrain Josephson junction (●) with the experimental data (□) for junctions in $YBa_2Cu_3O_7$ films on bicrystalline substrates.[6]

$$\langle i_c \rangle / i_0 \approx 160/\mu^4 = (160/\mu_0^4)[\sin(\theta/2)]^{-4/3}. \tag{9}$$

The average critical current $\langle i_c \rangle$ of the junction is determined solely (aside from the angle θ, of course) by the parameter μ_0 (see Eq. (8)). Setting $\sigma_c/\sigma_0 = 0.01$, $\xi_N/a = 10$, and $\Delta/a = 2$ (see Ref. 3 for arguments in support of this choice), we obtain $\mu_0 \approx 16$. The quantity $\langle i_c \rangle$ depends quite strongly on the value of μ_0 (see Eq. (9)). This can explain the quite strong variance observed in the data in many experiments. Indeed, the degree of randomness (characterized by the parameter Δ) of a system of dislocations at a boundary can be determined to some extent by the characteristics of its structure, which are associated with the technological process of its formation, the purity of the initial materials, the properties of the substrate (for film structures), and so on.

The degree of agreement between the proposed model and experiment can be judged from Fig. 2, which displays the computed angular dependence of the critical current of an intergrain Josephson junction (for $\mu_0 = 16$) together with the experimental data for Josephson junctions in $YBa_2Cu_3O_7$ films on bicrystalline substrates.[6] One can see that for misorientation angles $\theta \lesssim 25°$ the theoretical curve on average describes the widely ‘‘scattered’’ experimental data fairly well. For angles $\theta \gtrsim 40°$, however, the experimental points drop sharply and, evidently, can no longer be described in the present model. For such angles the interaction of approaching dislocations[b)] now probably becomes so strong that it results in a rearrangement of the dislocation cores (and hence the stress fields produced by the dislocations), on the one hand, and in the appearance of a definite correlation in their arrangement, on the other (which, of course, was neglected above, since the random positions of the dislocations were assumed to be mutually independent).

[a)] The distribution function is even with respect to σ_{xx}; only the part of this function that corresponds to values $\sigma_{xx} > 0$ is shown in Fig. 1.

[b)] For misorientation angle $\theta = 40°$ the distance between the dislocations, calculated formally according to the formula $D = a/[2\sin(\theta/2)]$, equals $1.3a$, which is comparable to the size of the dislocation cores. Of course, the dislocation model is no longer applicable under such conditions.

---

[1] M. F. Chisholm and S. J. Pennycook, Nature **351**, 47 (1991).
[2] S. E. Babcock and J. L. Vargas, Ann. Rev. Mater. Sci. **25**, 193 (1995).
[3] E. Z. Meĭlikhov, Zh. Éksp. Teor. Fiz. **110**, 1453 (1996) [JETP **83**, 803 (1996)].
[4] J. P. Hirth and J. Lothe, *Theory of Dislocations*, McGraw-Hill, New York, 1968.
[5] D. Dimos, P. Chaudhari, J. Mannhart, and F. K. LeGoues, Phys. Rev. Lett. **61**, 1653 (1988).
[6] R. Gross in *Proceedings of the International Conference on Polycrystalline Semiconductors*, Saint Malo, 1993.
[7] M. St. Louis-Weber, V. P. Dravid, V. R. Todt *et al.*, Phys. Rev. B **54**, No. 21 (1996) (in press) .
[8] S. Chandrasekhar, Rev. Mod. Phys. **15**, 1 (1943).

Translated by M. E. Alferieff

Excitonic effects in the recombination radiation spectra of completely filled Landau levels of two-dimensional electrons

O. V. Volkov, V. E. Zhitomirskiĭ, and I. V. Kukushkin
Institute of Solid-State Physics, Russian Academy of Sciences, 142432 Chernogolovka, Moscow District, Russia

K. von Klitzing and K. Eberl
Max-Planck-Institut für Festkörperforschung, 70569 Stuttgart, Germany

(Submitted 13 November 1996)
Pis'ma Zh. Éksp. Teor. Fiz. **65**, No. 1, 38–43 (10 January 1997)

The recombination radiation spectra of two-dimensional electrons in an asymmetrically doped GaAs/AlGaAs quantum well are investigated at different temperatures and laser-excitation energies. At low temperatures and in high magnetic fields the recombination lines of the electrons from completely filled Landau levels are split into narrow sublevels. It is shown that this fine structure of the Landau levels is due to the presence of excitonic effects in the initial and final states of the photoexcited system. It is demonstrated that the recombination process is accompanied by the excitation of intersubband and cyclotron magnetoplasma modes. © *1997 American Institute of Physics.* [S0021-3640(97)00701-9]

PACS numbers: 78.66.Fd, 73.50.Gr, 78.60.Ya, 71.70.Di

1. The progress made in recent years in the technology of preparing single quantum wells now makes it possible to investigate in detail the properties of two-dimensional electrons in the ultraquantum limit with the aid of optical spectroscopy.[1] However, a number of unsolved problems still remain in the interpretation of the luminescence spectra obtained at high filling factors, for which the behavior of the system of two-dimensional electrons itself has been studied in far greater detail. For example, it is generally accepted that excitonic effects are important in asymmetrically doped quantum wells either at low carrier densities[2] or for nonequilibrium electrons from an excited size-quantization subband,[3] since the screening of the Coulomb interaction is weakened in both of these cases.[4] However, data on the magnetooscillations of the recombination intensity of a photoexcited subband[5] attest to the presence of excitonic effects for empty Landau levels of the ground subband also. For completely filled Landau levels the excitonic effects cannot be large because of the uniform distribution of the electron density.[6] Nonetheless, in many publications data are presented on the splitting or distortion of the shape of the lines in the recombination spectra of completely filled Landau levels. This behavior is either not discussed[3] or it is explained by the presence of random charged impurities built into the well.[7] The effect of the interaction of intra- and intersubband magnetoplasmons on the shape of luminescence spectra in the case of resonance crossing of optical transitions is discussed in Ref. 8.

We have investigated the radiative recombination of two-dimensional electrons in an asymmetrically doped quantum well with a high electron density $n_s = 6.8 \cdot 10^{11}$ cm^{-2} and a high electron mobility $\mu = 9.8 \cdot 10^5$ cm^2/V$\cdot$s. It is shown below that the spectrum of the recombination radiation of two-dimensional electrons from a completely filled Landau level at temperatures below 10 K in a magnetic field exceeding 2 T splits into narrow sublevels which are an inherent property of two-dimensional systems, since they are observed for different high-quality structures. The width of these sublevels equals the width of the exciton line on the photoexcited subband and is much less than the Landau-level width associated with fluctuations of the random potential. This behavior is explained by the appearance of excitonic effects in the photoexcited subsystem before and after a recombination event.

2. A high-quality asymmetrically doped single quantum well was grown by molecular-beam epitaxy on a GaAs substrate according to the following scheme: a 3000 Å thick GaAs buffer layer, an undoped GaAs-AlGaAs superlattice (30 Å×100 Å) with total thickness 13000 Å, a 250 Å thick GaAs quantum well, a 200 Å thick AlGaAs spacer, and a 450 Å thick layer of doped AlGaAs:Si (doping level 10^{18} cm^{-3}). Optical excitation of the system was performed with a tunable Ti/Sp laser, and the radiation was detected with the aid of a CCD camera. A Ramanor U-1000 double monochromator with a resolution of 0.03 meV served as the spectral instrument.

3. A diagram of the energies of optical transitions in the photoluminescence excitation spectra (PLE) (a) and in the recombination spectra (b) is presented in Fig. 1. The diagram consists of a collection of spectra measured with a small magnetic-field step at temperature $T = 1.5$ K. The white color corresponds to high intensities of an optical transition, and the black color corresponds to a weak signal. Unfortunately, in a two-color representation it is impossible to show equally well the fine structure of the Landau levels with large and small quantum numbers. For this reason the contrast in the diagram was chosen so as to better reveal the structure of the higher energy levels. The magnetic-field threshold for excitation of the low-energy lines in the PLE is associated with the appearance of empty locations in the corresponding Landau level of the two-dimensional electrons as the magnetic field increases. The transition corresponding to a photoexcited size-quantization subband is present in both the recombination and photoexcitation spectra. One can see from Fig. 1 that the optical transitions corresponding to the recombination of electrons from completely filled Landau levels are split into narrow sublevels with a width comparable to that of the exciton line on the photoexcited subband. In addition, this splitting is all the more pronounced (the broadening is smaller) the closer the Landau level is to the Fermi level of the electronic system.

The temperature dependence of the recombination spectra of the system of two-dimensional electrons for magnetic fields corresponding to filling factors ν close to 3, 4, and 6, respectively, is shown in Fig. 2. As the temperature increases there is a redistribution of intensity between the sublevels corresponding to the same Landau level of the electrons. This is due to a change in the distribution function of the photoexcited holes with increasing temperature on account of the filling of the upper-lying hole states, so that at high temperatures the intensity is determined mainly by the values of the matrix elements for a transition between specific electron and hole states. At temperatures above 30 K the fine structure is obliterated and a single wide line, corresponding to the Landau level of the electronic system, remains in the recombination spectrum.

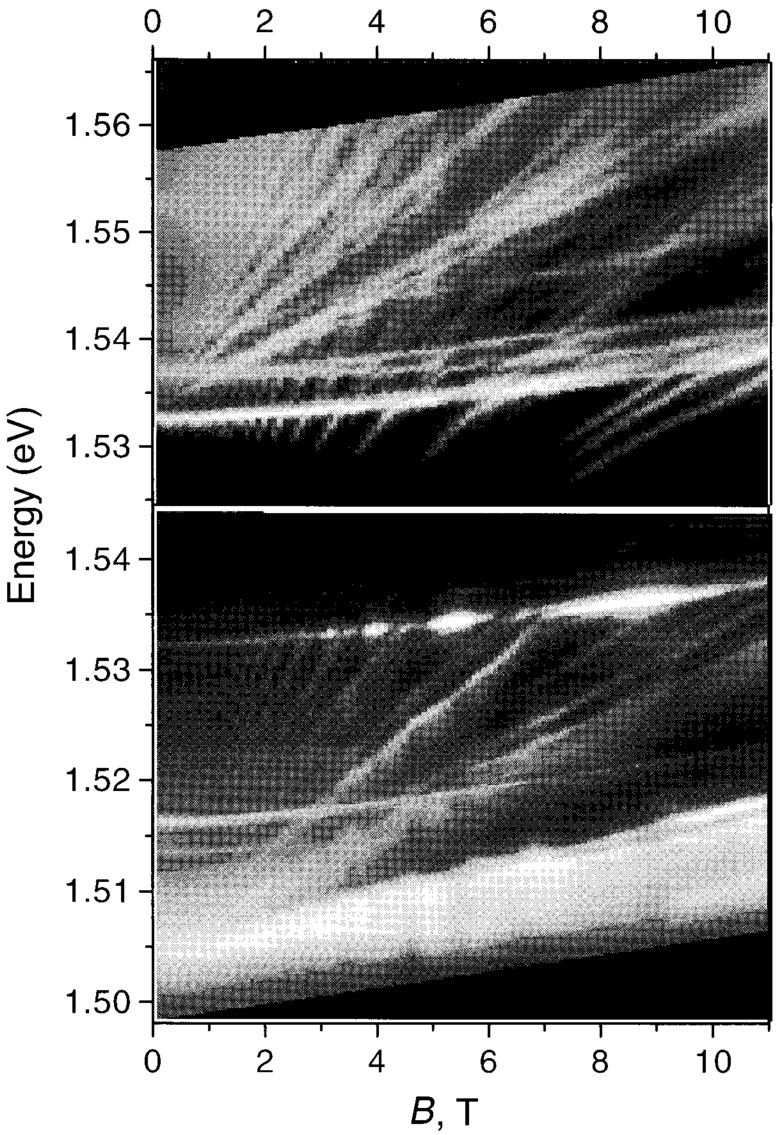

FIG. 1. Diagrams of the energies of optical transitions in PLE (a) and radiative recombination (b) spectra of two-dimensional electrons in a single asymmetrically doped quantum well (thickness 250 Å, carrier density $n_s = 6.6 \cdot 10^{11}$ cm^{-2}) in the magnetic-field range from 0 to 11 T. The diagrams consist of a collection of spectra measured with a small magnetic-field step. The contrast of the diagrams was chosen so that the highest transition intensity would correspond to the white color. Black corresponds to a weak signal.

The luminescence spectra measured in σ^- and σ^+ circular polarizations at a temperature of 1.5 K are presented in Fig. 3. The polarization and the position of the lines agree well with the theoretical results which we obtained for the parameters of the experimental sample. For example, for the zeroth Landau level recombination between

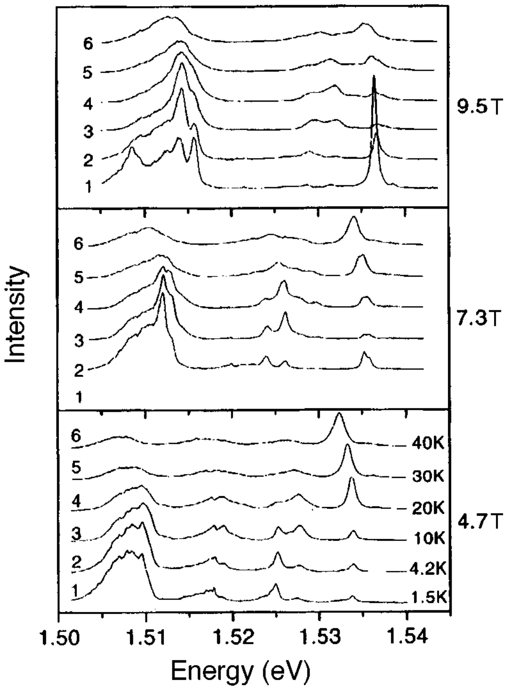

FIG. 2. Temperature dependence of the recombination spectra of two-dimensional electrons. The spectra were measured in magnetic fields corresponding to filling factors $\nu=3$, 4, and 6 of a two-dimensional system. The transition lying highest in energy corresponds to radiation from an excited electronic subband.

the lowest-energy hole $0h+$ and electronic $0+$ states should occur in σ^- polarization and the next (in energy) transition $0h-0$ should occur from the upper spin sublevel of the electrons in σ^+ polarization. For the first Landau level, the lowest-energy transition $0h+1$ will result in recombination in σ^- polarization, while for electrons of the second Landau level the $0h+2+$ transition corresponds to σ^+ circular polarization of the luminescence.

4. The splitting of the recombination line of a completely filled Landau level at temperatures below 10 K in a magnetic field above 2 T into narrow sublevels corresponding to different hole states is due to the appearance of excitonic effects in the photoexcited system before and after a recombination event. Specifically, in the initial state of a photoexcited system an electron in a half-empty Landau level of the ground subband or From a photoexcited size-quantization subband is associated with a hole in the valence band. In the final state the same electron is associated with a ''hole'' formed in the recombination process in a completely filled Landau level. The fluctuations of the random potential of the charged dopants, which determine the broadening of the Landau levels of two-dimensional electrons, do not affect the energy of these excitonic states and the broadening of the lines in the luminescence spectra is mainly due to the finite lifetime of an excitation in a two-dimensional system after the recombination event. This time is determined by the ascension of the ''hole'' to the Fermi level of the system and for this

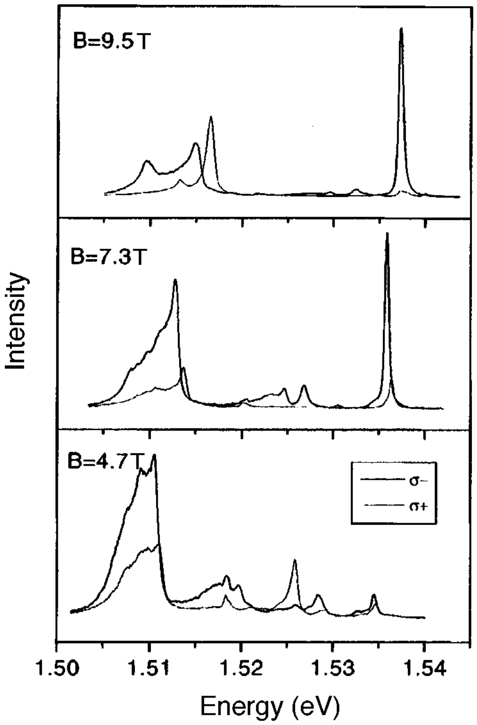

FIG. 3. Recombination spectra of two-dimensional electrons measured in σ^- and σ^+ polarizations at 1.5 K.

reason it is much shorter for the Landau levels lying lower in energy. This fact is demonstrated especially clearly in the magnetic field $B=4.7$ T ($\nu=6$, Fig. 2 and Fig. 3), when the splitting into sublevels is pronounced for the second Landau level but virtually absent for the zeroth level.

5. The recombination spectra of electrons in the zeroth Landau level under resonance laser excitation of different initial states of the system are displayed in Fig. 4. As one can see from the PLE diagram (Fig. 1a), the transitions *5* and *6* in the photoexcitation spectra correspond to the excitonic states $0l-0_1+$ and $0l+0_1-$ with the participation of a light hole and an electron in the zeroth Landau level of the first photoexcited subband. The transition *4* corresponds to a heavy hole and consists of the lines $0h+0_1+$ and $0h-0_1-$. The remaining transitions are associated with an electron on the first Landau level of the ground subband (see Fig. 1). In Fig. 4b one can see the extinction of a line in the recombination spectra of the electrons in the zeroth Landau level under excitation of the system below resonance with a light hole $0l-0_1+$. This line is circularly polarized in σ^+ polarization, just as the transition $0l-0_1+$, and it is shifted downwards From the transitions $0l-0_1+$ by the intersubband magnetoplasmon energy, determined for a given sample from the Raman scattering spectra.[10] Furthermore, the presence of this line in the recombination spectra of the zeroth Landau level correlates with the magnetooscillations in the intensity of the recombination of the photoexcited size-quantization subband.[5] This

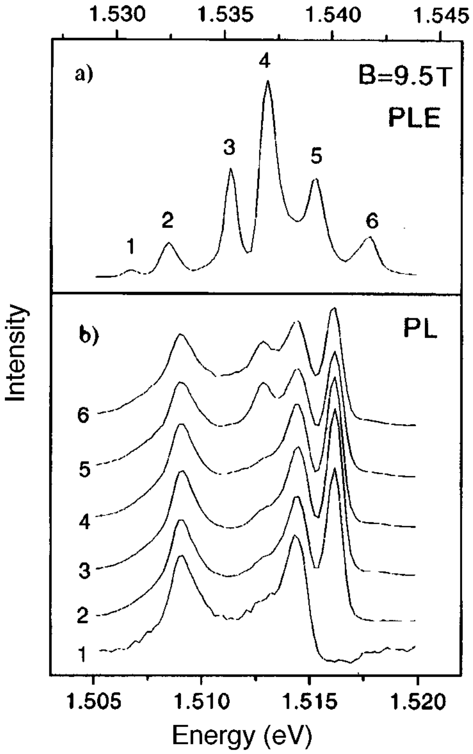

FIG. 4. PLE (a) and radiative recombination (b) spectra of two-dimensional electrons on a completely filled zeroth Landau level. The spectra were measured at $T = 1.5$ K. The different luminescence spectra (*1–6*) correspond to resonance photoexcitation of the transitions *1–6* in part a.

gives grounds for identifying the recombination transition under study as $0l-0+$ with an initial hole state $0l-0_1+$. The energy of this transition, equal to the difference of the energies in the initial and final states of the photoexcited system, is appreciably less than the energy of the transition $0h-0-$ in σ^+ polarization (see Fig. 3), despite the fact that the $0h-$ level lies much lower in energy than the $0l-$ level. This is due to the difference of the excitonic corrections to the energies of the initial, $0l-0_1+$, and final, $0h+0_1+$, magnetoplasmon states.

6. The appearance of a ‘‘hole’’ in a completely filled Landau level after recombination is simply the excitation of a magnetoplasmon mode in the system of two-dimensional electrons. The additional features in the recombination spectra could be due to the complicated dispersion of the intrasubband cyclotron mode.[9] The initial excitonic state $0h+1-$ lying lowest in energy with an electron from the upper spin sublevel of the first Landau level and the subsequent recombination $0h+0+$ of the photoexcited hole with an electron from the lower spin sublevel of the zeroth Landau level results in the excitation of a virtually dispersion-free magnetoplasmon with spin flip $0h+1-$. Starting at a filling factor $\nu=3$ in the two-dimensional electron gas, the photoexcited excitonic state $0h+1-$ can decay into an electron–hole pair $0h+1+$ in the electron spin-relaxation process $1- \Rightarrow 1+$ with the appearance of empty places on the lower spin sublevel. As a result of the orthogonality of the wave functions of the hole $0h+$ and electron in the state $1+$, only the recombination transition $0h+0+$ with excitation of a magnetoplasmon $0h+1+$ in the final state remains allowed. The absence of excitonic effects in the initial state of the system should lead to an ''opening up'' of the dispersion law of the magnetoplasmon in the final state. This will determine the low-energy tail in the recombination spectra of the zeroth Landau level. The presence of features in the density of states of a magnetoplasmon at large quasimomenta, the so-called magnetoroton,[9] could result in the appearance of a new line shifted to a lower energy.

Indeed, a new line dose appear on the low-energy tail in the recombination spectrum of the zeroth Landau level as the temperature decreases below 4 K at filling factors $\nu<3$ (Fig. 2). This line is circularly polarized in σ^- polarization (Fig. 3) and remains in the recombination spectrum with excitation of the lowest hole state $0h+$ (Fig. 4). However, in order to attribute this line unequivocally to the excitation of magnetorotons, additional measurements must be performed in stronger magnetic fields with filling factors $\nu<2$ and different carrier densities in the two-dimensional channel.

7. In summary, we have shown that the shape of the lines in the radiative recombination spectra of a two-dimensional electronic system is determined not only by the density of states of two-dimensional electrons but also by the existence of excitonic effects in the final and initial states of the photoexcited system. We have found that despite the uniform distribution of the electron density on the filled Landau levels, at low temperatures and in a strong magnetic field the recombination lines of the electrons from completely filled Landau levels split into narrow sublevels associated with a set of possible initial and final excitonic states of the photoexcited system. We have demonstrated that the recombination process is accompanied by the excitation of intersubband and cyclotron magnetoplasmon modes.

This work was supported by the Russian Fund for Fundamental Research (Grant 96-02-16177) and INTAS (Grant 95-IN/RU-675).

[1] D. Heiman, B. B. Goldberg, A. Pinczuk *et al.*, Phys. Rev. Lett. **61**, 605 (1988).
[2] A. J. Shields, M. Pepper, D. A. Ritchie, and M. Y. Simmons, Adv. Phys. **44**, 47 (1995); G. Finkelstein, H. Shtrikman, and I. Bar-Joseph, Phys. Rev. Lett. **74**, 976 (1995).
[3] B. Stepniewski, M. Potemski, H. Buhmann *et al.*, Phys. Rev. B **50**, 11895 (1994).
[4] A. B. Henriques, Phys. Rev. B **44**, 3340 (1991).
[5] O. V. Volkov, V. E. Zhitomirskiĭ, I. V. Kukushkin *et al.*, JETP Lett. **64**, 774 (1996).
[6] B. Janovici, Phys. Rev. Lett. **46**, 386 (1981).
[7] P. Vincente, A. Raymond, M. Kamal Saami *et al.*, Solid State Commun. **96**, 901 (1995).
[8] L. V. Butov, L. V. Kulik, V. D. Kulakovskiĭ, and T. G. Andersson, JETP Lett. **56**, 557 (1992).
[9] C. Kallin and B. I. Halperin, Phys. Rev. B **30**, 5655 (1984).
[10] I. V. Kukushkin, K. von Klitzing, and K. Eberl, submitted to Phys. Rev. B (1996).

Translated by M. E. Alferieff

Differential magnetoreflection spectroscopy of doped and undoped II–VI semiconductor quantum wells

A. V. Platonov,[a] V. P. Kochereshko, and D. R. Yakovlev
A. F. Ioffe Physicotechnical Institute, Russian Academy of Sciences, 194021 St. Petersburg, Russia

W. Ossau, A. Waag, and G. Landwehr
Physikalisches Institut der Universität Würzburg, Würzburg, Germany

F. Bassani and R. T. Cox
Laboratoire du Spectrometrie Physique et CENG/CEA, Grenoble, France

(Submitted 19 November 1996)
Pis'ma Zh. Éksp. Teor. Fiz. **65**, No. 1, 44–49 (10 January 1997)

A method has been developed for recording and analyzing the differential magnetoreflection (magnetotransmission) spectra of semiconductor structures with quantum wells. The method was used to determine the exciton g-factor in semimagnetic CdTe/(Cd, Mn)Te heterostructures with quantum wells. In nonmagnetic structures with quantum wells containing a two-dimensional electron gas, the excitonic damping depends on the spin state of the exciton. This effect is explained by the exchange contribution to exciton–electron scattering. © *1997 American Institute of Physics.* [S0021-3640(97)00801-3]

PACS numbers: 78.66.Mf, 78.20.Ls

1. Reflection spectroscopy is successfully employed for studying and characterizing semiconductor heterostructures, quantum wells, superlattices, and quantum wires. This method makes it possible to determine the excitonic parameters (resonance frequency, oscillator strength, and damping of an exciton),[1] their dependence on the form and type of heterostructure,[2] and the change in these parameters under external actions.[3]

However, the analysis of the reflection spectra from quantum wells (QWs) is sometimes complicated by the strong background reflection from the surface of the sample, masking the signal from the QWs. One way to solve this problem is to exploit the Brewster effect, when the spectrum is measured with inclined incidence of light on the sample at an angle close to the Brewster angle and the surface reflection is thereby minimized.[1] Modulation methods, for which the measured quantity is the derivative of the spectrum with respect to any excitonic parameter, are also widely used: electroreflection, photoreflection, piezoreflection, thermoreflection, and so on.[4] These methods all require specially prepared samples: doping of the substrate and preparation of contacts, built-in electric or piezoelectric field, and so forth. Besides the technological difficulties of such preparation, for many structures this is virtually impossible to do.

The problems associated with sample choice and preparation can be avoided by using a magnetic field to modulate the spectra. This possibility has been successfully employed by a number of investigators,[5,6] but the difficulties of this approach have also been indicated in these same works. In the standard modulation methods, the magnitude of the disturbance must be varied with a sufficiently large amplitude and frequency, which for a magnetic field is difficult because of the sluggishness of the systems producing this field.

This letter proposes a method for measuring and analyzing differential magnetoreflection spectra such that it is not the external disturbance but rather the polarization of the recorded signal in an external magnetic field that is modulated, i.e., the spectrum of the degree of circular polarization of the reflected light $P_{\mathrm{circ}}=(R_{\sigma^+}-R_{\sigma^-})/(R_{\sigma^+}+R_{\sigma^-})$, where R_{σ^+} and R_{σ^-} are the reflection coefficients in σ^+ and σ^- circular polarizations, is measured.

2. In a constant magnetic field the ground state $e1-hh1$ $(1S)$ of an optically active exciton with a heavy hole in a QW splits into two Zeeman sublevels with $J=\pm 1$. Each sublevel can interact only with the electromagnetic wave corresponding to circular polarization (right- or left-hand). In this case, the circularly polarized component of the reflection coefficient contains a contribution only from one sublevel and is characterized by a characteristic set of excitonic parameters, which, generally speaking, is different from the corresponding set for the second Zeeman sublevel.

If the excitonic parameters for the two polarizations differ very little, then in the approximation linear in the change in the parameters ($\Delta\omega_0$, $\Delta\Gamma$, and $\Delta\Omega_{LT}$) the reflection polarization signal can be represented in the form

$$P_{\mathrm{circ}}=\frac{R_{\sigma^+}-R_{\sigma^-}}{R_{\sigma^+}+R_{\sigma^-}}=\frac{\Delta R_{\pm}}{2R}=\frac{1}{2R}\left(\frac{\partial R}{\partial\Gamma_0}\Delta\omega_0+\frac{\partial R}{\partial\Gamma}\Delta\Gamma+\frac{\partial R}{\partial\omega_{LT}}\Delta\omega_{LT}\right). \tag{1}$$

This formula, together with the expression for the reflection coefficient of a structure with QWs[1]

$$R=R_b\left\{1+\frac{4n\sin\delta}{n^2-1}\,\frac{\omega_{LT}}{\Gamma}\,\frac{\sin\Phi+x\cos\Phi}{x^2+1}\right\},\quad x=\frac{\omega-\omega_0}{\Gamma}, \tag{2}$$

can be used for numerical analysis of differential magnetoreflection spectra. In Eq. (2) R_b is the reflection coefficient of the surface of the structure, n is the background refractive index, $\delta=KL_z$ is the phase shift of the light wave on passing through the QWs, $K=(\omega/c)n$ is the wave vector of the light, L_z is the width of the quantum well, $\Phi=2Kd$ is the phase shift of the light wave on passing from the surface of the structure to the quantum well and back, d is the thickness of the layer of the structure of the surface to the QW, ω_0 is the resonance frequency of the transition, ω_{LT} is the longitudinal–transverse splitting, and Γ is the damping. These are the parameters which describe the excitonic contribution to the reflection signal.

The characteristic form of the reflection and differential reflection contours calculated according to Eqs. (1)–(2) with a change in ω_0, ω_{LT}, or Γ for $\Phi=\pi$ and $\Phi=\pi/2$ is displayed in Fig. 1. One can see that there is a strong difference in the form of the differential contours with a change in the different parameters. This makes it

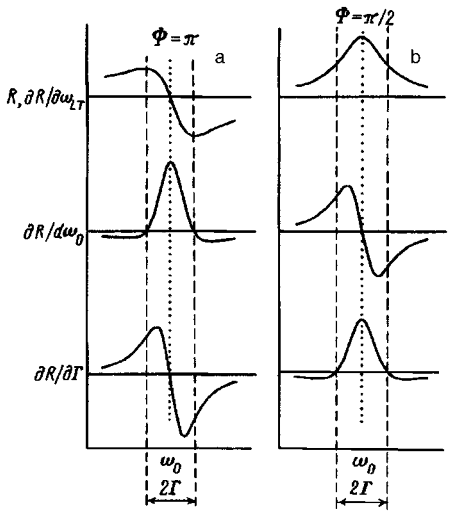

FIG. 1. Form of the excitonic reflection and differential magnetoreflection contours calculated from Eqs. (1) and (2) assuming that the contribution of only one term in Eq. (1) dominates for two values of the phase shift Φ.

possible to distinguish the contribution of each term on the right-hand side of Eq. (1) to the measured differential spectrum and thereby to decrease the number of adjustable parameters in analyzing the spectra.

The standard reflection spectrum alone is not always sufficient for reliable determination of the excitonic parameters. A differential spectrum makes it possible to determine more accurately the excitonic parameters describing the reflection spectrum (this is especially important for weak resonances) and also to determine additional parameters, for example, the excitonic g-factor, which describe the spectrum of the derivative of the reflection coefficient. If the magnetic field result only in the Zeeman splitting of the excitonic levels and has no effect on other excitonic parameters, then the differential magnetoreflection signal $P_{\rm circ}$ is proportional to the Zeeman splitting of the exciton $\Delta\omega_0=\mu g H$ (where μ is the Bohr magneton and g is the effective excitonic g-factor) and thereby the value of its g-factor. This makes it possible to measure the g-factor of an exciton by measuring the amplitude of the differential magnetoreflection signal $P_{\rm circ}$.

The expression (1) is also valid for the transmission coefficient, i.e., the method can be used to investigate the differential magnetotransmission spectra.

3. The measurements were performed in a glass helium cryostat at temperatures of 1.6 and 4.2 K. The magnetic field (up to 4.5 T) was produced with a superconducting solenoid at whose center the sample was placed. Unpolarized light from a KGM-12-100 halogen lamp was incident, after reflecting from the surface of the sample in a direction normal to the surface, on a quartz modulator operating in the $\lambda/2$-plate regime with a switching frequency of 50 kHz. A linear polarizer was placed behind the modulator. The signal was recorded in the photon counting mode with a two-channel scheme.[7] The noise level of the polarization signal is determined by fluctuations of the number of photons

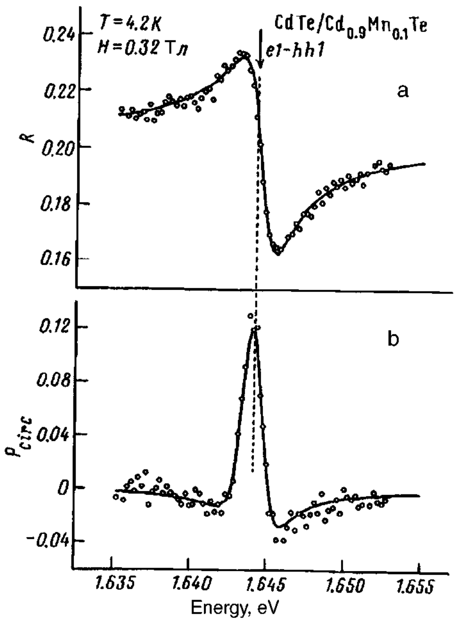

FIG. 2. Reflection (a) and differential magnetoreflection (b) spectra From a structure with a single 60-Å thick CdTe/Cd$_{0.9}$Mn$_{0.1}$Te quantum well near an excitonic resonance in a magnetic field $H = 0.32$ T. Dots — experiment, solid curve — calculation.

and equals $1/\sqrt{N^{\pm}} \propto 0.3\%$ for the characteristic number of recorded photons $\propto 10^5$ photon/s. This made it possible to measure the degree of polarization P_{circ} to within 0.1%.

Semimagnetic CdTe/Cd$_{0.9}$Mn$_{0.1}$Te and nonmagnetic CdTe/Cd$_{0.85}$Zn$_{0.15}$Te structures with quantum wells and a superlattice were used for the investigations. The samples were grown by molecular-beam epitaxy on undoped Cd$_{0.96}$Zn$_{0.04}$Te substrates. In structures based on Cd/TeCd$_{0.85}$Zn$_{0.15}$Te the energy of the excitonic resonance in the quantum well lies below the band gap of the substrate; this made it possible to investigate the transmission spectra of these structures.

4. The experimental reflection and differential magnetoreflection spectra from a structure with a single 60-Å wide CdTe/Cd$_{0.9}$Mn$_{0.1}$Te quantum well near a heavy-exciton resonance $e1-hh1$ in the QW are displayed in Fig. 2. Comparing this spectrum with the model spectra in Fig. 1 ($\Phi = \pi$), it can be concluded that the main contribution to the differential spectrum, as expected for semimagnetic structures, is due to the Zeeman splitting of the excitonic levels. Figure 2 displays the fitted curves which were constructed using the expressions (1) and (2) with the parameters $\omega_0 = 1.646$ eV, $\omega_{LT} = 1.7$ meV, and $\Gamma = 1.05$ meV. The good quality of the initial spectrum made it possible to determine all excitonic parameters (ω_0, $\omega_{LT,}$ and Γ) and to use the differential spectrum only for determining the effective excitonic g-factor. Curves of the splitting versus the magnetic field are displayed in Fig. 3 for a set of semimagnetic quantum wells

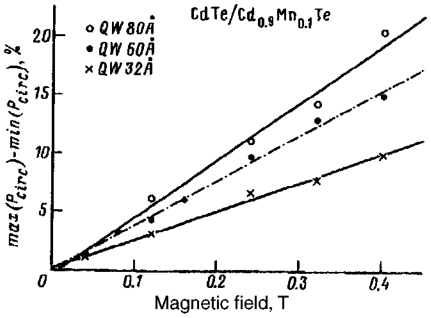

FIG. 3. Amplitude of the differential magnetoreflection contour as a function of the external magnetic field for semimagnetic structures with quantum wells of different width (the amplitude of the contour $\max(P_{\mathrm{circ}}) - \min(P_{\mathrm{circ}})$ is proportional to the Zeeman splitting of an excitonic resonance).

of different width. For all quantum wells, in the region of magnetic fields presented this dependence is nearly linear and its slope determines the effective exciton g-factor. The data on the excitonic parameters and g-factors which were found are summarized in Table I. The giant excitonic g-factors in semimagnetic heterostructures are due to exchange enhancement of the Zeeman splitting in magnetic semiconductors.[8] The increase in the effective g-factor with decreasing QW width (see Table I) is due to the large penetration of the carrier wave functions into the semimagnetic barriers in narrow QWs. This method can be used to measure the excitonic g-factors not only in semimagnetic but also in nonmagnetic heterostructures, for example, GaAs/GaAlAs or CdTe/CdZnTe. Indeed, the strength of the signal is $P_{\mathrm{circ}}(\omega_{LT}/\Gamma)g$, and it is therefore possible to obtain an appreciable differential magnetoreflection signal on account of both the large value of the g-factor and the high oscillator strength or small damping of the exciton.

5. The proposed method makes it possible to measure not only the excitonic g-factor, which determines the change in the resonance frequencies, but also other excitonic parameters and their change in a magnetic field $(\Delta\omega_{LT}, \Delta\Gamma)$. This problem arises in the investigation of the transmission and reflection spectra of structures with QWs containing a two-dimensional electron gas (2DEG). We investigated modulationally doped structures with CdTe/Cd$_{0.85}$Zn$_{0.15}$Te quantum wells. The structures consisted of ten 100-Å wide CdTe QWs separated by 450-Å wide Cd$_{0.85}$Zn$_{0.15}$Te barriers. The center of each barrier was doped with donors (In) to obtain an electron density of $5 \cdot 10^{10}$ cm^{-2} in each QW.

TABLE I. Excitonic parameters in CdTe/Cd$_{0.9}$Mn$_{0.1}$Te structures with quantum wells.

QW, Å	ω_0, eV	ω_{LT}, meV	Γ, meV	g
32	1.677	5.5	3.1	218
60	1.646	1.7	1.05	69
80	1.624	1.2	0.8	57

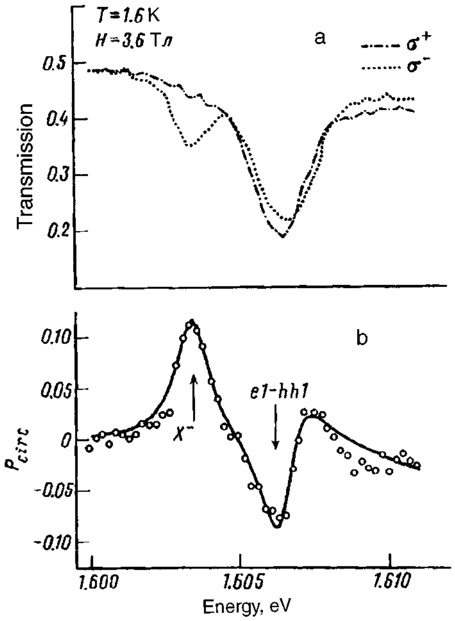

FIG. 4. a) Transmission spectra of a structure with CdTe/$Cd_{0.85}Zn_{0.15}Te$ quantum wells near an excitonic resonance in the magnetic field $H=3.6$ T for two circular polarizations σ^+ and σ^-. b) Differential magnetotransmission spectrum of this structure. Circles — experiment, solid curve — calculation.

Figure 4a shows the transmission spectrum of such a structure near an excitonic resonance in a magnetic field in two opposite circular polarizations σ^+ and σ^-. Two absorption lines are observed in the spectrum. The lines are associated with the excitation of a 1.606 eV heavy exciton $(e1-hh1)$ and with optical transitions in the state of a negatively charged exciton (trion) consisting of the bound state of an exciton and one additional electron with a binding energy of the order 3 meV (Ref. 9) (X^- in Fig. 4). Transitions with excitation of a trion are observed in only one polarization, viz., σ^-. This is due to the fact that for a trion a bound state exists only for a singlet, where two electrons in the trion have opposite spins.[9] In a sufficiently strong magnetic field, when all additional electrons occupy only the lower Zeeman sublevel, this results in a strong polarization of the trion absorption line.

It is interesting that the form of the excitonic absorption contour is not completely identical for the two circular polarizations. However, since these contours differ very little, it is not possible to establish reliably the difference of the excitonic parameters by analyzing these two spectra. This is easy to do by analyzing the differential magnetotransmission spectra. The differential magnetotransmission spectrum near the excitonic resonance in a QW measured in a magnetic field $H=3.6$ T is displayed in Fig. 4b. The signal near 1.603 eV is evidently due to the polarization of a trion absorption line, which is appreciable in the ordinary spectrum in Fig. 4a. Analyzing the signal near the exciton absorption line, it can be concluded that this signal is associated with the difference of the excitonic damping Γ for the two polarizations σ^+ and σ^-. The solid curve in Fig. 4b shows the result of fitting the experimental spectrum and the computed spectrum with the parameters $\omega_0 = 1.606$ eV, $\Gamma = 0.92$ meV, and $\omega_{LT} = 0.45$ meV in σ^+ polarization and $\omega_0 = 1.606$ eV, $\Gamma = 1.04$ meV, and $\omega_{LT} = 0.45$ meV in σ^- for an exciton and $\omega_0 = 1.603$ eV, $\Gamma = 0.7$ meV, and $\omega_{LT} = 0.09$ meV in σ^- for a trion; the trion is not observed in a magnetic field in σ^+ polarization. Therefore the analysis shows that in structures with quantum wells containing a low-density two-dimensional electron gas, exciton damping in a magnetic field depends on the spin state of the exciton. At the same time, the other excitonic parameters do not change much in the investigated range of magnetic fields. The difference of the excitonic damping in two polarizations increases with the magnetic field, saturating in fields of the order of 2 T. In our structures the maximum value equals 0.23 meV.

We attribute the observed dependence of the excitonic damping on the exciton spin to exchange scattering of an exciton by electrons. Indeed, in the presence of a 2DEG it is natural to assume that an appreciable fraction of the excitonic damping γ is associated with the scattering of an exciton by electrons from the 2DEG. Direct processes in such scattering are not spin-dependent, while the exchange processes, when the exciton exchanges an electron with the 2DEG, depend on the exciton spin. In a magnetic field, when electrons in the 2DEG are completely spin-polarized, the exchange contribution to the scattering is substantial only for excitons which contain an electron whose spin is oriented opposite to that of the electrons in the 2DEG.

6. In summary, this letter proposes a method of differential magnetoreflection (magnetotransmission) for investigating semiconductor heterostructures with quantum wells. The method was used to measure the excitonic g-factor in quantum wells with semimagnetic barriers based on CdTe/CdMnTe. It was found that the excitonic damping in QWs containing a low-density 2DEG in an external magnetic field depends on the spin state of the exciton. This dependence is associated with the contribution of exchange processes in exciton-electron scattering. Considering the fact that in the experimental structures the inhomogeneous width of the excitonic absorption line is of the order of the homogeneous width, the observed 20% difference of the excitonic damping indicates that the contribution of exchange processes to the exciton–electron scattering is comparable to the contribution of direct processes.

We thank the Russian Fund for Fundamental Research (Grant 95-02-04061a), INTAS (Grant 93-3657), and Ext and Volkswagen Stiftung for providing partial financial support for this work. We also thank E. L. Ivchenko for helpful discussions.

[a] e-mail: platon@semimag.ioffe.rssi.ru

---

[1] E. L. Ivchenko, P. S. Kop'ev, V. P. Kochereshko *et al.*, Fiz. Tekh. Poluprovodn. **22**, 784 (1988) [Sov. Phys. Semicond. **22**, 495 (1988)]; E. L. Ivchenko and G. E. Pikus, *Superlattices and Other Heterostructures. Symmetry and Optical Phenomena*, Springer Series in Solid State Sciences, Springer-Verlag, 1995, Vol. 110.

[2] E. L. Ivchenko, V. P. Kochereshko, P. S. Kop'ev *et al.*, Solid State Commun. **70**, 529 (1989); I. L. Aleiner, E. L. Ivchenko, V. P. Kochereshko *et al.*, Superlattices Microstruct. **13**, 237 (1993).

[3] E. V. Goncharova, V. P. Kochereshko, M. A. Yakobson *et al.*, JETP Lett. **61**, 894 (1995).

[4] M. Cardona, *Modulation Spectroscopy*, Suppl. 11 of Solid State Physics, edited by F. Seitz, D. Turnbull, and H. Ehrenreich, Academic Press, New York, 1969 [Russian translation, Mir, Moscow, 1972].

[5] R. P. Seĭsyan, *Spectroscopy of Diamagnetic Excitons* [in Russian], Nauka, Moscow, 1984.

[6] E. Oh, R. G. Alonso, and A. K. Ramdas, Solid State Commun. **82**, 969 (1992).
[7] A. P. Balatsyuk, V. A. Novikov, and V. G. Fleĭsher, Prib. Tekh. Éksp. No. 1, 171 (1976).
[8] J. A. Gay, R. Planel, and G. Fishman, Solid State Commun. **29**, 435 (1979).
[9] K. Kheng, R. T. Cox, Y. Merle d'Aubigne *et al.*, Phys. Rev. Lett. **71**, 1752 (1993).

Translated by M. E. Alferieff

Character of electron reflection at a normal metal–Peierls semiconductor boundary

S. N. Artemenko[a] and S. V. Remizov
Institute of Radio Engineering and Electronics, Russian Academy of Sciences, 103902 Moscow, Russia

(Submitted 11 November 1996; resubmitted 25 November 1996)
Pis'ma Zh. Éksp. Teor. Fiz. **65**, No. 1, 50–55 (10 January 1997)

The reflection of electrons incident from a normal metal on the boundary of the metal with a quasi-one-dimensional conductor containing a charge-density wave (CDW) is investigated theoretically. It is shown that the reflection is not of an Andreev character but rather of a Bragg character. This is due to the fact that the CDW is actually an electronic crystal, and its wave vector is a reciprocal lattice vector of the electronic crystal. The ratio of the intensities of the standard and Bragg reflection depends on the phase of the CDW. © *1997 American Institute of Physics.* [S0021-3640(97)00901-8]

PACS numbers: 61.16.Bg, 72.15.Nj, 42.79.Dj

It is well known (see, for example, Ref. 1) that an electronic crystal — a charge or spin density wave whose motion under the influence of an electric field is associated with a collective mechanism of conduction — forms in quasi-one-dimensional conductors below the Peierls transition temperature. For definiteness, in what follows we shall study a charge-density wave (CDW), but the results obtained are also applicable to the case of a spin density wave.

There exists a formal analogy between Peierls semiconductors (PSs) and superconductors, since in both cases the condensed state is described by an order parameter $\Delta=|\Delta|\exp i\varphi$ whose amplitude determines the energy gap in the single-particle excitation spectrum and the derivative of whose phase (in a superconductor with respect to the coordinate and in a Peierls semiconductor with respect to time) is proportional to the contribution of the condensed electrons to the electric current density. A CDW can be graphically imagined as a condensate consisting of bound pairs of electrons and holes whose momenta differ by the magnitude of the wave vector of the CDW. By analogy to superconductors, where the condensate consists of pairs of electrons with opposite momenta and Andreev reflection is observed at a boundary with normal metal,[2] it should be expected that even the reflection of electrons with energy close to the Fermi energy from the normal metal–PS boundary $(N-P)$ has an unusual character. It has been concluded in theoretical works[3,4] that an electron relected from a PS onto which it was incident from a normal metal moves along the same trajectory along which it was incident on the PS, i.e., the reflection is similar to Andreev reflection, but in contrast to a superconductor the sign of the charge of the incident quasiparticle does not change. The observation of features in the resistance of a contact of a PS with a normal metal which were interpreted as a manifestation of the Andreev-type reflection predicted in Refs. 3 and 4 was recently

© 1997 American Institute of Physics

reported in Ref. 5. In our view, a reflection in which the reflected particle moves along the same trajectory cannot appear at a metal–PS contact, since a quasiparticle in the PS is a superposition of two electrons with momenta differing by the wave vector of the CDW and not with opposite momenta. We shall show that the momentum component parallel to the interface can either be conserved (standard reflection) or change by an amount equal to the CDW wave vector component parallel to the interface (Bragg reflection from an electronic crystal).

We shall be interested in the reflection of electrons with energies of the order of k_BT or Δ near the Fermi energy, since such electrons will determine the conductivity in structures containing a PS.

We consider first the reflection of electrons at the interface between a normal metal and a PS, whose electronic structures differ from one another only by the presence of a CDW in the PS, occupying the space $x>0$. This model will enable us to investigate reflection from a CDW in a pure form, since there will be no reflection, associated with the difference in the energy structure of the crystals and having no relation with the CDW, from the interface. The fact that the CDW was formed in only a part of the crystal could be due to the fact, for example, that the electron-phonon interaction constant vanishes for $x<0$.

To calculate the electronic wave functions in a PS it is often convenient to employ the self-consistent field approximation equations of the Bogolyubov–de Gennes type for superconductors, as was done, for example, in Ref. 3. The envelopes $u(\mathbf{r})$ and $v(\mathbf{r})$ — the amplitudes determining the contribution of the states belonging to opposite sheets of the Fermi level, shifted by the wave vector $\mathbf{Q}$ of the CDW, to the total wave functions — serve as the elements of the spinor wave functions. In calculating the wave functions in a nonuniform system by matching at the interface, the total wave functions

$$\psi = u e^{i\mathbf{Q}\cdot\mathbf{r}/2} + v e^{-i\mathbf{Q}\cdot\mathbf{r}/2}, \tag{1}$$

which are solutions of the Schrödinger equation with the potential of the CDW, prescribed for $x>0$ as $2|\Delta|\cos(\mathbf{Q}\cdot\mathbf{r}+\varphi)$, must be matched. The matching of the envelopes u and v at the interface in the case of a CDW gives, generally speaking, an incorrect result.

Let the conducting chains be directed along the x axis and let the electronic spectrum of the quasi-one-dimensional conductor in the normal state have the form $E_N = p_x^2/2m + E_\perp(\mathbf{p}_\perp)$, where $|E_\perp| \ll E_F$ and $E_F = p_{xF}^2/2m$ is the Fermi energy. For definiteness, we shall consider the case when the wave vector of the CDW possesses the components $\mathbf{Q} = (2k_F, Q_y, 0)$. Then in the Peierls state the spectrum has the form $E_P = \eta \pm \sqrt{\xi^2 + |\Delta|^2}$, where $\xi = [E(\mathbf{k}) - E(\mathbf{k}-\mathbf{Q})]/2$, $\eta = [E(\mathbf{k}) + E(\mathbf{k}-\mathbf{Q})]/2$, and the relation between u and v in Eq. (1) is determined by $u = -\Delta v/(\xi + \sqrt{\xi^2 + |\Delta|^2})$. If the energy is measured from the Fermi energy $|\epsilon| = |E - E_F|$ is less than $|\Delta|$, then in the state with the CDW $|u| = |v|$ to within corrections of order Δ/E_F. It follows from the form of Eq. (1) that as a result of matching the solutions at $x=0$ it will turn out that, to the same accuracy, the amplitudes u and v, which in the normal metal correspond to the amplitudes of the incident and reflected waves, are of the same absolute magnitude. Therefore if the wave vector of the CDW possesses a component Q_y parallel to the interface, then the corresponding component of the electron momentum will change by Q_y on reflection.

We shall now calculate, by matching the wave functions, the reflection coefficient, neglecting the coordinate dependence of the energy gap near the interface as a result of the proximity effect. Let us assume, for simplicity, that on formation of a CDW the period is doubled in a direction perpendicular to the conducting chains, i.e., $2Q_y$ corresponds to a reciprocal-lattice vector. For $x<0$ we seek the wave function in the form

$$\psi=[e^{ik_x x}+Ae^{-ik_x x}+Be^{-ik_x x+iQ_y y}]e^{i(k_y y+k_z z)}, \tag{2}$$

where the first term describes the incident wave, the second term describes the standard reflection, and the third term describes Bragg reflection. For $x>0$ the wave function must be a linear combination of functions of the form (1), which describe states possessing along the y axis momentum components k_y and k_y+Q_y and the same energy as the state (2). Strictly speaking, the wave functions in the form of plane wave combinations considered above can be equated only if the electronic structure in the N and P regions is the same and the Bloch periodic factors are identical for $x>0$ and $x<0$. Nonetheless, to understand qualitatively the effect of the difference of the electronic spectra in the N and P regions, we shall also discuss the result of the matching for the case when the electronic spectra on both sides of the interface are different.

The expressions for the reflection coefficient R in the general case are quite complicated. For this reason, we confine our attention to the limiting case of weak three-dimensionality of the spectrum in the conductor with the CDW and we neglect terms of the order of $E_\perp/\epsilon$. For the case when the electronic structure is the same to the left and right of the boundary, we obtain for the ratio of the standard and Bragg reflection intensities

$$|A/B|^2=(|\Delta|\sin\varphi/E_F)^2. \tag{3}$$

Therefore, in accordance with what we have said above, $|A|\ll|B|$ and Bragg reflection, where the parallel component of the momentum changes by Q_y, dominates. We also note that the relation (3) depends on the phase of the CDW. For $|\epsilon|<|\Delta|$ the reflection coefficient $R=1$, and for $|\epsilon|>|\Delta|$ we obtain $R=|\Delta|^2/(|\epsilon|+\xi)^2$, where $\xi=\sqrt{\epsilon^2-|\Delta|^2}$.

We now consider the case when the effective masses along the x axis are different in the materials to the left and right of the interface. Then

$$|A/B|^2=\frac{(m_1-m_2)^2}{4m_1m_2}\begin{cases}\sin^2(\varphi+\varphi_0) & \text{for } |\epsilon|<|\Delta| \\ (\epsilon/|\Delta|)^2-\cos^2\varphi & \text{for } |\epsilon|>|\Delta|\end{cases}, \tag{4}$$

where $\varphi_0=\tan^{-1}(\xi/\epsilon)$. For $m_1=m_2$, when the answer in Eq. (4) vanishes, the terms of order 1 in the ratio $|A/B|^2$ cancel and therefore the small terms of the order of $(|\Delta|/E_F)^2$, which result in the formula (3), must be taken into account. Therefore, when the electronic spectrum of the crystals on different sides of the interface is different, the standard reflection, where the angle of incidence equals the angle of reflection, is added to the Bragg scattering, and the intensities of both types of scattering are of the same order of magnitude and their ratio depends on the phase of the CDW. If it is assumed that an isotropic metal fills the space $x<0$, then one obtains an expression differing from expression (4) by the fact that the effective mass m_1 in the N region is replaced by $m_1/\cos\theta$, where θ is the angle of incidence of the electron. Of course, this result is not quantitative, since in matching the wave functions we neglected the periodic Bloch factors in them. Taking account of the real crystal structure would have resulted in the appearance of terms in the expansion of the wave function in a Fourier series in the coordinate which correspond to a change in the momentum by an arbitrary reciprocal-lattice vector of both the main and electronic crystals, as a result of which reflection would have also appeared in other directions corresponding to Bragg scattering.

Since the phase of the CDW can change when an electric field directed along the conducting chains is applied to the PS, the dependence of the character of the reflection on the phase of the CDW can be used for experimental investigation of N–P contacts.

We note one other interesting feature of reflection from an N–P contact. This feature is reminiscent of the properties of a normal metal–superconductor contact. As is well known, in a thin layer of normal metal of thickness d bordering a superconductor, bound states with an energy splitting of the order of $\varepsilon_0 = \pi\hbar v_F/d$ (here $v_F = p_{xF}/m$) appear at energies $|\epsilon| < |\Delta|$ as a result of the Andreev reflection from the superconductor. A similar quantization also appears in a normal metal in contact with a PS if the thickness d of the normal metal is less than the mean-free path length. The simplest method for investigating such quantization is to calculate the density of states with the aid of the quasiclassical equations for the momentum-integrated Green's functions, which were employed for investigating the transport properties of PSs.[6,7] For our purposes it is sufficient to solve an equation for the retarded Green's function neglecting the collision integral, in which case this equation has the very simple form

$$i\hbar v \frac{d\hat{g}}{dx} + (\tilde{\epsilon}\sigma_z + \hat{\Delta})\hat{g} - \hat{g}(\tilde{\epsilon}\sigma_z + \hat{\Delta}) = 0, \tag{5}$$

where the Green's function $\hat{g}$ is a 2×2 matrix with respect to the index corresponding to opposite sheets of the Fermi surface which are displaced by the wave vector $\mathbf{Q}$ of the CDW, $\tilde{\epsilon} = \epsilon - \eta(\mathbf{p}_\perp)$, $\hat{\Delta} = i|\Delta|(\sigma_y \cos\varphi + \sigma_x \sin\varphi)$, and σ_a are the Pauli matrices. Assuming once again that $|\Delta|$ vanishes abruptly for $x<0$ and that the normal metal occupies the region $-d<x<0$, we solve Eq. (5) with the boundary condition $\mathrm{Tr}\,\sigma_x g(0) = 0$ at the boundary of the normal metal with the vacuum. From Eq. (5) we obtain for the function $g = \mathrm{Tr}(\sigma_z \hat{g})$, whose real part determines the density of states, in the normal region

$$g = (\xi + i\tilde{\epsilon}t)/(\tilde{\epsilon}t + i\xi), \tag{6}$$

where $t = \tan(2\tilde{\epsilon}d/\hbar v_F + \varphi)$ and it must be assumed that ξ is an analytic function of ϵ in the upper half-plane. The off-diagonal components of $\hat{g}$ do not vanish even in the normal region, where they oscillate as $\exp(2i\tilde{\epsilon}d/\hbar v_F)$, since the decay length for them equals the mean-free path length and is greater than the thickness of the normal region. In an accurate calculation, we would have to take account of the lowering of the energy gap, which changes the shape of the potential well, in the PS at distances of the order of $\hbar v_F/|\Delta|$, which happens as a result of the proximity effect. This lowering is due to perturbations of the off-diagonal components of $\hat{g}$ in the region of the PS near the contact, but the change in the shape of the potential well does not affect the qualitative conclusions and we shall neglect it.

One can see from Eq. (6) that the density of states in the normal metal is an oscillating function of the phase of the CDW as well as of the energy and thickness of the normal region. For energies $|\epsilon|<|\Delta|$ at which bound states appear the density of states has the form

$$N(\epsilon)=\pi\langle(|\xi|+\widetilde{\epsilon}t)\delta(\widetilde{\epsilon}t-|\xi|)\rangle. \tag{7}$$

Here $\langle\ldots\rangle$ indicates averaging over $\mathbf{p}_{\perp}$. At energies much less than $|\Delta|$ formula (7) reduces to

$$N(\epsilon)=\varepsilon_0\langle\delta(\widetilde{\epsilon}-(2n+1)\varepsilon_0)\rangle,$$

where n is a positive integer.

Therefore, according to Eq. (7), the electron spectrum in the N layer consists of bands of width $E_{\perp}$ (the width, determined by the function $\eta(\mathbf{p}_{\perp})$, of the electron energy band in the perpendicular direction). If the electron spectrum is strongly one-dimensional $(E_{\perp}<\varepsilon_0)$, then the allowed energy bands are separated by regions of forbidden energies, otherwise they overlap and the energy dependence of the density of states is of a stepped form. An estimate gives $\varepsilon_0\approx 70$ K for $v_F=3\cdot 10^7$ cm/s and $d=0.1$ μm. At sufficiently low temperatures $(T<\varepsilon_0,\ E_{\perp})$ energy quantization can be observed in measurements of the conductivity of the normal region in the contact plane or in measurements of the density of states performed with the aid of tunneling or point contacts to the normal region. The application of an electric field in the direction of the chains changes the phase of the CDW, and for this reason, according to Eq. (7), the field should influence the density of states. To observe quantization, the width of the contact should not exceed the phase correlation length, since the phase of the CDW depends on the coordinates as a result of impurity pinning.

It was assumed above in the analysis of quantization that with the exception of the presence of the CDW for $x>0$ the electronic spectrum is the same on both sides of the contact. The effect of the differences in the electronic spectrum can be estimated by matching the wave functions, as done in the investigation of reflection. It is found that in the case of a contact of two different quasi-one-dimensional metals with $|k_{xF}^N-k_{xF}^P|\ll|k_{xF}^N+k_{xF}^P|$, where k_{xF}^N is the Fermi wave vector in the normal region and k_{xF}^P is the Fermi wave vector in the PS, the quantization condition is obtained if the argument of the tangent $2\widetilde{\epsilon}d/(\hbar v_F)$ in formula (7) is replaced by $\widetilde{\epsilon}_N d/(\hbar v_F)+2(k_{xF}^N-k_{xF}^P)d$, where the dependence of the energy on $\mathbf{p}_{\perp}$ in the normal region appears in $\widetilde{\epsilon}_N$ in the same way as in the similar dependence in $\widetilde{\epsilon}$ for a PS. Therefore the thickness of the N region enters the quantization condition not only in the form ϵ_0 but also in the form of the product $(k_{xF}^N-k_{xF}^P)d$, which for large differences in k_{xF} should blur the quantization effects even as a result of small variations of the thickness d.

Thus we have found that when electrons incident from a normal metal onto the interface with a PS are reflected, the component of their wave vector parallel to the interface is either conserved or changes by an amount equal to the projection of the wave vector of the CDW on the contact plane. The intensity of different types of reflection depends on the phase of the CDW and therefore can change when an electric field is applied. Specifically, the reflection of electrons from the region with a Peierls gap under certain conditions can result in quantization of the energy spectrum of the electrons near the Fermi energy.

We thank V. A. Volkov for a discussion of this work and also I. G. Gorlova and A. A. Sinchenko for a discussion and for familiarizing us with the experimental data prior to publication. This work is supported by Russian Fund for Fundamental Research (Grant 95-02-05392) and MTP ''Physics of Solid-State Nanostructures'' (Grant 1-018).

[a] e-mail: Art@mail.cplire.ru

---

[1] G. Grüner, *Density Waves in Solids*, Addison-Wesley, Reading, 1994.
[2] A. F. Andreev, Zh. Éksp. Teor. Fiz. **46**, 1823 (1964) [Sov. Phys. JETP **19**, 1228 (1964)].
[3] A. L. Kasatkin and É. A. Pashitskiĭ, Fiz. Nizk. Temp. **10**, 640 (1984) [*sic*].
[4] A. L. Kasatkin and É. A. Pashitskiĭ, Fiz. Tverd. Tela (Leningrad) **27**, 2417 (1985) [Sov. Phys. Solid State **27**, 1448 (1985)].
[5] A. A. Sinchenko, Yu. I. Latyshev, S. G. Zybtsev *et al.*, JETP Lett. **64**, 285 (1996).
[6] S. N. Artemenko and A. F. Volkov, Zh. Éksp. Teor. Fiz. **81**, 1872 (1982) [Sov. Phys. JETP **54**, 992 (1982)].
[7] S. N. Artemenko and A. F. Volkov, *Charge Density Waves in Solids*, edited by L. Gor'kov and G. Grüner, Elsevier, Amsterdam, 1989, Chapter 9.

Translated by M. E. Alferieff

Appearance of a band of delocalized D^- states in uncompensated silicon in an electric field

A. P. Mel'nikov, Yu. A. Gurvich, L. N. Shestakov, and E. M. Gershenzon
Moscow Pedagogical State University, 119882 Moscow, Russia

(Submitted 25 November 1996)
Pis'ma Zh. Éksp. Teor. Fiz. **65**, No. 1, 56–59 (10 January 1997)

The impurity photoconductivity spectra of uncompensated silicon at liquid-helium temperatures under conditions of strongly suppressed background radiation (background) are studied in different electric fields E. It is established that the delocalization arising in the D^- band as E increases is not associated with any changes of the fluctuation potential and is due to the direct action of the field E. A delocalization band of finite width appears abruptly at a critical value E_c ($\sim$100 V/cm) of E. The critical field E_c increases with the density of charged centers in the sample. © *1997 American Institute of Physics.* [S0021-3640(97)01001-3]

PACS numbers: 72.40.+w, 73.20.Jc, 61.72.Ss

1. In crystalline germanium and silicon delocalization of the D^- states appears in certain intervals of the majority impurity density N and compensations K. Thermal excitation of carriers to the mobility threshold ϵ_μ from the band of ground states results in the so-called ϵ_2 conductivity. The appearance of delocalization is an Anderson transition. It occurs when the ratio I/W reaches a certain value. Here I is the energy overlap integral; its value is determined by the asymptotic wave function of a D^- center at large distances, i.e., the radius a of the D^- state: $I \sim \exp(-2R/a)$, where R is the average intercenter distance. The energy variance W of the D^- states is ordinarily determined by the fluctuations of the Coulomb potential which appear as a result of the presence of a compensating impurity.[1]

In the presence of an electric field E, the asymptotic behavior of the wave functions at quite large distances changes radically: The bound states of an electron in a well of finite depth become unbound (formally — in an arbitrarily weak field E). This suggests that for some value $E = E_c$ delocalized states — field-induced delocalization — appear in the spectrum of electrons localized on randomly distributed centers. Theoretical investigations confirmed this conjecture, though the question of determining the threshold field E_c in the three-dimensional case is not entirely clear (see Ref. 2 and the references cited therein). The discovery of field-induced delocalization is of fundamental importance.

In our previous work[3] it was discovered that as E increases, delocalization in the D^- band of uncompensated crystalline silicon and a mobility threshold ϵ_μ appear at $E = E_c$ and as E increases further, the mobility threshold shifts substantially in the direction of lower energies. This conclusion was reached on the basis of a study of the evolution of the impurity photoconductivity (PC) spectra with increasing field E.

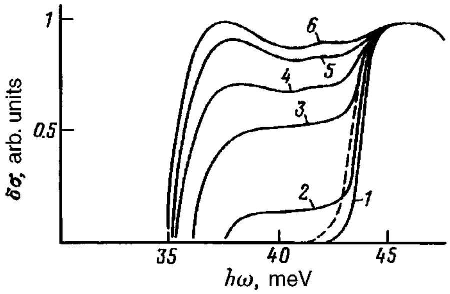

FIG. 1. Photoconductivity spectra in an electric field: Solid lines — background Φ_1; E, V/cm: *1* — 108, *2* — 110, *3* — 120, *4* — 130, *5* — 140, *6* — 150; dashed line: background Φ_2, $E=120$ V/cm.

In experiments studying the PC spectra, besides monochromatic radiation, background radiation always falls on the sample. In our case this background results in carrier detachment from the neutral centers and filling of the D^- states via an unoccupied band. The carriers that move along the unoccupied band and along the states of the D^- band produce a current. The rest of the carriers form complexes with charged centers or with groups of neutral centers. The additionally arising charged impurities and complexes produce a fluctuation potential in the sample and increase the energy variance W of the states. In Ref. 3 the background was substantial and the charge density produced by the background was quite high. Photodetachment of carriers from the complexes resulted in the appearance of low-frequency PC ($\hbar\omega=5-15$ meV). As E increased, the complexes decayed (the low-frequency part of the PC vanished) and the potential fluctuations and hence also the value of W decreased. Therefore it was impossible to rule out in the situation occurring in Ref. 3 the appearance of Anderson delocalization as E increased, and the results of Ref. 3 cannot be unequivocally interpreted as a manifestation of field-induced delocalization.

2. Our aim in the present work was to obtain reliable confirmation of the existence of field-induced delocalization. For this, it was necessary to rule out the influence of complexes. Experiments similar to those described in Ref. 3, except that cold Si:Ga, Si:As, and black polyethylene filters were placed in front of the sample, were performed. The background radiation with $\hbar\omega>45$ meV could be suppressed by a factor of up to 10^5 (and, correspondingly, the resistance of the sample could be increased) by varying the thickness of the filters and the impurity density in them. In this case, the range $\hbar\omega<45$ meV remained practically open. In this situation the population of the D^- states was decreased substantially, and the destruction of the D^- centers and complexes as a result of electron photodetachment decreased very little. The transmission of the system of filters was determined with a Ge bolometer; the PC spectra were normalized to the spectral distribution of the photons.

3. The PC spectra for a Si:B sample ($N=1.6\cdot10^{16}$ cm^{-3}, $K=10^{-4}$) with different values of E at temperature $T=4.2$ K are displayed in Fig. 1. The dark conductivity in this sample is less than 10^{-10} S/cm for small values of E. The solid curves in Fig. 1 were obtained for the case of a minimal background (Φ_1). For $E<E_c$ photoconductivity due to photoionization of the impurities ($\hbar\omega\geqslant45$ meV) is observed. For $E=E_c=110$ V/cm

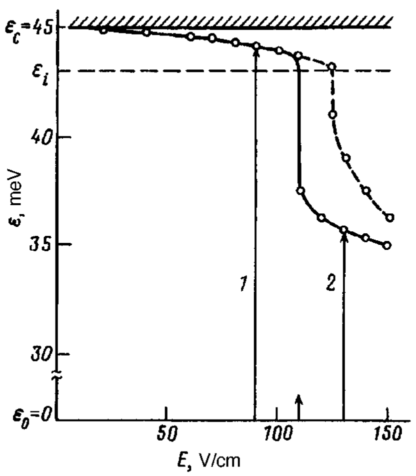

FIG. 2. Threshold $\epsilon_\mu(E)$: Solid line — background Φ_1; dashed line — background Φ_2. The arrows indicate transitions: *1* — $E<E_c$, *2* — $E>E_c$.

a leftward shift of the PC edge $\hbar\omega_t$ is observed: PC appears for $\hbar\omega<45$ meV. The magnitude of this PC increases with E, and the PC edge shifts to lower values of $\hbar\omega$. We note that the PC edge at $E=E_c$ shifts abruptly by ~ 6 meV. We underscore that the low-frequency PC is not observed for $E<E_c$. The latter circumstance is what mainly distinguishes the present results from those of Ref. 3.

The dependence of the PC edge on E is displayed in Fig. 2 (solid curve *1*). One can see that for $E>E_c$ the dependence of $\hbar\omega_t$ on E becomes weaker and the shift reaches 10 meV for $E=150$ V/cm.

The dashed curve in Fig. 1 represents the PC spectrum at $E=120$ V/cm for a background $\Phi_2\sim 300$ times stronger than Φ_1 (and ~ 10 times weaker than in Ref. 3). One can see that at Φ_2 the shift of the PC edge is still absent in such a field, while for Φ_1 the shift reaches 7 meV in the same fields. In the case of Φ_2 a weak signal is observed in the low-frequency part of the spectrum (not shown in the figure). The dashed curve in Fig. 2 also shows the dependence of the PC edge for Φ_2. One can see that the curve is shifted to higher values of E by ~ 15 V/cm and the E dependence is smoother.

4. Let us now discuss the results obtained. For $E<E_c$ the PC edge $\hbar\omega_t$ is determined by a transition: The ground state of the impurity ($\epsilon_0=0$) is the bottom of the unoccupied band ϵ_c: $\hbar\omega_t=\epsilon_c(E)$. According to Ref. 3 , in the presence of a mobility threshold in the D^- band $\epsilon_\mu(E)<\epsilon_c(E)$the PC edge $\hbar\omega_t$ is determined by a transition to the mobility threshold $\epsilon_\mu(E)$: $\hbar\omega_t=\epsilon_\mu(E)$. Therefore the evolution of the PC spectrum as E increases reflects the appearance and displacement of the mobility threshold $\epsilon_\mu(E)$.

The absence of PC in the band $\hbar\omega=5$–15 meV at Φ_1 shows that the density of complexes in the sample is very low. Their destruction cannot greatly facilitate delocalization: According to our estimates, the density of charged centers for $E<E_c$ and

$\Phi=\Phi_1$ is close to the equilibrium value KN and can only increase as E increases (see below). For this reason, we believe that the results presented here attest to the fact that the presence of a quite strong field E in itself leads to the appearance of a band of delocalized states in the D^- band.

We call attention to an important feature of field-induced delocalization. It follows from Figs. 1 and 2 that for $E>E_c$ the mobility edge shifts downwards very sharply: The delocalization band expands abruptly. Having appeared, it immediately encompasses an energy interval that is two to three times greater than the binding energy of an isolated D^- center ($\epsilon_i\sim 2$ meV).

5. Increasing the background radiation (switching from Φ_1 to Φ_2) results in higher values of E_c. The jump in ϵ_μ in this case becomes smaller, and the maximum delocalization band apparently becomes narrower (the appearance of breakdown of shallow impurities impedes advancement to higher values of E). This is explained by the fact that for Φ_2 the background is stronger and, correspondingly, the density of charged centers is higher. The energy variance W increases and the D^- states become more localized. High values of E are now required in order for delocalization to appear. Therefore, comparing the results obtained with different filters, one can see that the Anderson and field-induced mechanisms of localization appear simultaneously.

We note that for $E>E_c$ impurity conductivity, which grows rapidly with E, appears in such samples. According to Ref. 4 , this conductivity is due to the appearance of electrons, which have detached from neutral impurity centers, in D^- states. This is evidently accompanied by an increase in the density of charged centers and therefore the fluctuations of the potential increase. Despite this, delocalization is observed clearly, i.e., the effect of the field is stronger than that of an increase in the variance W.

It is possible that this increase of the fluctuations is one reason why the threshold $\epsilon_\mu(E)$, after jumping sharply, changes more slowly and approaches a limiting value as E increases: The increase in the fluctuation variance and the field-induced mechanism of delocalization, which act in opposite directions, ‘‘balance’’ one another.

This work was supported by the Russian Fund for Fundamental Research (Grant 95-02-06289a).

[1] B. I. Shklovskiĭ and A. L. Éfros, *Electronic Properties of Doped Semiconductors*, Springer-Verlag, New York, 1984 [Russian original, Nauka, Moscow, 1979].
[2] T. R. Kirkpatrick, Phys. Rev. B **33**, 780 (1986).
[3] A. P. Mel'nikov, Yu. A. Gurvich, L. N. Shestakov, and E. M. Gershenzon, JETP Lett. **63**, 100 (1996).
[4] Yu. A. Gurvich, A. P. Mel'nikov, L. N. Shestakov, and E. M. Gershenzon, JETP Lett. **61**, 730 (1995).

Translated by M. E. Alferieff

Bias-field-induced spiral dynamic domains induced in iron garnet films

G. S. Kandaurova and A. A. Rusinov
Ural State University, 620083 Ekaterinburg, Russia

(Submitted 26 November 1996)
Pis'ma Zh. Éksp. Teor. Fiz. **65**, No. 1, 60–64 (10 January 1997)

The induction of an Anger state (AS) in a multidomain magnetic medium by a static bias magnetic field is observed. The properties of the spiral dynamic domains in the induced AS are substantially different from those of previously studied spiral domains.

© *1997 American Institute of Physics.* [S0021-3640(97)01101-8]

PACS numbers: 75.60.Ch, 75.50.Gg

It is well known[1,2] that a special excited state, termed in Ref. 3 an Anger state (AS), can be realized in iron garnet (IG) films placed in a spatially uniform, continuously acting, alternating magnetic field $H_{\sim}$. This state is observed in a definite range of amplitudes H_0 and frequencies f of the alternating field. In Refs. 1 and 2 it is referred to states of the autowave type.[4] An Anger state possesses at least two distinguishing features: 1) *self-organization* in a chaotically moving system of domains and formation of stable, ordered dynamic domain structures (DDSs), usually in the form of spirals, and 2) *self-generation* of periodic (quasiperiodic) processes, the main one being the appearance/disappearance of spiral dynamic domains (SDDs). The lifetime T_g of a SDD and the waiting time T_w of the formation of new SDD(s) are dynamical parameters of the AS.

Investigations of a large number of IG films[5] have shown that the AS is by no means observed in all samples. An unequivocal criterion for the realization of an AS has still not been determined. There is also no theory of the AS. A large amount of interesting experimental data has been accumulated. The factors which strongly influence the amplitude–frequency region $(H_0 - f)$ of the Anger state have been determined, it has been found that T_g and T_w depend on the frequency and amplitude of the alternating the field, the character of the evolution of an individual SDD over its lifetime has been determined,[6] the relation between the AS and the dynamical hysteresis properties of an IG film has been found,[7] etc.

The effect of a static magnetizing field (bias field H_b) on a SDD in the Anger state of a IG film was investigated in Ref. 3. It was shown that as the field H_b increases, the spirals become smaller and disappear, i.e., the AS is destroyed. The maximum value of H_b is a relatively small fraction of the amplitude H_0 of the alternating field (not more than 20%).

In the present work we have discovered that high bias fields H_b, comparable to or several times greater than H_0, can give rise to the formation of SDDs, whose behavior attests to the appearance of an AS, from chaos. We have termed this state an induced Anger state — AS(i). This effect has been observed in several IG films. We shall dem-

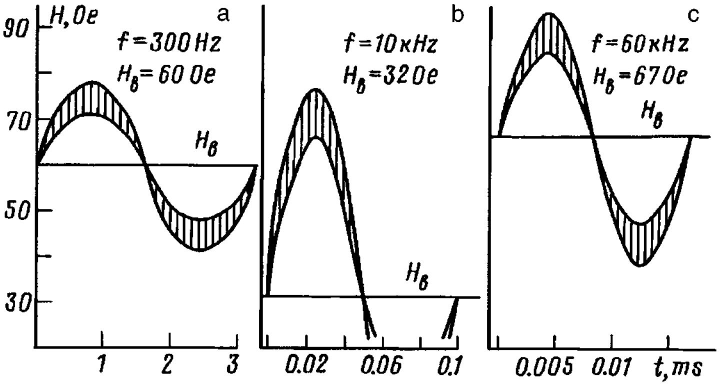

FIG. 1.

onstrate it for the example of a (111) $(YLuBi)_3(FeGa)_5O_{12}$ iron garnet film of thickness $L=16.6$ μm.

The film had the following parameters: The static saturation field $H_s=91$ Oe, the uniaxial perpendicular anisotropy field $H_A=11$ kOe, and the period of the initial labyrinthine domain structure $P_0=28.5$ μm. The domains were observed with the aid of the Faraday magnetooptic effect. Photographing was performed with an exposure time of 1 ms. The sample was placed at the center of a 6 mm in diameter alternating-field coil. The alternating field $H_\sim=H_0\sin 2\pi ft$ was oriented in a direction normal to the sample. The frequency f and amplitude H_0 were varied in the ranges $f=10^2$–10^5 Hz and $H_0=0$–100 Oe. A static magnetic field H_b with an intensity of up to 100 Oe was also applied in a direction normal to the film.

It should be especially underscored that in the entire experimental range of values of f and H_0 of the field $H_\sim$ and in the absence of the bias field H_b neither SDDs nor an AS were observed in this sample. Only chaotic DDSs of different kinds were formed. The situation changes radically in a sufficiently strong bias field H_b. Beautiful, stable, ordered structures in the form of SDDs, surrounded by dynamic domain chaos, arise for some combinations of f, H_0, and H_b. The SDDs ‘‘live’’ for a time T_g and disappear, after some time interval T_w new SDDs reappear, and so on. This is the characteristic indication of the Anger state, in this case AS(i). The chaos/order transition processes continue indefinitely as long as the experimental conditions remain unchanged.

We found three combinations of values of H_0, f, and H_b for which the AS(i) are most stikingly observed (Fig. 1). Acually, an AS(i) is realized not only for a given fixed value of each of these parameters but also in definite intervals ΔH_0, Δf, and ΔH_b. Therefore one must talk about three regions (H_0-f-H_b) where AS(i) are realized. The maximum ranges of variation of the intensity of the alternating field with some fixed values of the frequency f and bias field H_b from these three regions (H_0-f-H_b) can be seen in Fig. 1 (hatched parts of the sinusoid). It was found that these regions AS(i) are strongly separated along the frequency scale and fall, respectively, in the intervals $(0.1-1.2)$, $(5-16)$, and $(40-100)$ kHz. If all three parameters H_0, f, and H_b are

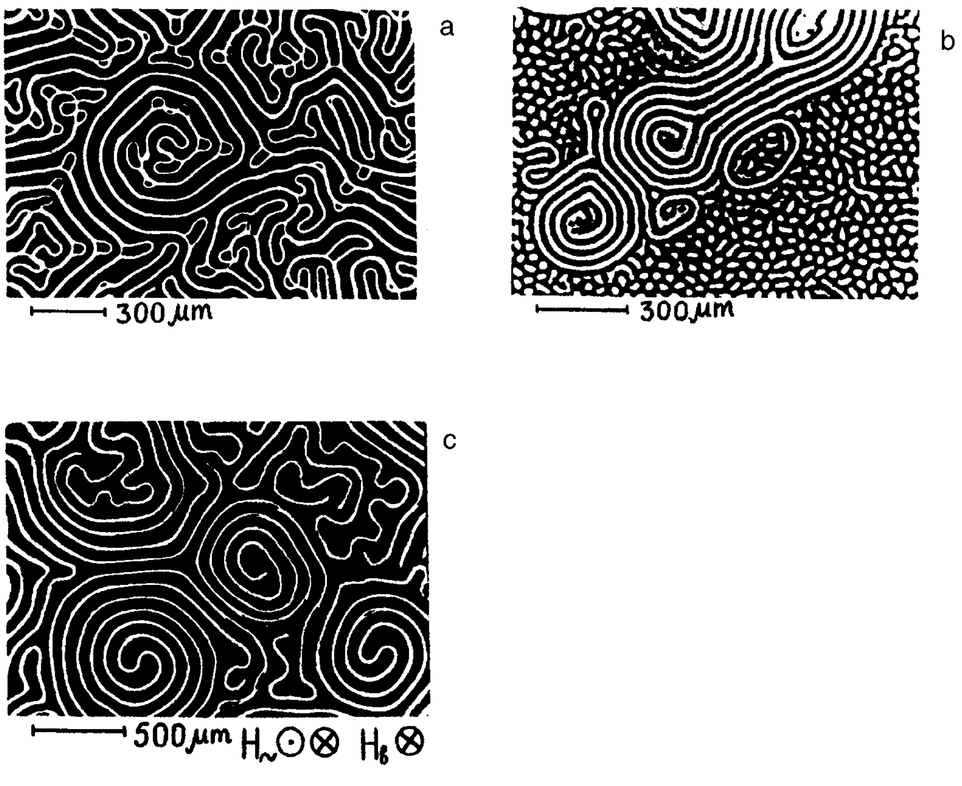

FIG. 2.

varied in the experiment, then, naturally, three-dimensional regions of existence of AS(i) must be studied. However, the present letter presents the results of an analysis of DDSs in three regions AS(i) for some selected values of H_b.

The characteristic patterns of DDSs with spiral domains from the indicated regions $(H_0 - f - H_b)$ are presented in Fig. 2. The photographs were obtained under experimental conditions corresponding to Fig. 1. The difference in the configuration of the SDDs and the domain chaos surrounding them is striking. But even more remarkable is the fact that the dynamic behavior of the spiral domains is very different in all three regions AS(i).

In the region AS(i)-1 mainly two-sleeve, long-lived SDDs with a small number of turns, of which the outer one is associated with the surrounding domain chaos, form (Fig. 2a). The distance between the turns is approximately two times greater than the period P_0. In the field $H_b = 60$ Oe the SDDs can spiral in different directions, both clockwise and counterclockwise. Such SDDs either stay in place throughout their lifetime T_g or drift very slowly with a velocity not exceeding 0.1 mm/s. The stripe domains in the turns at the periphery of the SDDs are immobile, while the stripe domains in the interior parts of the SDDs move about intensively. This motion is manifested in the photographs in Fig. 2a by the fact that at some locations the white domains have a contrast image of a small loop. This means that the position of domains with opposite amplitude values of the alternating field is captured over the exposure time. The white stripe domains become shorter at the top of the sinusoid (Fig. 1a) and longer at the bottom part. Therefore the velocity of a domain can be estimated according to the displacement of the domain (turn) over the exposure time. For $f = 300$ Hz and $H_0 = 14$ Oe the velocity is of the order of 0.1 m/s.

The most remarkable feature of AS(i)-1 is that it is possible to observe visually how the SDDs form gradually during a period of 3–4 s. The lifetime of such spirals equals, on the average, 7 s, but sometimes large, long-lived SDDs whose lifetime T_g reaches 3 min form. Then successive stages of the process of destruction of SDDs can be observed over a time of 1–2 s. Based on these observations, we introduced new dynamical parameters of AS(i) and SDDs — the formation time (T_b) and the destruction time (T_d). Thus far previous works have reported only that the SDDs appear and disappear practically instantaneously, abruptly.

In the region of AS(i)-2, single-sleeve SDDs with a relatively small core are formed (Fig. 2b). The turns of the spirals are packed quite densely, so that their period is only slightly greater than the period P_0 (by 1.2–1.3 times). In a bias field $H_b = 32$ Oe there is no predominant direction of twist of the spirals. Such SDDs are more dynamic than those in the AS(i)-1 region. They form much more rapidly (tenths of a second), live for a shorter time (3–4 s), and break down more rapidly (less than 1 s). Over the time T_g the SDDs do not stay in place. They move chaotically, ‘‘swimming’’ with a speed of 1–1.5 mm/s. Often systems consisting of two or three SDDs, connected by a S-shaped bond or a ‘‘ram’s horns’’ type bond, arise.[3] The SDDs are surrounded by chaos, consisting mainly of distorted cylindrical and stripe domains.

Large smooth one- and two-sleeve SDDs form in the region AS(i)-3 (Fig. 2c). The period of the turns in such spirals is at least two times greater than the period of the initial structure. In the field $H_b = 67$ Oe the two-sleeve SDDs wind predominantly clockwise and in the single-sleeve SDDs no clearly predominant direction of twist is seen. Dynamically, the SDDs in the region AS(i)-3 are even more mobile structures than those described above. They form more rapidly and decay more rapidly, so that it is difficult to estimate visually the time interval over which a stripe domain twists into a spiral or is ‘‘torn apart’’ by the surrounding chaos. The average lifetime of these SDDs equals 2 s. They intensively move, rotate, interact with one another, and so on. Outside this ($H_0 - f - H_b$) region only disordered SDDs from extended stripe domains are observed.

In summary, the strength of the static bias field, together with the frequency and amplitude of the alternating field, is the third parameter controlling the Anger state of multidomain magnetic films. It is natural to attribute the twisting of the stripe domains to the action of a gyrotropic force which deflects the end (top) of a moving domain in one or another direction. According to Ref. 8, this force is proportional to the velocity of the domain. This explains qualitatively the facts that as the field $H_b + H_0$ increases, the velocity increases and the gyrotropic forces become more effective and hence it becomes possible for SDDs to form under the conditions for which SDDs did not form in the absence of H_b. However, to explain the existence of several AS(i) regions with different spiral domains, a serious theoretical analysis, similar to the one presented in Ref. 9 for static spiral domains, is required.

This work is supported by the Russian Fund for Fundamental Research (Grant 96-02-16119a).

[1] G. S. Kandaurova and A. É. Sviderskiĭ, JETP Lett. **47**, 490 (1988).
[2] G. S. Kandaurova and A. É. Sviderskiĭ, Pis'ma Zh. Tekh. Fiz. **14**, 777 (1988) [Sov. Tech. Phys. Lett. **14**, 346 (1988)].
[3] G. S. Kandaurova and A. É. Sviderskiĭ, Zh. Éksp. Teor. Fiz. **97**, 1218 (1990) [Sov. Phys. JETP **70**, 684 (1990)].
[4] V. A. Vasil'ev, Yu. M. Romanovskiĭ, and V. G. Yakhno, *Autowave Processes* [in Russian], Nauka, Moscow, 1987.
[5] G. S. Kandaurova, A. É. Sviderskiĭ, V. P. Klin, and V. I. Chani, Pis'ma Zh. Tekh. Fiz. **20**, 40 (1994) [Tech. Phys. Lett. **20**(16), 663 (1994)].
[6] G. S. Kandaurova, V. Kh. Osadchenko, A. A. Rusinov, and E. A. Rusinova, JETP Lett. **63**, 478 (1996).
[7] G. S. Kandaurova and V. Kh. Osadchenko, Pis'ma Zh. Tekh. Fiz. **20**, 24 (1994) [Tech. Phys. Lett. Tech. Phys. Lett. **20**(21), 864 (1994)].
[8] A. Malozemoff and J. Slonczewski, *Magnetic Domain Walls in Bubble Materials*, Academic Press, New York, 1979 [Russian translation, Mir, Moscow, 1982].
[9] A. B. Borisov and Yu. I. Yal'shev, Fiz. Met. Metalloved. **79**, 18 (1995).

Translated by M. E. Alferieff

Magnetization-odd nonreciprocal reflection of light from the magnetoelectric–ferromagnet $LiFe_5O_8$

V. N. Gridnev, B. B. Krichevtsov, V. V. Pavlov, and R. V. Pisarev
A. F. Ioffe Physicotechnical Institute, Russian Academy of Sciences, 194021
St. Petersburg, Russia

(Submitted 28 November 1996)
Pis'ma Zh. Éksp. Teor. Fiz. **65**, No. 1, 65–70 (10 January 1997)

Circular dichroism, which changes sign under magnetization reversal and exhibits a 120° periodicity, is observed in the reflection of light from the (111) plane of a noncentrosymmetric $LiFe_5O_8$ crystal in the transverse geometry $\mathbf{k}\perp\mathbf{M}$, where the linear Kerr effect is forbidden. It is shown that this phenomenon is due to the manifestation of optical magnetoelectric susceptibility and a Kerr effect of third order in the magnetization. The spectral dependences of the circular dichroism in the range 1.4–3.1 eV show that this phenomenon is of a resonance character. © *1997 American Institute of Physics.*
[S0021-3640(97)01201-2]

PACS numbers: 75.50.Cc, 75.80.+q, 78.20.Fm, 78.20.Jq, 75.60.Ej

It is well known that so-called nonreciprocal optical phenomena can exist in crystals in which invariance under time reversal is violated.[1] The nonreciprocal Faraday and Kerr effects, observed in the transmission and reflection of light, respectively, are well known.[2,3] These effects are widely used to study the electronic states and magnetic structures of magnets, semiconductors, superconductors, and metals. However, symmetry analysis shows[4–6] that the spectrum of possible nonreciprocal effects can be much wider and need not be limited to the Faraday and Kerr effects. For example, until recently it was assumed that a necessary condition for the appearance of nonreciprocal optical effects is the presence of spontaneous or external magnetic field induced magnetization **M**. But it is now known that this condition is sufficient but not necessary. Nonreciprocal effects in transmission and reflection of light are possible, for example, in crystals with a zero magnetic field and with noncentrosymmetric magnetic structure, as was recently shown in the antiferromagnetic crystal Cr_2O_3 (Refs. 6–8). The study of nonstandard nonreciprocal effects is of interest in connection with the fact that their magnitude and sign are determined by microscopic mechanisms which are fundamentally different from those of the standard magnetooptic effects.[4,5,8,9]

This letter reports a new phenomenon — nonreciprocal reflection of light From a noncentrosymmetric crystal with spontaneous magnetization **M** under normal incidence in the transverse geometry $\mathbf{k}\perp\mathbf{M}$, i.e., under conditions when the linear (in the magnetization) Kerr effect vanishes. We shall show that the observed effect is due to magnetoelectric (ME) susceptibility and is related with a Kerr effect of third order in the magnetization.

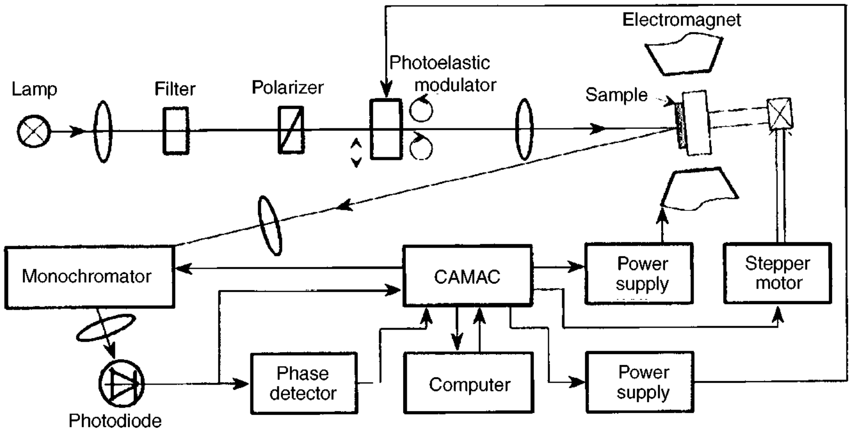

FIG. 1. Arrangement of the experimental apparatus for studying circular dichroism in reflection of light.

EXPERIMENT

The well-known lithium ferrite $LiFe_5O_8$ (Ref. 10), possessing a spinel structure, was chosen as the object of investigation. At temperatures $T>1020$ K its structure is described by the cubic group O_h^7 Below 1020 K, as the crystal cools slowly, the symmetry of the crystal decreases, as a result of ordering of an Li^+ ion and the three ions Fe^{3+} in the unit cell along directions of the (110) type, and is described by the noncentrosymmetric group O^6. At temperatures $T_C<943$ K lithium ferrite possesses ferrimagnetic ordering with easy axis in directions of the (111) type. The magnetic moments of the tetrahedral (A) and octahedral (B) Fe^{3+} sublattices are directed antiparallel as a result of the antiferromagnetic A–B interaction. The linear ME effect in $LiFe_5O_8$ was investigated in Ref. 11 by ferromagnetic resonance measurements. The magnetooptic Kerr effect in $LiFe_5O_8$ was studied in Refs. 12 and 13.

In the present work we investigated circular dichroism (CD), which changes sign under magnetization reversal of the crystal $+\mathbf{M}\rightarrow-\mathbf{M}$, in the transverse geometry $\mathbf{k}\perp\mathbf{M}$ with the light reflected from a (111)-type plane. The experimental arrangement is shown in Fig. 1. A light beam from a 300-W incandescent lamp pass through a condenser, a water filter, a polarizer, and a photoelastic modulator and was focused on the sample. The water filter served to prevent heating of the sample. The sample on the holder could be rotated with the aid of a stepper motor around a direction normal to the surface of the sample by an angle $\phi=0-360°$. The sample was located in the gap of an electromagnet, which produced in the plane of the sample a magnetic field of magnitude up to $H=\pm1$ T, which is much stronger than the magnetic anisotropy field $H_A=0.029$ T. The reflected beam was focused onto the slit of a monochromator. The light leaving the monochromator was focused on a silicon photodiode. The variable component of the preamplified electric signal from the photodiode was fed into a phase detector. The experimental data were processed with a computer and a CAMAC interface. The constant component of the signal from the photodetector was measured with an ADC. The amplitude and sign of the magnetic field, the magnitude of the half-wave voltage on the

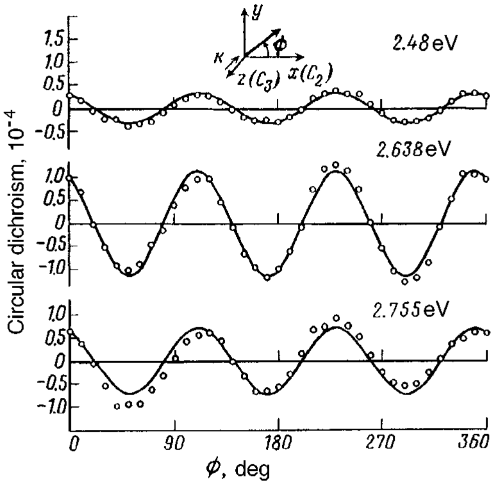

FIG. 2. Angular dependences of the circular dichroism upon rotation of the magnetization in a plane of the (111) type in $LiFe_5O_8$. $\phi=0$ corresponds to $\mathbf{M}\parallel C_2$. Dots — experimental data, solid curves — computational results. Inset: Geometry of the experiment.

modulator, the wavelength of the light, and the rotation angle of the crystal could be varied according to a special program. The magnitude of the circular dichroism was defined as the relative difference $(I^+ - I^-)/(I^+ + I^-)$ of the intensities of light with right-hand (I^+) and left-hand (I^-) circular polarizations reflected from the crystal. The measurements were performed at temperature $T=294$ K in the spectral range 1.4–3.1 eV. The angle between the wave vector **k** of the light and the normal to the surface of the sample did not exceed 10°. Its presence was due to the fact that it was necessary to separate the incident and reflected rays. The sensitivity of the CD measurements was equal to $\sim 10^{-5}$. The samples consisted of $5\times4\times1$ mm (111)-type plates oriented by the x-ray crystallographic method to within the accuracy $\sim 1°$ of the determination of the position of the axes.

RESULTS

The angular dependences of the CD of light reflected from the $LiFe_5O_8$ sample are displayed in Fig. 2. The sample was rotated around the [111] axis, which is oriented in a direction normal to the surface of the sample. The dependences are presented for three photon energies (2.48, 2.638, and 2.755 eV) and a magnetic field of 0.7 T. All angular dependences of the CD are identical and exhibit a 120° periodicity. The angle $\phi=0°$ corresponds to having the magnetic field **H** oriented parallel to the C_2 axis. Inaccuracy in the orientation of **H** relative to the plane of the sample could have resulted in the appearance of a polar Kerr effect, whose magnitude would not depend on the angle ϕ. This undesirable effect was eliminated by accurately orienting **H** parallel to the plane of the sample.

The spectral dependence of the CD, corresponding to the maximum in the angular dependence of this effect ($\phi=110°$), is displayed in Fig. 3. A weak maximum (2.4 eV)

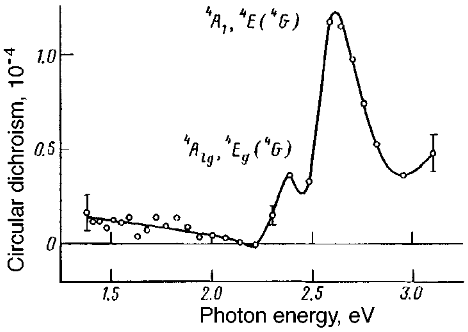

FIG. 3. Spectral dependence of the circular dichroism in reflection in $LiFe_5O_8$.

and a stronger and wider maximum are observed in the spectrum near 2.6 eV. Their position corresponds to electronic transitions observed in the spectral measurements of the Kerr effect in $LiFe_5O_8$.[13] However, it should be noted that in our work the CD was measured in a transverse magnetic field, while in Ref. 13 the rotation of the polarization plane of the reflected light in a longitudinal field was measured.

ANALYSIS

We shall analyze the experimental results on the basis of a phenomenological theory. Let the light propagate along the z axis, which is also the C_3 axis ([111]), of the laboratory coordinate system, and let the x axis coincide with the C_2 axis ([110]) (see inset in Fig. 2). Let us calculate the off-diagonal element r_{xy} of the matrix of reflection coefficients that is related with the ellipticity ε and the rotation θ of the polarization plane of the reflected light by the relation $\theta+i\varepsilon=r_{xy}/R_0$, where R_0 is the reflection coefficient neglecting the magnetization. We note that the CD in reflection is proportional to the ellipticity ε. Since in optics the ME effect is manifested only when allowance is made for the spatial dispersion of the permittivity tensor ϵ_{ij}, to analyze the reflection it is necessary to take account of the nonuniformity of the medium as a result of the presence of a boundary.[14] The material relations allowing for contributions which are odd under time reversal have the form[15]

$$D_i(\mathbf{r})=\left[\epsilon_{ik}^s+\epsilon_{ik}^a+\frac{1}{2}\,\frac{\partial(\gamma_{ikl}^s-\gamma_{ikl}^a)}{\partial r_l}\right]E_k+\gamma_{ikl}^s\frac{\partial E_k}{\partial r_l}, \tag{1}$$

where the indices s and a denote the symmetric and antisymmetric parts of the material tensors with respect to an interchange of the indices i and k. All terms in Eq. (1) except the first one describe nonreciprocal effects of interest to us. Specifically, the tensor ϵ_{ik}^a describes the magnetooptic Kerr effect and γ_{ikl} describes the linear spatial dispersion, which includes the ME contribution. Using the method proposed in Ref. 16 we obtain for r_{xy}

$$r_{xy}=\frac{2k}{n_0(n_0+1)^2}\left[\frac{\epsilon_{xy}^a}{k}+i\gamma_{xyz}^a\right], \tag{2}$$

where $k = \omega n_0 / c$.

An interesting feature of $LiFe_5O_8$ is that under normal incidence of light in the transverse geometry $\mathbf{k} \perp \mathbf{M}$ there are no terms in Eq. (2) which are linear in the magnetization. This fact is well known for the linear (in the magnetization) Kerr effect, and here we shall present a proof for the ME effect. As a result of the antisymmetry of γ^a_{xyz} with respect to x and y and on account of the duality relations, the most general expression for the components γ^a_{xyz} has the form $\gamma^a_{xyz} = e_{xyz} \beta_{zzk} M_k$, where $e_{xyz} = 1$ is a component of the completely antisymmetric tensor of rank 3 and β_{zzk} are the components of a material tensor of rank 3. However, in an O group the components $\beta_{zzk} = 0$. Therefore, in the case when light is incident in a direction normal to the sample, the nonreciprocal effects in reflection from a $LiFe_5O_8$ crystal magnetized in the (111) plane can be of cubic or higher odd order in the magnetization. Taking account of contributions in ϵ^a_{xy} which are cubic in $\mathbf{M}$ results in the fact that in both reflection and transmission of light odd (with respect to $\mathbf{M}$) nonreciprocal effects can be observed under normal incidence in the transverse geometry $\mathbf{k} \perp \mathbf{M}$. These effects are absent in cubic crystals, if light propagates along even two- and fourfold symmetry axes, but they can appear along any other directions, for example, along a threefold axis of the type (111). The contribution of terms which are third order in $\mathbf{M}$ to γ^a_{xyz} also leads to the appearance of nonreciprocal effects, and for an orientation of the crystal with the (111) axis perpendicular to the surface of the sample it will be manifested in the form of a 120° periodicity of the effects associated with both ϵ^a_{xy} and γ^a_{xyz}. Therefore it is very important in practice to have a criterion for distinguishing these contributions. We shall indicate a symmetry criterion based on different transformation properties of the tensors ϵ^a_{ik} and γ^a_{ikl}.

If $\mathbf{M} \| x$, then the component ϵ^a_{xy} can be written in the form $\epsilon^a_{xy} = \epsilon_{xyz} A_{zxxx} M^3_x$ where A_{zxxx} are the components of a tensor of rank 4. When the crystal is rotated by 180° around the x axis, $A_{zxxx} \rightarrow -A_{zxxx}$ and the component ϵ^a_{xy} changes sign. This means that there is no Kerr effect. If $\mathbf{M} \| y$, then the component ϵ^a_{xy} remains unchanged under a rotation by 180° around the x axis. Therefore the angular dependence of the Kerr effect which is of third order in $\mathbf{M}$ and the associated circular dichroism in reflection has the form $\mathrm{CD} = A \sin 3\phi$, where ϕ is the angle between the magnetization and the C_2 axis in the (111) plane. The component γ^a_{xyz} possesses an additional index z compared with ϵ^a_{xy} and for this reason the angular dependence of the circular dichroism associated with γ^a_{xyz} is described by the expression $\mathrm{CD} = B \cos 3\phi$, i.e., the effect is nonzero when $\mathbf{M} \| C_2$ and zero when $\mathbf{M} \perp C_2$.

The experimental dependences of the circular dichroism, which changes sign when the magnetization of the crystal is reversed, are described by a third-order harmonic $\sin(3\phi + \phi_0)$, where $\phi_0 = 10°$ (Fig. 2). Such angular dependences cannot be associated with a longitudinal Kerr effect because of the presence of a small angle between the incident and reflected beams, since this effect should not depend on the angle ϕ. Therefore the observed CD can be attributed only to a third-order Kerr effect and a ME contribution. Since the angle $\phi_0 \simeq 10^0$ and $A/B = \tan 10° \sim 0.2$, we can conclude that the ME contribution to the CD is much larger in the spectral range investigated.

The spectral dependence of CD in $LiFe_5O_8$ (Fig. 3) exhibits a pronounced resonance character and is characterized by the presence of two bands at the energies $E = 2.4$ eV and

$E=2.6$ eV belonging to transitions in Fe^{3+} ions in the octahedral and tetrahedral positions, respectively.[13] It is important to note, however, that the measured CD is proportional to the ellipticity ε of the reflected light, which in the case of the Kerr effect possesses near electronic transitions a dispersion-type spectral dependence.[2] At the same time, the CD spectrum due to the ME mechanism is characterized near electronic transitions by a resonance-type dependence,[8,9] as is also observed experimentally.

The main result of the present work is the observation of spontaneous nonreciprocal circular dichroism in a noncentrosymmetric cubic crystal. The unusual aspect of this phenomenon is that the nonreciprocity is observed under normal incidence in the transverse geometry $\mathbf{k}\perp\mathbf{M}$, i.e., when the linear magnetooptic Kerr effect vanishes. Symmetry analysis showed that the observed effect is determined by two different mechanisms, mostly by the optical ME susceptibility and partially by a Kerr effect which is of third order in the magnetization. The large magnitude of the effect in $LiFe_5O_8$ is due, in our opinion, to the fact that it is determined by the spontaneous magnetization and also by the resonance enhancement of the effect near electronic transitions. In principle, effects of this type should exist in noncentrosymmetric dia- and paramagnetic crystals in a magnetic field, but in this case the question of their magnitude can be solved only in further experiments.

We thank N. F. Kartenko for orienting the samples. This work was supported by the Russian Fund for Fundamental Research and the program ''Fundamental Spectroscopy.''

[1] L. D. Landau and E. M. Lifshitz, *Electrodynamics of Continuous Media*, Pergamon Press, N. Y., 1960, translation of the 1st Russian edition [Russian original, Nauka, Moscow, 1992, 3rd edition].

[2] J. F. Dillon Jr. in *Physics of Magnetic Garnets*, edited by A. Paoletti, North-Holland, Amsterdam, 1978, p. 379.

[3] J. Schoenes in *Materials Science and Technology*, edited by K. H. J. Buschow, VCH, Weinheim, 1992, Vol. 3A, p. 147.

[4] L. D. Baron, *Molecular Light Scattering and Optical Activity*, Cambridge University Press, Cambridge, 1982.

[5] E. B. Graham and R. E. Raab, Philos. Mag. B **64**, 267 (1991); *ibid.* **66**, 269 (1992).

[6] A. L. Shelankov and G. E. Pikus, Phys. Rev. B **46**, 3326 (1992).

[7] R. V. Pisarev, B. B. Krichevtsov, and V. V. Pavlov, Phase Transitions **37**, 63 (1991).

[8] B. B. Krichevtsov, V. V. Pavlov, R. V. Pisarev, and V. N. Gridnev, Phys. Rev. Lett. **76**, 4628 (1996).

[9] B. B. Krichevtsov, V. V. Pavlov, R. V. Pisarev, and V. N. Gridnev, Zh. Éksp. Teor. Fiz. **110**, 1505 (1996) [JETP **83**, 834 (1996)].

[10] Landholt-Boernstein, *Zahlenwerte und Funktionen, Magnetic Properties I*, Springer-Verlag, Berlin, 1962, Vol. 9.

[11] G. T. Rado, J. Magn. Magn. Mater. **15–18**, 542 (1980).

[12] A. V. Malikhovskiĭ, I. S. Édel'man, V. P. Gavrilin, and G. I. Barinov, Fiz. Tverd. Tela (Leningrad) **16**, 410 (1974) [Sov. Phys. Solid State **16**, 266 (1974)].

[13] S. Visnovsky and R. Krishnan, Appl. Phys. **18**, 243 (1979).

[14] V. M. Agranovich and V. L. Ginzburg, *Crystal Optics with Spatial Dispersion and Excitons*, Springer-Verlag, N. Y., 1984 [Russian original, Nauka, Moscow, 1979].

[15] V. V. Krichevtsov, V. V. Pavlov, R. V. Pisarev, and V. N. Gridnev, J. Phys., Condens. Matter. **5**, 8233 (1993).

[16] V. N. Gridnev, Phys. Rev. B **51**, 13079 (1995).

Translated by M. E. Alferieff

Q^2 dependence of the measured asymmetry A_1: a test of the Bjorken sum rule

A. V. Kotikov[a)] and D. V. Peshekhonov[b)]
Particle Physics Laboratory, Joint Institute for Nuclear Research, 141980 Dubna, Russia

(Submitted 11 September 1996; resubmitted 4 December 1996)
Pis'ma Zh. Éksp. Teor. Fiz. **65**, No. 1, 9–14 (10 January 1997)

We analyze the proton and deuteron data on the spin-dependent asymmetry $A_1(x,Q^2)$, supposing that the DIS structure functions $g_1(x,Q^2)$ and $F_3(x,Q^2)$ have a similar Q^2 dependence. As a result, we have found that $\Gamma_1^p - \Gamma_1^n = 0.190 \pm 0.038$ at $Q^2 = 10$ GeV^2 and $\Gamma_1^p - \Gamma_1^n = 0.165 \pm 0.026$ at $Q^2 = 3$ GeV^2; these values are in the best agreement with the Bjorken sum rule predictions. © *1997 American Institute of Physics.* [S0021-3640(97)00201-6]

PACS numbers: 11.55.Hx, 13.60.Hb, 13.88.+e

An experimental study of the nucleon spin structure is carried out by measuring the asymmetry $A_1(x,Q^2) = g_1(x,Q^2)/F_1(x,Q^2)$. The best known theoretical predictions for the spin-dependent structure function $g_1(x,Q^2)$ of the nucleon were made by Bjorken[1] and by Ellis and Jaffe[2] for the so-called first-moment value $\Gamma_1 = \int_0^1 g_1(x)dx$.

Calculation of the value of Γ_1 requires knowledge of the structure function g_1 at the same Q^2 over the entire range of x. Experimentally the asymmetry A_1 is measured at different values of Q^2 for different x bins. The accuracy of the past and modern experiments[3,4] permits one to analyze the data with the assumption[5] that the asymmetry $A_1(x,Q^2)$ is independent of Q^2 (i.e., that the structure functions g_1 and F_1 have the same Q^2 dependence). However, this assumption is not theoretically warranted (see discussions in Refs. 6–8); a different Q^2 dependence of the structure functions $g_1(x,Q^2)$ and $F_1(x,Q^2)$ is expected due to the difference in the polarized and unpolarized splitting functions (except for the leading order quark–quark one). Thus, in view of forthcoming more-precise data it is important to include the Q^2 dependence of the asymmetry.

This article is based on our observation that the Q^2 dependence of the spin-dependent and spin-averaged structure functions g_1 and F_3 is very similar over a wide range of $x: 10^{-2} < x < 1$. In the small-x region ($x < 10^{-2}$) it might not be true (see Refs. 6 and 9), but most of the existing data have been measured outside of that range.

Let us consider the nonsinglet (NS) Q^2 evolution of the structure functions F_1, g_1, and F_3. The DGLAP equation for the NS part of these functions can be written as[c)]:

$$\frac{dg_1^{NS}(x,Q^2)}{d\ \ln\ Q^2} = -\frac{1}{2}\gamma_{NS}^{-}(x,\alpha) \times g_1^{NS}(x,Q^2),$$

$$\frac{dF_1^{NS}(x,Q^2)}{d\ \ln\ Q^2} = -\frac{1}{2}\gamma_{NS}^{+}(x,\alpha)\times F_1^{NS}(x,Q^2), \tag{1}$$

$$\frac{dF_3(x,Q^2)}{d\ \ln\ Q^2} = -\frac{1}{2}\gamma_{NS}^{-}(x,\alpha)\times F_3(x,Q^2),$$

where the symbol × means the Mellin convolution. The splitting functions $\gamma_{NS}^{\pm}$ are the inverse Mellin transforms of the anomalous dimensions $\gamma_{NS}^{\pm}(n,\alpha)=\alpha\gamma^{(0)}(n)_{NS}+\alpha^2\gamma_{NS}^{\pm(1)}(n)+O(\alpha^3)$ and the Wilson coefficients[d)] $\alpha b^{\pm}(n)+O(\alpha^2)$:

$$\gamma_{NS}^{\pm}(x,\alpha)=\alpha\gamma_{NS}^{(0)}(x)+\alpha^2(\gamma_{NS}^{\pm(1)}(x)+2\beta_0 b^{\pm}(x))+O(\alpha^3), \tag{2}$$

where $\beta(\alpha)=-\alpha^2\beta_0-\alpha^3\beta_1+O(\alpha^4)$ is the QCD β function.

The above-mentioned Mellin transforms mean that

$$f(n,Q^2)=\int_0^1 dx x^{n-1} f(x,Q^2), \tag{3}$$

where $f=\{\gamma_{NS}^{(0)},\ \gamma_{NS}^{\pm(1)},\ b_{NS}^{\pm},\ \gamma_{ij}^{(k)},\ \gamma_{ij}^{*(k)},\ b_i$ and $b_i^*\}$ with $k=1,\ 2$ and $\{i,j\}=\{S,G\}$.

Equations (1) show that the Q^2 dependence of the NS parts of g_1 and F_3 is the same (at least in the first two orders of the perturbative QCD[10)]) and differs from F_1 already in the first subleading order ($\gamma_{NS}^{+(1)}\neq\gamma_{NS}^{-(1)}$ (Ref. 11) and $b_{NS}^{+}-b_{NS}^{-}=(8/3)x(1-x)$).

For the singlet parts of g_1 and F_1 the evolution equations are:

$$\frac{dg_1^S(x,Q^2)}{d\ \ln Q^2} = -\frac{1}{2}[\gamma_{SS}^{*}(x,\alpha)\times g_1^S(x,Q^2)+\gamma_{SG}^{*}(x,\alpha)\times\Delta G(x,Q^2)],$$

$$\frac{dF_1^S(x,Q^2)}{d\ \ln Q^2} = -\frac{1}{2}[\gamma_{SS}(x,\alpha)\times F_1^S(x,Q^2)+\gamma_{SG}(x,\alpha)\times G(x,Q^2)], \tag{4}$$

where

$$\gamma_{SS}(x,\alpha)=\alpha\gamma_{SS}^{(0)}(x)+\alpha^2(\gamma_{SS}^{(1)}(x)+b_G(x)\times\gamma_{GS}^{(0)}(x)+2\beta_0 b_S(x))+O(\alpha^3),$$

$$\begin{aligned}\gamma_{SG}(x,\alpha)=\frac{e}{f}[\alpha\gamma_{SG}^{(0)}(x)+\alpha^2(\gamma_{SG}^{(1)}(x)+b_G(x)\times(\gamma_{GG}^{(0)}(x)-\gamma_{SS}^{(0)}(x)+2\beta_0 b_G(x)\\ +b_S(x)\times\gamma_{SG}^{(0)}(x))]+O(\alpha^3)\end{aligned}$$

and $e=\Sigma_i^f e_i^2$ is the sum of the squares of the charges of f active quarks. The equations for the polarized anomalous dimensions $\gamma_{SS}^{*}(x,\alpha)$ and $\gamma_{SG}^{*}(x,\alpha)$ are similar. They can be obtained by making the replacements $\gamma_{SG}^{(0)}(x)\rightarrow\gamma_{SG}^{*(0)}(x)$, $\gamma_{Si}^{(1)}(x)\rightarrow\gamma_{Si}^{*(1)}(x)$, and $b_i(x)\rightarrow b_i^{*}(x)$ $(i=\{S,G\})$.

Note here that the gluon term in the case of F_1 is not negligible at $x<0.3$, but for g_1 we can neglect such terms at $x>0.01$ (Refs. 7 and 8). The value $b_s^{*}(x)(b_s(x))$ coincides with $b^{-}(x)(b^{+}(x))$. The difference between $\gamma_{NS}^{-(1)}$ and $\gamma_{SS}^{*(1)}+b_G^{*}(x)\times\gamma_{GS}^{(0)}(x)$ is negligible because it does not contain a power-law singularity at $x\rightarrow 0$ (i.e., a singularity at $n\rightarrow 1$ in momentum space). Moreover, it decreases as $O(1-x)$ at $x\rightarrow 1$

TABLE I. The first-moment values of g_1 of the proton and deuteron.

$x_{\min}-x_{\max}$	$\langle Q^2\rangle$	Target type	$\int_{x_{\min}}^{x_{\max}} g_1 dx$	Γ_1	Experiment
.003−0.7	10 GeV^2	proton	0.130	0.134±0.011	SMC
.003−0.7	10 GeV^2	deuteron	0.038	0.036±0.009	SMC
.029−0.8	3 GeV^2	proton	0.123	0.130±0.004	E143
.029−0.8	3 GeV^2	deuteron	0.043	0.044±0.003	E143

(Ref. 12). Contrary to this, the difference between $\gamma_{SS}^{(1)}+b_G(x)\times\gamma_{GS}^{(0)}(x)$ and $\gamma_{SS}^{*(1)}+b_G^*(x)\times\gamma_{GS}^{(0)}(x)$ contains a power-law singularity at $x\rightarrow 0$ (see, e.g., Ref. 10).

The analysis discussed above allows us to conclude that the function

$$A_1^*(x)=\frac{g_1(x,Q^2)}{F_3(x,Q^2)} \tag{5}$$

should be practically independent of Q^2 at $x>0.01$.

The right-hand sides of Eqs. (1) and (4) contain integrals of structure functions, and so Eq. (5) should hold approximately only in the case of similar x dependence of $g_1(x,Q^2)$ and $F_3(x,Q^2)$ at fixed Q^2. But such is indeed the case (see Ref. 13 at $Q^2=3\ \mathrm{GeV}^2$, for example).

The asymmetry A_1 at $Q^2=\langle Q^2\rangle$ can then be defined as

$$A_1(x_i,\langle Q^2\rangle)=\frac{F_3(x_i,\langle Q^2\rangle)}{F_3(x_i,Q_i^2)}\cdot\frac{F_1(x_i,Q_i^2)}{F_1(x_i,\langle Q^2\rangle)}\cdot A_1(x_i,Q_i^2), \tag{6}$$

where $x_i(Q_i^2)$ means an experimentally measured value of $x(Q^2)$.

We use the SMC and E143 proton and deuteron data on the asymmetry $A_1(x,Q^2)$.[3,4] To get $F_1(x,Q^2)$ we take the NMC parametrization of $F_2(x,Q^2)$ (Ref. 14) and the SLAC parametrization of $R(x,Q^2)$ (Ref. 15) ($F_1\equiv F_2/2x[1+R]$). To get the values of $F_3(x,Q^2)$ we parametrize the CCFR data[16] as a function of x and Q^2 (see the parametrization in the Appendix).

First, using Eq. (5), we recalculate the asymmetry measured by SMC[3] and E143[4] on the proton and deuteron targets at $Q^2=10\ \mathrm{GeV}^2$ (SMC) and $3\ \mathrm{GeV}^2$ (E143), which are the average values of Q^2 in these experiments, respectively. The values obtained for $\int g_1(x)dx$ through the measured x ranges are shown in Table I.

To get the values of the first moments $\Gamma_1^{p(d)}$ we estimate the unmeasured regions of SMC and E143, using their original formalism. Our estimates coincide with the original ones except for the results in the small-x region unmeasured by SMC. We obtain the following results for central values of $\Delta\Gamma^{p,d}=\int_0^{0.003}g_1(x)dx$ at $Q^2=10\ \mathrm{GeV}^2$: $\Delta\Gamma^p=0.003$ and $\Delta\Gamma^d=0.0022$, which are smaller then the corresponding SMC estimates: $\Delta\Gamma^p=0.004$ and $\Delta\Gamma^d=0.0028$. The errors coincide with those cited in Ref. 3. The E143 estimates for $\int_0^{0.029}g_1(x)dx$ do not change, since the Q^2-evolution of the asymmetry is negligible at $x\sim 0.03$. Results on the values of Γ_1 are also shown in Table I.

We would like to point out that the E143 and SMC formalisms may lead to underestimation of $g_1^{p,d}(x,Q^2)$ at small x and, hence, to underestimation of $\Delta\Gamma^{p,d}(Q^2)$ (see the careful analysis in the first of Refs. 8). Unfortunately, our procedure does not at work at $x \leqslant 0.01$, and we cannot check the SMC and E143 estimates for the unmeasured regions here. To clear up this situation it is necessary to include a careful small-x analysis in the discussion; that is a subject for our future long article.[17]

As the last step we calculate the difference which is predicted by the Bjorken sum rule, $\Gamma_1^p - \Gamma_1^n$:

$$\Gamma_1^p - \Gamma_1^n = 2\Gamma_1^p - 2\Gamma_1^d/(1-1.5\cdot\omega_D),$$

where $\omega_D = 0.05$[3,4] is the probability for the deutron to be in a D state.

At $Q^2 = 10$ GeV^2 we get the following results:

$$\Gamma_1^p - \Gamma_1^n = 0.190 \pm 0.038, \tag{7}$$

to be compared with the SMC published value

$$\Gamma_1^p - \Gamma_1^n = 0.199 \pm 0.038 \quad (\text{SMC}^3),$$

and the theoretical prediction

$$\Gamma_1^p - \Gamma_1^n = 0.187 \pm 0.003 \quad (\text{Theory}).$$

At $Q^2 = 3$ GeV^2 we get for the E143 data:

$$\Gamma_1^p - \Gamma_1^n = 0.165 \pm 0.026, \tag{8}$$

to be compared with

$$\Gamma_1^p - \Gamma_1^n = 0.163 \pm 0.026 \quad (\text{E143}^4),$$

$$\Gamma_1^p - \Gamma_1^n = 0.171 \pm 0.008 \quad (\text{Theory}).$$

Note that only the statistical errors are quoted here. To the accuracy considered they are equal to the errors cited in Refs. 3 and 4. The above-cited theoretical predictions for the Bjorken sum rule have been computed in Ref. 18 to the third order in the QCD parameter α_s.

In conclusion, we would like to note the following:

- The value of $\Gamma_1^p - \Gamma_1^n$ obtained in our analysis is in the best agreement with the Bjorken sum rule prediction.
- The values obtained here for Γ_1^p and Γ_1^n themselves are essentially unchanged. The improvement in relation to the Bjorken sum rule is the result of oppositely directed changes in the values of Γ_1^p and Γ_1^n when Eq. (5) is used.
- Our observation that the function $A_1^*(x)$ is independent of Q^2 at large and intermediate x is supported by the good agreement of the present analysis with other estimates[19,7,8] of the Q^2 dependence of A_1. A detailed analysis will be presented later in a separate long article.[17]

TABLE II. Values of the coefficients of CCFR data parametrization.

C_1	C_2	C_3	C_4	C_5
0.8064	1.6113	0.70921	−2.2852	1.8927
C_6	C_7	C_8	C_9	C_{10}
6.0810	4.5578	0.7464	−0.3006	3.9181
C_{11}	C_{12}	C_{13}	C_{14}	C_{15}
−0.1166	10.516	−5.7336	−37.114	3.7452

We are grateful to W. G. Seligman for providing us the available CCFR data of Ref. 16, to A. V. Efremov for discussions, and to an anonymous referee for critical comments which led to important improvements in this paper.

We are also grateful to G. Ridolfi for the opportunity to present a short version[20] of this letter at the Polarized Structure Function section of the Workshop DIS96.

This work is supported in part by the Russian Fund for Fundamental Research, Grant No. 95-02-04314-a.

APPENDIX

The parametrization used for the CCFR data[16] is:

$$xF_3(x,Q^2)=F_3^a\left(\frac{\log(Q^2/\Lambda^2)}{\log(Q_0^2/\Lambda^2)}\right)^{F_3^b},$$

where

$$F_3^a=x^{C_1}(1-x)^{C_2}(C_3+C_4(1-x)+C_5(1-x)^2+C_6(1-x)^3+C_7(1-x)^4)[C_8$$
$$+C_9x+C_{10}x^2+C_{11}x^3],\quad F_3^b=C_{12}+C_{13}x+\frac{C_{14}}{x+C_{15}},$$

$Q_0^2=10$ GeV^2, and $\Lambda=200$ MeV.

[a] e-mail: kotikov@sunse.jinr.dubna.su

[b] e-mail: peshehon@sunse.jinr.dubna.su

[c] We use $\alpha(Q^2)=\alpha_s(Q^2)/4\pi$.

[d] Because we are considering here the structure functions themselves, and not the parton distributions. Note that $b^+_{NS}(n)$ and $b^-_{NS}(n)$ have more-standard definitions as $b_{1,NS}(n)=b_{2,NS}(n)-b_{L,NS}(n)$ and $b_{3,NS}(n)$.

---

[1] J. D. Bjorken, Phys. Rev. **148**, 1467 (1966); Phys. Rev. D **1**, 1376 (1970).
[2] J. Ellis and R. L. Jaffe, Phys. Rev. D **9**, 1444 (1974); **10**, 1669 (1974).
[3] D. Adams, B. Adeva, E. Arik *et al.*, Phys. Lett. B **329**, 399 (1994); **357**, 248 (1995).
[4] K. Abe, T. Akadi, P. L. Anthony *et al.*, Phys. Rev. Lett. **74**, 346 (1995); **75**, 25 (1995).
[5] J. Ellis and M. Karliner, Phys. Lett. B **313**, 131 (1993); F. E. Close and R. G. Roberts, Phys. Lett. B **316**, 165 (1993).

[6] M. Anselmino, A. Efremov, and E. Leader, Phys. Rep. **261**, 1 (1995); J. Ellis and M. Karliner, Preprint CERN-TH.279/95 and TAUP-2297-95 (1995); B. L. Ioffe, ‘‘The nucleon spin structure’’, Proceedings of Quarks-94, Vladimir, p. 14.

[7] T. Gehrmann and W. J. Stirling, Z. Phys. C **65**, 470 (1995); M. Glück, E. Reya, and W. Vogelsang, Phys. Lett. B **359**, 210 (1995); A. V. Kotikov and D. V. Peshekhonov, Phys. Rev. D **54**, 3162 (1996).

[8] M. Glück, E. Reya, M. Stratmann and W. Vogelsang, Phys. Rev. D **53**, 4775 (1996); T. Gehrmann and W. J. Stirling, Phys. Rev. D. **53**, 6100 (1996).

[9] S. Forte, Preprint CERN-Th/95-305 (1995); R. D. Ball, Preprint Edinburg 95/558 (1995).

[10] J. Kodaira, S. Matsuda, T. Muta *et al.*, Phys. Rev. D **20**, 627 (1979); Nucl. Phys. B **159**, 99 (1979).

[11] D. A. Ross and C. T. Sachrajda, Nucl. Phys. B **149**, 497 (1979); G. Altarelli, Phys. Rep. **81**, 1 (1982).

[12] R. Merting and W. L. van Neerven, Z. Phys. C **70**, 625 (1996).

[13] C. Bourrely and J. Soffer, Nucl. Phys. B **445**, 341 (1995).

[14] M. Arneodo, A. Arvidson, B. Badelek *et al.*, Phys. Lett. B **364**, 107 (1995).

[15] L. W. Whitlow, S. Rock, A. Bodek *et al.*, Phys. Lett. B **250**, 193 (1990).

[16] P. Z. Quintas, W. C. Leung, S. R. Mishra *et al.*, Phys. Rev. Lett. **71**, 1307 (1993); M. H. Shaevitz, C. Arroyo, K. T. Bachmann *et al.*, Nucl. Phys. Proc. Suppl. B **38**, 188 (1995).

[17] A. V. Kotikov, A. P. Nagaitsev and D. V. Peshekhonov, work in progress.

[18] S. A. Larin and J. A. M. Vermaseren, Phys. Lett. B **259**, 345 (1991).

[19] G. Altarelli, P. Nason, and G. Ridolfi, Phys. Lett. B **320**, 152 (1994); K. Abe, T. Akadi, P. L. Anthony *et al.*, Phys. Lett. B **364**, 61 (1995); R. D. Ball, S. Forte, and G. Ridolfi, Nucl. Phys. B **444**, 287 (1995).

[20] A. V. Kotikov and D. V. Peshekhonov, hep-ph/9608369 and in the Proceedings of the Workshop DIS96 (in press).

Published in English in the original Russian journal. Edited by Steve Torstveit.

On the effect of van Hove singularities on the critical field of type-II superconductors

R. O. Zaĭtsev
Kurchatov Institute Russian Science Center, 123182 Moscow, Russia

(Submitted 3 October 1996; resubmitted 28 November 1996)
Pis'ma Zh. Éksp. Teor. Fiz. **65**, No. 1, 71–76 (10 January 1997)

The properties of the two-dimensional Hubbard model with strong repulsion are studied under the condition that the Fermi surface passes through van Hove singularities. The upper critical field is calculated under conditions where there is no relaxation. © *1997 American Institute of Physics.* [S0021-3640(97)01301-7]

PACS numbers: 74.60.Ec, 74.20.−z

Experiments show that the superconducting transition temperature T_c depends strongly on the position of the Fermi level inside the Brillouin zone. In the generalized Hubbard–Emery–Hirsch model, the vanishing and appearance of Cooper instability for certain values of the Fermi energy is explained by the possibility of a sign change of the amplitude of electron-electron scattering on the entire Fermi surface at once. In Refs. 1 and 2 I did not consider the problem of finding the transition temperature. Actually, the analysis was conducted at $T=0$, which reduced to discovering the Cooper instability for the critical electron or hole density corresponding to the condition of a sign change of the scattering amplitude.

This letter studies the case of intermediate densities, for which the scattering amplitude is negative. To find the maximum possible critical field, it is assumed that in this region the Fermi surface intersects the van Hove singularities. Computer calculations[3] for the Hubbard model with strong repulsion confirm this possibility.

Consider a two-dimensional electronic system with the spectrum

$$\xi_{\mathbf{p}}=-2|t|(\cos\alpha+\cos\beta)-\mu. \tag{1}$$

Here $2|t|$ is the doubled effective hopping integral, which in what follows is set equal to 1; α and β are dimensionless quasimomenta; and, μ is the chemical potential.

Assume first that there is no field and $T=0$. Then for a prescribed scattering amplitude g the equation for determining the energy gap Δ_0 has the form

$$2=\sum_{\mathbf{p}}\frac{g}{\sqrt{\Delta_0^2+\xi_{\mathbf{p}}^2}}. \tag{2}$$

For zero chemical potential μ this relation can be put into the form[4]

$$\pi=g\int_0^\infty\int_0^\infty\frac{d\epsilon dy\cos(\epsilon y)J_0^2(y)}{\sqrt{\Delta_0^2+\epsilon^2}}=g\int_0^\infty dyK_0(\Delta_0 y)J_0^2(y). \tag{3}$$

© 1997 American Institute of Physics

Here $J_0(y)$ and $K_0(y)$ are Bessel and modified Bessel (Macdonald) functions.

The final result determines the implicit dependence of the dimensionless energy gap $\overline{\Delta}_0 = \Delta_0/2|t|$ on the dimensionless constant $\Lambda = g/2\pi^2|t|$,

$$\Lambda^{-1} = 2q_\delta K^2(q_\delta), \tag{4}$$

where $q_\delta = 2/(\sqrt{4+\Delta_0^2}+\Delta_0)$ and $K(q)$ is a complete elliptic integral of the first kind.

In the asymptotic region $\Lambda \ll 1$ we have

$$\Delta_0 = 32|t|\exp(-\sqrt{2/\Lambda}). \tag{5}$$

To find the thermodynamic critical field we employ the general relation referring to the variation of the Ω potential:

$$\frac{\partial\Omega}{\partial g} = -\frac{\Delta^2}{g^2}. \tag{6}$$

Here Ω is the correction to the Ω potential referred to one cell.

Switching by means of the relation $\partial g/g^2 = \partial\Lambda/2\pi^2|t|\Lambda^2$ to variation with respect to $1/\Lambda$ and then integrating Eq. (6) in the variables Δ_0 with the aid of Eq. (5), we find an expression for the correction to the ground state energy that extends the BCS relation to the case of a logarithmically divergent density of states:

$$E_n - E_s = \Delta_0^2 \ln(32|t|\sqrt{e}/\Delta_0)/4\pi^2|t|. \tag{7}$$

Equating this expression to the magnetic-field energy per cell $H^2 v_0/8\pi$, we find the thermodynamic critical field H_{cm}

$$H_{cm} = \Delta_0 \sqrt{2\ln(32|t|\sqrt{e}/\Delta_0)}/a\sqrt{\pi|t|d}, \tag{8}$$

where d and a are the dimensions of the unit cell in directions parallel and transverse to the tetragonal axis of the experimental crystal.

Therefore we find that a logarithmic increase, proportional to $(2/\Lambda)^{1/4}$, of the thermodynamic critical field as compared with the BCS theory.

An even larger increase can be obtained for the so-called upper critical field, corresponding to the appearance of superconducting seed nucleus. To calculate the upper critical field H_{c2} it is sufficient to study an integral equation linearized with respect to the wave function $\Psi(\mathbf{r})$ of a Cooper pair:

$$\Psi(\mathbf{r}) = g\sum_{\mathbf{r}'} K(\mathbf{r},\mathbf{r}')\Psi(\mathbf{r}'). \tag{9}$$

Just as in Eq. (2), the quantity g equals minus the electron scattering amplitude calculated at the Fermi surface.

In a homogeneous space the kernel $K(\mathbf{r}-\mathbf{r}')$ is determined in terms of its Fourier components $K(\mathbf{s})$

$$K(\mathbf{s}) = T\sum_{\omega,\mathbf{p}} G_\omega(\mathbf{p}_+)G_{-\omega}(-\mathbf{p}_-), \tag{10}$$

where

$$G_\omega(\mathbf{p})=(i\omega-\xi_{\mathbf{p}})^{-1}, \quad \mathbf{p}_\pm=\mathbf{p}\pm\mathbf{s}/2. \tag{11}$$

The differential part of the Ginzburg–Landau equations is determined by the second term in the expansion of the kernel $K(\mathbf{s})$ in powers of $\mathbf{s}$.

The size of a Cooper pair decreases with temperature, so that the Ginzburg–Landau equation becomes inapplicable.[5] In the presence of an external field H, instead of these equations one must solve the integral equation (9) with the kernel (10) where the substitution $s_x\rightarrow s_x+eH\hat{y}$ is made. If an eigenfunction of the Ginzburg–Landau equation, $\Psi(\mathbf{r})=\exp(-|e|Hy^2)$, is used as a trial function, then it can be proved[6] that it is also an eigenfunction of the integral operator (10). Substituting this function and integrating over the angular variables yields the following solvability condition:

$$1=g\sum_{\mathbf{r}} K(0,\mathbf{r})\exp[-|e|H(x^2+y^2)/2c\hbar]. \tag{12}$$

Ultimately, after a Fourier transformation, we obtain the equation

$$2\pi|e|H=g\int_{-\infty}^{+\infty}K(\mathbf{s})\exp[-c\hbar(s_x^2+s_y^2)/2|e|H]ds_x ds_y, \tag{13}$$

where

$$K(\mathbf{s})=\sum_{\mathbf{p}} \frac{\tanh\dfrac{\xi_{\mathbf{p}_+}}{2T}+\tanh\dfrac{\xi_{-\mathbf{p}_-}}{2T}}{2(\xi_{\mathbf{p}_+}+\xi_{-\mathbf{p}_-})}. \tag{14}$$

It is convenient to use the kernel, obtained for the integral equation, at $T=0$. The explicit form of the kernel for the three-dimensional and isotropic case was obtained in Ref. 5. In the two-dimensional case it is natural to introduce two new variables to replace p_x and p_y: $2u=\xi_{\mathbf{p}_+}+\xi_{\mathbf{p}_-}$ and $2v=\xi_{\mathbf{p}_+}-\xi_{\mathbf{p}_-}$. The corresponding Jacobian of the transformation can be calculated for the two-dimensional isotropic case as well as near the van Hove singularities $A=(0, \pi)$ or $B=(\pi, 0)$, where the excitation spectrum is hyperbolic; $\xi_{\mathbf{p}}\approx p_x^2/2-\overline{p_y}^2/2$ or $\xi_{\mathbf{p}}\approx-\overline{p_x}^2/2+p_y^2/2$ $(\overline{p_{x,y}}=\pi+p_{x,y})$. Assuming also that the magnitude of each component of the total momentum $\mathbf{s}$ is small compared with the reciprocal of the size of a unit cell, we obtain the Jacobian in the form

$$Jk_{\mathbf{s}}^{(+)}=\frac{D(u,v)}{D(p_x,\overline{p_y})}, \quad Jk_{\mathbf{s}}^{(-)}=\frac{D(u,v)}{D(\overline{p_x},p_y)},$$

$$Jk_{\mathbf{s}}^{(\pm)}=\sqrt{R^2\mp 2Ru+v^2}, \quad R=a^2(s_x^2-s_y^2)/4. \tag{15}$$

The upper sign refers to the van Hove point A and the lower sign refers to the van Hove point B.

Let us consider first the case $T=0$. Then

$$K(\mathbf{s})=\sum_{\lambda=\pm}\int\int\frac{du\,dv\,\Theta(u^2-v^2)}{2\pi^2|u|Jk_{\mathbf{s}}^{(\lambda)}}=\int_0^1\frac{du}{2\pi^2 u}\ln\left[\frac{(1+2u)}{|1-2u|}\right]$$

$$+\int_1^{\bar{u}/|R|}\frac{du\,\ln(4u^2-1)}{2\pi^2 u}. \tag{16}$$

The quantity $\bar{u}$, determining the upper cutoff limit for the energy variable u, equals to logarithmic accuracy the corresponding energy quantity $\bar{\epsilon}$ arising in the calculation of the energy gap Δ_0. Comparing with the corresponding result (5) shows that in the dimensionless units $\bar{u}=8$, but this assertion must be checked with the aid of computer calculations.

The expression (16) must be substituted into the left-hand side of Eq. (12) and the resulting equation must be integrated with respect to the variables $s_x=\rho\cos\varphi$, $s_y=\rho\sin\varphi$, and $4R=a^2\rho^2\cos 2\varphi$. The integrals are calculated independently over φ and ρ. The final results are expressed in terms of a logarithmic function of $[\overline{uc}\hbar]/[|e|Ha^2]$ and also in terms of Euler's constant $C=\ln\gamma=0.5772\ldots$. As a result, we obtain a relation similar to Eq. (4):

$$2\Lambda^{-1}=\ln^2[4c\hbar\gamma\overline{u/a}^2|e|H]. \tag{17}$$

The dimensionless quantity $\bar{u}$ should appear in the definition of Δ_0, so that comparing with the asymptotic equation (4) makes it possible to express the upper critical field in terms of Δ_0:

$$H_{c2}(0)=c\hbar\gamma\Delta_0/a^2|te|. \tag{18}$$

This answer must be compared with the result for the spherical model:[5]

$$H_{c2}(0)=c\gamma e^2\Delta_0^2/8|e|\hbar v_F^2=\gamma c\hbar\Delta_0^2 d^{2/3}/32|e|t^2a^{8/3}(3\pi^2 n)^{2/3}, \tag{19}$$

where v_F is the Fermi velocity and n is the number of electrons per cell.

The critical field (19) for a spherical Fermi surface is of the same order of magnitude as the critical field for a two-dimensional cylindrical surface. However, the critical field (18) for the hyperbolic model is t/Δ_0 times greater than the critical field (19). It is also greater than the thermodynamic field (8). In order of magnitude $H_{c2}(0)/H_{cm}(0)\simeq(c\hbar/e^2)\sqrt{e^2d/ta^2}\Lambda^{1/4}$, so that if the BCS parameter Λ is not small compared to the fourth power of the fine-structure constant, then the system under study should be regarded as a type-II superconductor.

To find the temperature dependence of the upper critical field near the superconducting transition temperature, we represent the kernel of the integral equation as a sum over the discrete frequencies $\omega=T\pi(2n+1)$ and then expand in powers of the total momentum $\mathbf{s}$:

$$K(\mathbf{s})=T\sum_{\omega}W_{\omega}(\mathbf{s}). \tag{20}$$

For fixed $|\omega|$ the function $W_{\omega}(0)$ can be expressed in terms of a complete elliptic integral $K(k)$ with the parameter $k_{\omega}=2/\sqrt{4+\omega^2}$:

$$W_{\omega}(0)=\sum_{\mathbf{p}} G_{\omega}(\mathbf{p})G_{-\omega}(-\mathbf{p})=\frac{k_{\omega}K(k_{\omega})}{\pi|\omega|}. \tag{21}$$

The expression (21) summed over frequencies can be represented as an expansion in large logarithms of the inverse temperature:

$$K(0,T)\cong\frac{1}{2\pi^2}\ln^2\left(\frac{32|t|\gamma}{\pi T}\right). \tag{22}$$

Expanding the expression (22) in powers of the closeness to the superconducting transition temperature T_c, we find a linear law according to which the second critical field vanishes:

$$H_{c2}=\pi^2T_cL(T_c-T)/7\zeta(3)|e|a^2t^2, \tag{23}$$

where L is a large temperature logarithm evaluated at $T=T_c$: $L=\ln(32\gamma|t|/\pi T_c)=\sqrt{2/\Lambda}$. Hence it can be concluded that near the transition point the field H_{c2} is $\sqrt{L}$ times greater than the thermodynamic critical field. To fine the temperature slope of the critical field at low temperatures $T\ll T_c$ it is necessary to take account of the effect of the van Hove singularities, which is large in the frequency range $|\omega|\ll|\mathbf{s}|$.

In the case of zero chemical potential the contribution of the van Hove points can be distinguished by switching to the variables u and v, integrating with the aid of the Jacobian (15), and then employing for $T\ll|t(s_x^2-s_y^2)a^2|$ the asymptotic form of the kernel $K(\mathbf{s})$ at $T=0$ (see Eq. (16)):

$$K(\mathbf{s})=\frac{1}{2\pi^2}\ln^2\frac{\overline{u}}{r(\mathbf{s})},\quad r(\mathbf{s})=|s_x^2-s_y^2|a^2/4. \tag{24}$$

To further simplify the calculations, we employ the following interpolation description: For small $r(\mathbf{s})\ll T$ we employ the low-temperature expansion (22) and for large $r(\mathbf{s})\gg T$ we employ the approximation (24). More accurately, in integrating over the variable $r(\mathbf{s})$ a limiting value r^* is chosen such that above this value the kernel $K(\mathbf{s})$ is determined according to Eq. (24) while for smaller values of the argument the kernel depends only on the temperature in accordance with Eq. (22). We find the quantity r^* from the obvious condition that the expressions (22) and (24) be identical, so that for $r<r^*=\overline{u}\pi T/16\gamma$

$$K(r)=\frac{1}{2\pi^2}\ln^2\frac{\overline{u}}{r^*(T)},\quad \text{for } r>r^*,\quad K(\mathbf{s})=\frac{1}{2\pi^2}\ln^2\frac{\overline{u}}{r(\mathbf{s})}. \tag{25}$$

We choose instead of the variables $s_{x,y}$ the variables r and $z=a^2(s_x^2+s_y^2)$. As a result, the integral equation (13) acquires the form

$$1=8g\alpha\int_{r>0}drK(r)\int_{4r}^{\infty}\frac{dz\ \exp(-\alpha z)}{\pi\sqrt{z^2-16r^2}}.$$

Integrating over the variable z yields

$$\pi=8g\alpha\int_0^{r=r^*}K(r=r^*)K_0(4r\alpha)dr+8g\alpha\int_{r=r^*}^{\infty}K(r>r^*)K_0(4r\alpha)dr.$$

It is convenient to switch in the second integral to integration over infinite limits, so that an expansion of the modified Bessel function for small x, $K_0(x) \approx \ln(2/\gamma x)$, can be used in the remaining integrals.

The integration over infinite limits gives a temperature-independent leading term given by Eq. (17). The remaining integrals over the region $r < r^*$ are proportional to the first power of the temperature and contain a dependence on different logarithmic variables:

$$2\Lambda^{-1} = \ln^2(8\overline{u}\alpha\gamma) - \frac{2}{\pi}\int_0^{\tau}\left[\ln^2\left(\frac{4\alpha\overline{u}}{x}\right) - \ln^2\left(\frac{4\alpha\overline{u}}{\tau}\right)\right]\ln\left(\frac{2}{\gamma x}\right)dx.$$

Here $\alpha = 1/2|e|Ha^2$, $\tau = [\pi T\overline{u}\alpha/4\gamma]$, and $\overline{u} = 8$.

As a result of the integration, we find a double logarithmic correction proportional to the temperature:

$$2\Lambda^{-1} = \ln^2(8\overline{u}\alpha\gamma) - \frac{4T}{\gamma|e|Ha^2}\ln\left(\frac{8e^2}{\overline{u}\pi T\alpha}\right)\ln\left(\frac{16\gamma e}{\pi T}\right), \tag{26}$$

where $\overline{u} = 8$, and the doubled hopping integral $2|t|$, to which the temperature is scaled, can be eliminated from the right-hand side with the aid of the definition of the energy gap (5). The third equation, which makes it possible to eliminate the dimensionless BCS constant, is Eq. (17), which determines the maximum possible critical field H_0:

$$2\Lambda^{-1} = \ln^2(4\overline{u}\gamma c\hbar/|e|H_0a^2) = \ln^2(32|t|/\Delta_0). \tag{27}$$

As a result, both the left- and right-hand sides of Eq. (26) can be expressed only in terms of measurable quantities H_0, Δ_0, H, and a^2:

$$2\Lambda^{-1} = \ln^2\left(\frac{4\overline{u}\gamma c\hbar}{|e|H_0a^2}\right) = \ln^2\left(\frac{4\overline{u}\gamma c\hbar}{|e|Ha^2}\right) - \frac{2T}{\gamma^2\Delta_0}\ln\left(\frac{4e^2\Delta_0}{\pi T}\right)\ln\left(\frac{4\gamma\overline{u}\Delta_0 e}{\pi T H_0|e|a^2}\right). \tag{28}$$

The logarithmic growth of the temperature derivative is partially compensated by the large logarithm L, which, according to Eq. (27), can be expressed in terms of the maximum critical field H_0: $L = \ln(32\gamma c\hbar/a^2|e|H_0)$, and

$$-\left.\frac{\partial H}{\partial T}\right|_0 \approx \frac{H_0}{\gamma^2\Delta_0}\ln\left(\frac{4\gamma e\Delta_0}{\pi T}\right)\left[1 + L^{-1}\ln\left(\frac{\Delta_0 e}{\pi T}\right)\right]. \tag{29}$$

The temperature derivative of the expression (25) in the limit $T \to T_c$ can be expressed similarly:

$$-\left.\frac{\partial H}{\partial T}\right|_{T_c} = \left(\frac{32LH_0\gamma}{7\zeta(3)T_c}\right)e^{-L}. \tag{30}$$

Therefore, for $T \leqslant T_c$ the large temperature logarithm is completely compensated by the small ratio between the superconducting transition temperature and the magnitude of the hopping integral, which, according to Eq. (30), gives exponential smallness in logarithmic variables.

As the temperature decreases, the absolute magnitude of the temperature derivative increases. According to Eq. (29), at low temperature this changes into a logarithmic temperature increase. Therefore the entire curve $H_{c2}(T)$ has negative curvature. The double logarithmic growth can be observed only at extremely low temperatures, where $T/T_c \ll |e|H_0 a^2/c\hbar \cong 2\cdot 10^{-5}\ \mathrm{kOe}^{-1} H_0$.

The small slope (30) for $T \leqslant T_c$ corresponds to an ordinary pure superconductor[5] with a Fermi energy of the order of the hopping integral $|t|$ and an effective mass of the order of $\hbar^2/a^2|t|$.

This work was performed as part of the State Program on high-T_c superconductivity ''Ékstend II'' 94011.

[1] R. O. Zaĭtsev, Phys. Lett. A **134**, 199 (1988).
[2] R. O. Zaĭtsev, JETP Lett. **55**, 135 (1992).
[3] E. Dagotto, A. Moreo, D. J. Scalapino *et al.*, Phys. Rev. Lett. **67**, 1918 (1991).
[4] A. P. Prudnikov, Yu. A. Brychkov, and O. I. Marichev, *Integrals, Series, and Special Functions* [in Russian], Nauka, Moscow, 1983.
[5] L. P. Gor'kov, Zh. Éksp. Teor. Fiz. **37**, 833 (1960) [Sov. Phys. JETP **10**, 593 (1960)].
[6] E. Helfand and N. R. Werthamer, Phys. Rev. Lett. **147**, 686 (1964).
[7] A. P. Mackenzie, S. R. Jullian, G. G. Lonzarich *et al.*, Phys. Rev. Lett. **71**, 1238 (1993).
[8] M. Osofsci, R. J. Soulen, S. A. Wolf *et al.*, Phys. Rev. Lett. **71**, 2315 (1993).

Translated by M. E. Alferieff

Investigation of the magnetic structure of holmium by the muonic method

I. A. Krivosheev, A. A. Nezhivoĭ, B. A. Nikol'skiĭ, and A. N. Ponomarev
Kurchatov Institute Russian Science Center, 123182 Moscow, Russia

V. N. Duginov, V. G. Ol'shevskiĭ, and V. Yu. Pomyakushin
Joint Institute of Nuclear Research, 141980 Dubna, Moscow District, Russia

(Submitted 28 November 1996)
Pis'ma Zh. Éksp. Teor. Fiz. **65**, No. 1, 77–80 (10 January 1997)

The possibility of investigating by the muonic method spin-incommensurate helicoidal structures of rare-earth magnets is examined for the example of holmium. It is shown that at temperatures 20 K $< T <$ 130 K only one precession frequency of the muon spin is observed in holmium; this is characteristic for a simple helicoidal structure. The broadening of the frequency spectrum increases sharply at temperatures $T \leqslant 20$ K, possibly as a result of the appearance of spin-slip structure at these temperatures. The Fermi contact magnetic field of the conduction electrons of holmium at a muon is measured.

© *1997 American Institute of Physics.* [S0021-3640(97)01401-1]

PACS numbers: 75.30.−m, 76.75.+i, 75.50.Ee

The magnetic structure of holmium has been investigated by the method of neutron diffraction[1–3] and later with the aid of synchrotron radiation.[4,5] It has been shown that the magnetically ordered state of holmium is observed at $T < T_N$, where $T_N = 132$ K is the Néel temperature. For $T_C < T < T_N$ the magnetic structure of holmium is an antiferromagnetic helicoid, which at $T_C = 20$ K restructures into a ferromagnetic helicoid. The axis of the helicoid is directed along the hexagonal c axis of the crystal perpendicular to the basal plane of the base. The atomic magnetic moments in the antiferromagnetic state of holmium lie in the basal planes. Their directions in each separate plane are parallel to one another and make with the neighboring plane an angle α, which increases continuously from $\alpha \sim 30°$ at $T = 20$ K up to $\alpha \sim 50°$ at $T = 130$ K. In the ferromagnetic state of holmium a small component of the atomic magnetic moments appears along the hexagonal axis of the crystal, and for $T < T_C$ the angle α remains approximately constant: $\alpha \sim 30°$.

The above-described magnetic helicoid of holmium is a spiral structure whose wavelength along the c axis and the distance between the basal planes of the crystal lattice are, generally speaking, incommensurate. A phenomenological description of such an incommensurate helicoid is the model of a magnetic spin-slip structure,[4–7] according to which only six equivalent directions of magnetic moments in the basal plane, which correspond to its hexagonal symmetry, are possible. According to the spin-slip model, an individual angle α_{ind} between the directions of magnetization of two neighboring basal planes of the helicoid can assume only two values: $\alpha_{\text{ind}} = 0$ and $\alpha_{\text{ind}} = 60°$. For $\alpha_{\text{ind}} = 0$

TABLE I. Schematic representation of the magnetic spin-slip structures of holmium.

T, K	α, deg	Symbol	Diagram
< 20	30	1	
40	36	2•	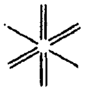
70	40	1•	
96	45	1••	

pairs (doublets) of two identically polarized basal planes form; two neighboring doublets are turned with respect to one another by an angle $\alpha_{\text{ind}} = 60°$ with one another. The sequence of doublets alternates with single planes (singlets), whose polarization makes an angle $\alpha_{\text{ind}} = 60°$ with the direction of polarization of the neighboring planes. The formation of such a singlet plane is termed spin-slip. According to the spin-slip model, the above-indicated angles α measured by the diffraction method are the average values of the individual angles α_{ind} between the doublet and singlet planes of a given magnetic structure. The conventional designations shown in Table I have been adopted to describe the spin-slip structure. The temperature and the corresponding angle α are presented in the first and second columns of the table. The third column gives the conventional symbols of the magnetic spin-slip structure; here the number indicates the number of

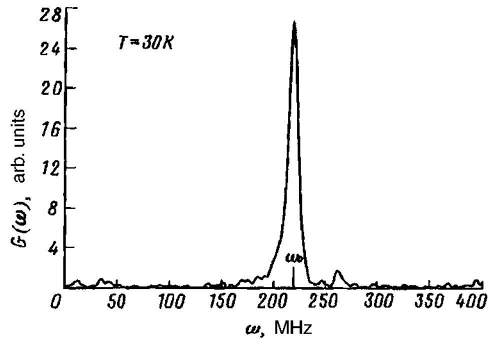

FIG. 1. Frequency spectrum $G(\omega)$ of precessing muons in holmium in a zero external magnetic field at $T = 30$ K; ω_0 is the value of ω in the single-frequency description of muon spin precession.

doublets and the dot indicates the number of singlets in successively repeating element of the spiral structure with average angle α. The fourth column gives the arrangements of the presented magnetic structures in projection on the basal plane; here the double lines denote doublets and single lines denote singlets.

In the present work the incommensurate magnetic structure of holmium is investigated for the first time by the muonic (μSR) method. This method is used to measure the internal magnetic fields B_μ at interstitial sites of the crystal lattice, where a muon is localized. In a simple helicoidal structure, i.e., with $\alpha_{\mathrm{ind}}=\alpha$, all interstitial sites are magnetically equivalent, and in a μSR experiment only one muon spin precession frequency is observed at a given temperature. In the spin-slip structure, the interstitial fields in different sections of the helicoid are different and the frequency spectrum of the muonic signal is found to be more complicated. For example, according to Table I, for $\alpha=36°$ the magnetic structure $2\cdot$ contains three magnetically nonequivalent interstitial sites: between a singlet and doublet, between two parallel-polarized planes of the same doublet, and between two doublets.

The experimental holmium sample consisted of a textured crystal with a distinguished direction of the hexagonal c axis and with approximately 0.01% impurities. During the measurements the c axis of the crystal was oriented parallel to the polarization of the muon beam. The sample was placed in a special cryostat whose temperature was set to within $\Delta T<0.2$ K. All measurements were performed in a zero external magnetic field. The experiment was performed in the muon channel of the GPD at the Paul Scherrer Institute (Villingen, Switzerland).

Figure 1 displays the frequency spectrum $G(\omega)$ of the oscillating part of the muon spin relaxation function at $T=30$ K. One can see from Fig. 1 that the spectrum $G(\omega)$ is

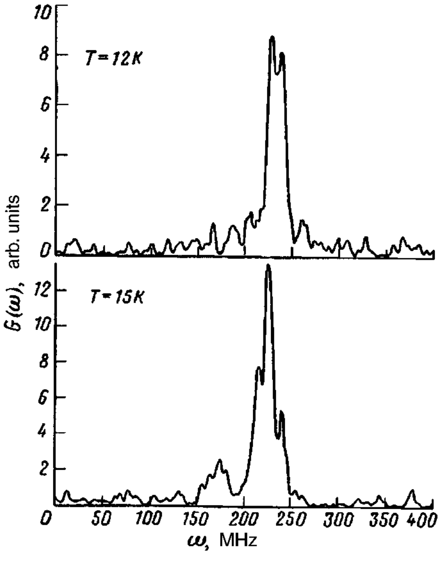

FIG. 2. Frequency spectra $G(\omega)$ holmium at temperatures 12 and 15 K.

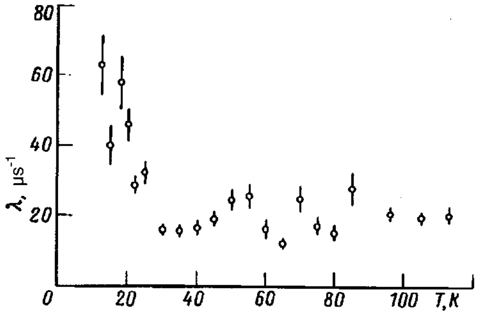

FIG. 3. Temperature dependence $\lambda(T)$ of the muon spin relaxation rate in holmium.

described by a single muon spin precession frequency $\omega_0 = \gamma B_\mu$ corresponding to the magnetic field B_μ at the interstitial site where the muon is localized. Here $\gamma = 13.55 \cdot 10^3$ Hz/G is the gyromagnetic ratio of the muon. Similar spectra $G(\omega)$ are observed at temperatures $T > 30$ K in the magnetically ordered state of holmium. At low temperatures $T < 20$ K the spectra $G(\omega)$ remain single-frequency, but they are more broadened, as shown in Fig. 2. The temperature dependence of the degree of broadening of the spectra $G(\omega)$ is illustrated in Fig. 3, which displays the relaxation rate $\lambda(T)$ of the amplitude of single-frequency muon spin precession in holmium.

The spectra $G(\omega)$ measured in holmium in the present experiment characterize the magnetic structure of this metal as a simple spiral with $\alpha_{\text{ind}} = \alpha$. At the same time, the broadening of the spectra $G(\omega)$, shown in Figs. 2 and 3, at $T < 20$ K could be due to several experimentally overlapping frequencies characteristic for the spin-slip structure observed at these temperatures in diffraction experiments.[5,6] The temperature dependence $B_\mu(T) = \gamma^{-1}\omega_0(T)$ of the magnetic field at a muon in holmium is shown in Fig. 4, which also displays the computed temperature dependences of the dipole magnetic fields B_{tet} and B_{oct} in the tetragonal and octahedral interstitial sites, respectively, of the crystal

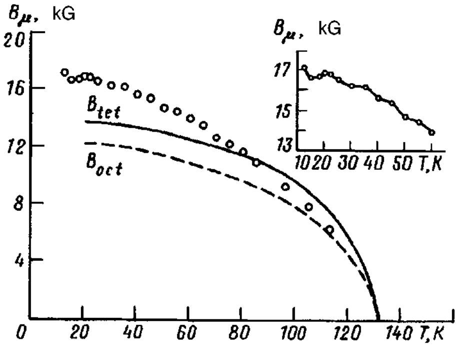

FIG. 4. Temperature dependence $B_\mu(T)$ of the magnetic field at a muon. $B_{\text{tet}}(T)$ and $B_{\text{oct}}(T)$ are the computed temperature dependences of the dipole magnetic fields in tetrahedral and octahedral interstitial sites of the crystal for the antiferromagnetic state of holmium at temperatures 20 K $< T <$ 132 K.

lattice of holmium for the case of a simple magnetic spiral, i.e., for $\alpha_{\mathrm{ind}}=\alpha$ in the antiferromagnetic state ($T>20$ K). The calculation of the dipole magnetic fields took account of the temperature dependences of the wavelength of the helicoid,[5] the crystal lattice parameters, and the magnetic moment of a holmium ion in the crystal.[3] One can see from Fig. 4 that the experimentally measured fields B_{μ} differ from dipole magnetic fields. This difference is due to the Fermi contact magnetic field of polarized conduction electrons at a muon $B_c=8/3\pi\mu_B\rho(0)P_e$. Here μ_B is the Bohr magneton; $\rho(0)$ is the density of the electronic wave function at the muon; and, P_e is the polarization of the conduction electrons.

We thank W. Zimmerman for assisting in the measurements. This work was supported by the Russian Fund for Fundamental Research (Grant 96-02-16999a).

[1] W. C. Koehler, J. W. Cable, H. R. Child *et al.*, Phys. Rev. **151**, 414 (1966); *ibid.* **158**, 450 (1967).
[2] G. P. Felcher, G. H. Lander, T. Arai *et al.*, Phys. Rev. B **13**, 3034 (1976).
[3] M. J. Pechan and C. Stassis, J. Appl. Phys. **55**, 1900 (1984).
[4] D. Gibbs, D. E. Moncton, K. L. D'Amico *et al.*, Phys. Rev. Lett. **55**, 234 (1985).
[5] J. Bohr, D. Gibbs, D. E. Moncton, and K. L. D'Amico, Physica A **140**, 349 (1986).
[6] R. A. Cowley and S. Bates, J. Phys. C: Solid State Phys. **21**, 4113 (1988).
[7] S. Bates, C. Patterson, G. J. McIntire *et al.*, J. Phys. C: Solid State Phys. **21,** 4125 (1988).

Translated by M. E. Alferieff

Mobile line in the acceptor photoluminescence spectrum of ‘‘pure’’ GaAs

K. S. Zhuravlev[a] and A. M. Gilinskiĭ
Institute of Semiconductor Physics, Siberian Branch of the Russian Academy, of Sciences, 630090 Novosibirsk, Russia

(Submitted 3 December 1996)
Pis'ma Zh. Éksp. Teor. Fiz. **65**, No. 1, 81–85 (10 January 1997)

A new line is observed in the photoluminescence spectra of epitaxial layers of undoped GaAs. The line is recorded in the region of the band–acceptor transitions with a delay relative to the excitation pulse, and with time after the excitation pulse it shifts substantially (by up to 15–18 meV) in the long-wavelength direction. The characteristics of the line attest to the possibility that small, highly doped, local regions with extended density-of-states tails can form in undoped GaAs. © *1997 American Institute of Physics.* [S0021-3640(97)01501-6]

PACS numbers: 78.66.Fd, 78.60.Ya

Low-temperature photoluminescence (PL) spectroscopy is widely used to check the impurity and defect composition of gallium arsenide and similar III–V compounds. It is well known that excitonic transition lines and lines corresponding to transitions to levels of shallow acceptors, chemical or bound with point defects in the material, are observed in the PL edge spectra of GaAs at low temperatures.[1,2] In contrast to this, the present letter reports the observation of an unusual ‘‘mobile’’ line in the low temperature PL spectra of undoped epitaxial gallium arsenide. The energy position of this line changes substantially as the excitation intensity changes or with time after the excitation pulse (up to 15–18 meV within 50–100 μs). The line lies in the region of transitions involving the participation of shallow acceptors, it dominates the delayed nonstationary PL spectra, and it is not associated with recombination via shallow impurities. The observed energy characteristics of the line and its behavior with time after excitation attest to the possibility of the formation of small local regions, possessing a high level of doping and extended density-of-states tails, in undoped GaAs.

Samples of nominally doped *n*- and *p*-GaAs with residual shallow impurity densities N_A and N_D in the range 10^{14}–10^{16} cm^{-3} and different degree of compensation were investigated. The samples were prepared by liquid-phase epitaxy (LPE) and molecular-beam epitaxy (MBE) in different growth regimes. The samples were grown on substrates consisting of undoped or chromium-doped semi-insulating (100) GaAs; the epitaxial layers ranged in thickness from 1 to 7 μm for the samples obtained by MBE and from 10 to 25 μm for the samples obtained by LPE. The lines were observed against the background of impurity luminescence by a measurement method in which the evolution of the nonstationary PL spectrum was recorded with a delay of tens of microseconds after pulsed excitation. As shown in Ref. 3, the decrease observed in the energy width of the lines in the delayed spectra makes it much easier to distinguish the components and

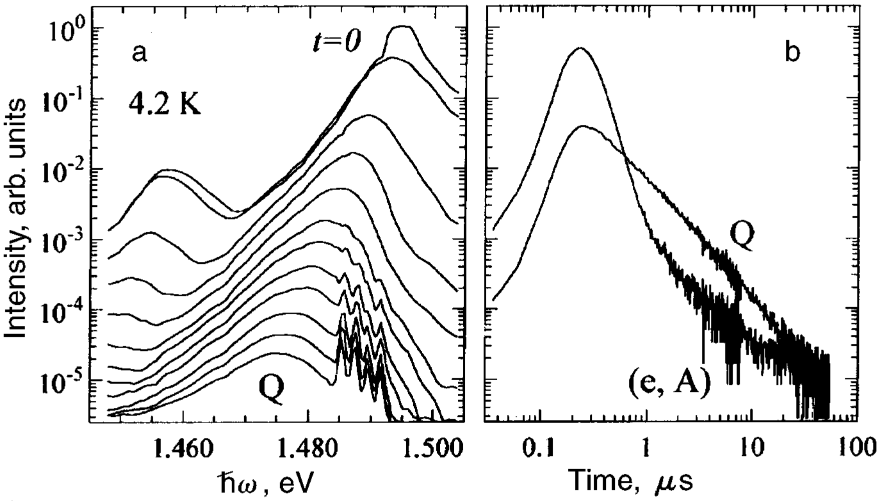

FIG. 1. Evolution of the PL spectra as a function of the delay time (a) and decay curves of nonstationary PL (b) of a sample demonstrating a mobile Q line at temperature $T=4.2$ K. The spectra in (a) were recorded at times of 0, 0.1, 0.3, 0.6, 1, 2, 3.5, 6, 9, 18, 30, and 50 μs after the excitation pulse (top to bottom). The decay curves (b) correspond to $\hbar\omega=1.4915$ eV ((e, A) line) and $\hbar\omega=1.483$ eV (Q line).

permits identification of transitions in multicomponent impurity PL spectra of GaAs. Nonstationary photoluminescence was excited by YAG:Nd laser pulses ($\lambda_{\mathrm{exc}}=532$ nm, pulse duration $\tau=120$ ns) or Al_2O_3:Ti laser pulses ($\lambda_{\mathrm{exc}}=760$ nm, $\tau=30$ ns); the power density in an excitation pulse was equal to 0.5–5 kW/cm^2. Ar$^+$ and He–Ne lasers were used to excite the stationary PL. The PL was recorded with a spectrometer based on a double diffraction monochromator and a photomultiplier operating in the photon counting mode with time resolution.

The PL spectra and decay curves of a sample demonstrating an unusual PL line at temperature $T=4.2$ K are displayed in Fig. 1. The data presented were obtained on a p-type sample, with a high degree of purity, grown by the LPE method from bismuth melt[4] and possessing, according to Hall measurements, $N_A-N_D=6\cdot10^{14}$ cm^{-3}. A wide line, associated with band–acceptor transitions, with a maximum near 1.493 eV and its phonon repetition are present in the spectrum during the action of the pump pulse. As the excitation relaxes, both lines shift with time in the long-wavelength direction. After 3.5 μs a fine structure appears in the spectrum, and 5 μs after the excitation pulse four narrow lines are distinguished in the spectrum. Thereafter the energy positions of the two short-wavelength lines do not change ($\hbar\omega=1.4913$ and 1.4890 eV), while the other two lines shift with time in the long-wavelength direction by ≈ 1 meV. This behavior attests to the fact that the first two lines are due to band–acceptor (e, A) transitions and the second pair of lines correspond to donor–acceptor transitions (D, A) with the participation of magnesium (or beryllium) and zinc acceptors. A wide structureless line, designated as Q and moving to $\hbar\omega=1.473$ eV at a time 50 μs after excitation, appears in the spectrum simultaneously with transitions on shallow donors. The shape of this line is substantially different from that of the lines associated with shallow impurities, and

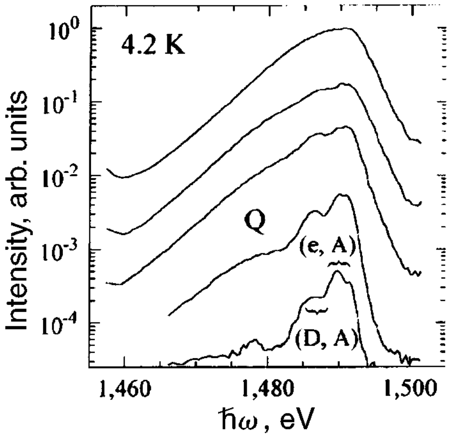

FIG. 2. PL spectra with stationary excitation with power density (top to bottom) of 20, 3, 0.4, $6\cdot10^{-2}$, and $6\cdot10^{-3}$ W/cm^2; $T=4.2$ K.

consists of an asymmetric bell with exponential wings of the form $I(\hbar\omega)\sim\exp(-|\hbar\omega-\hbar\omega_m|/\Delta)$, where $\hbar\omega_m$ is the position of the line maximum. The line width at half-height increases with the delay time up to 13 meV, and the slope indicator Δ increases to ≈ 15 and 5 meV on the long- and short-wavelength wings, respectively; this attests to the absence of quasiequilibrium in the system of carriers participating in the recombination.[2] The integral intensity of the Q line in the delayed spectra is 10–20 times higher than the intensity of the (e, A) and (D, A) lines. The Q line decays with time according to a power law close to $I(t)\sim t^{-1.5}$, and the (e, A) and (D, A) transitions decay according to the law $I(t)\sim t^{-1}$ (Fig. 1b).

Under stationary excitation the Q line is weak. For comparison, the stationary PL spectra for the same sample are displayed in Fig. 2. Irrespective of the excitation intensity, the (e, A) and (D, A) transitions dominate in the spectra, while the Q line is present in the form of a long-wavelength shoulder and is clearly distinguished only in the case of low excitation intensities, when it shifts strongly in the long-wavelength direction. As the excitation intensity increases, a superlinear increase in the intensity of the Q line is observed. The dependence of the position of its maximum on the excitation intensity I is described by a function of the form $\hbar\omega_m(I)=\hbar\omega_0+g\cdot\ln(I/I_0)$, where g is a parameter characterizing the displacement of the line accompanying a change in the pump intensity. This same dependence describes the displacement of the line with time in the nonstationary PL spectra, where I is the line intensity. The values of the parameter g for stationary and nonstationary PL spectra agree well with one another, and for the experimental samples they equal $g=1.5$–2.5 meV.

The above-described features of the decay kinetics and the spectra remain unchanged as the measurement temperature T increases up to 10–12 K. As T increases further, a temperature quenching of the (e, A), (D, A), and Q lines is observed together with an acceleration of the decay of the nonstationary PL. Surprisingly, however, increasing the temperature from 4.2 to 8 K results in a large increase in the intensity of transi-

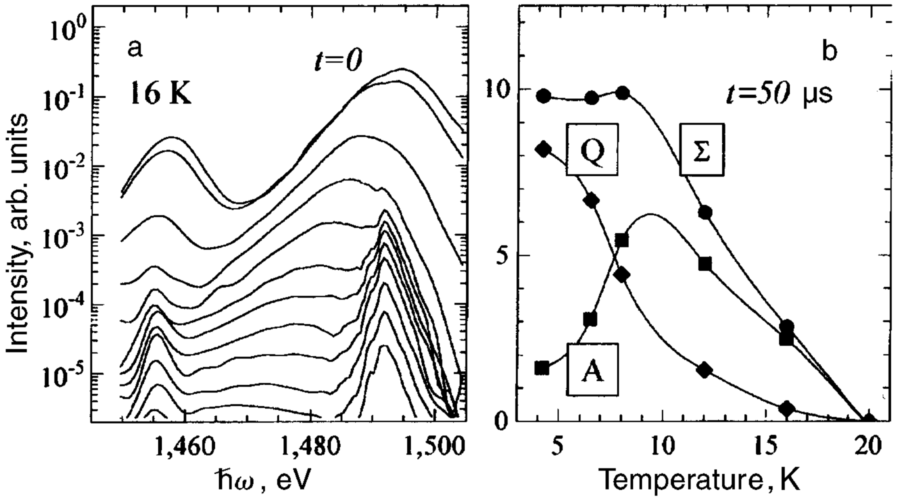

FIG. 3. a) Evolution of the PL spectra as a function of the delay time at temperature $T=16$ K. The spectra were recorded at times of 0, 0.1, 0.3, 0.6, 1, 2, 3.5, 6, 9, 18, 30, and 50 μs after the excitation pulse (top to bottom). b) Temperature dependence of the integral intensity of transitions A on shallow acceptors and the mobile Q line and the total intensity Σ in the spectrum 50 μs after the excitation pulse.

tions on shallow acceptors, accompanied by a drop of equal magnitude in the intensity of the Q line in the delayed spectra (Fig. 3). It is known that in the case of uniform doping of a material no increase with temperature is observed in the intensity of acceptor transitions.[1] The redistribution of the line intensities shows that in the process of trapping of nonequilibrium carriers the centers which are due to the appearance of the Q line compete with shallow impurities and, therefore, are located at a distance from the latter equal to less than the diffusion length. Hence it also follows that the potential well in which the carriers are captured is of the order of 1 meV deep, and in view of the substantially lower effective mass the formation of a shallow well is more likely for electrons than holes.

We observed the Q line in the spectra of a number of layers prepared by LPE and MBE, and we did not observe any correlation between the presence of a line and the density of residual impurities or the degree of compensation of the layers. Measurement of the charge carrier density profiles by the C–V method likewise did not reveal any macroscopic nonuniformities characteristic of these samples. The prolonged nonexponential decay of the Q line attests to the spatially indirect character of the carrier recombination. The energy position, line shape, and modification of the line shape with time as well as the superlinear dependence of the line intensity on the pump intensity show that the line Q is due to transitions between the density-of-states tails in strongly doped material.[2] Similar dependences were observed in samples of strongly compensated GaAs and solid solutions of III–V compounds,[5–7] on account of the formation of density-of-states tails with a depth of tens and hundreds of millielectron-volts. However, an estimate of the depth of the density-of-states tails according to the electrophysical parameters of the layers gives a value of not greater than several millielectron volts, which makes it impossible to explain the large width and shift of the Q lines by recombination in the density-of-states tails of uniform material. The transfer of line intensities in the spectrum as the temperature changes (Fig. 3) suggests that the appearance of the Q line is due to the existence of local regions in the epitaxial film which have a high doping level and deep density-of-states tails and which serve as effective sinks for nonequilibrium charge carriers but, because of their small volume, have very little effect on the electrophysical parameters of the samples. We conjecture that such locally nonuniform regions can form as a result of the penetration of impurities or defects from the substrates into the epitaxial layers.

We thank N. A. Yakusheva, N. S. Rudaya, Yu. B. Bolkhovityanov, D. I. Lubyshev, N. T. Moshegov, and A. I. Toropov for providing the GaAs samples and V. A. Samoĭlov for performing the C–V measurements. This work was supported by the Russian Fund for Fundamental Research (Grant 95-02-04755-a).

[a] e-mail: L37@ispht.nsk.su

---

[1] E. W. Williams, H. Barry Bebb *et al.*, *Semiconductors and Semimetals*, Academic Press, New York, 1972, p. 321.
[2] A. P. Levanyuk and V. V. Osipov, Usp. Fiz. Nauk **133**, 427 (1981) [Sov. Phys. Usp. **24**, 187 (1981)].
[3] A. M. Gilinsky and K. S. Zhuravlev, Appl. Phys. Lett. **68**, 373 (1996).
[4] N. S. Rudaya, Yu. B. Bolkhovityanov, K. S. Zhuravlev *et al.*, Pis'ma Zh. Tekh. Fiz. **16**(9), 37 (1990) [Tech. Phys. Lett. **16**, 337 (1990)].
[5] D. Redfield, J. P. Wittke, and J. I. Pankove, Phys. Rev. B **2**, 1830 (1972).
[6] M. C. DeLong, P. C. Taylor, and J. M. Olson, Appl. Phys. Lett. **57**, 620 (1990).
[7] P. W. Yu, C. E. Stutz, M. O. Manasreh *et al.*, J. Appl. Phys. **76**, 504 (1994).

Translated by M. E. Alferieff

Local surface segregations of implanted aluminum in an iron crystal with a low density of defects

V. I. Lavrent'ev and A. D. Pogrebnyak
Sumy Institute of Surface Modification, 244030 Sumy, Ukraine[a)]

R. Sandrik
Oxford University, Nuclear Physics, Oxford OX 3RH, UK

(Submitted 3 December 1996)
Pis'ma Zh. Éksp. Teor. Fiz. **65**, No. 1, 86–89 (10 January 1997)

The surface distribution of elements is studied by scanning a 3-MeV proton beam along the surface of a bcc-Fe sample implanted with aluminum ions in the dose interval $(1-50)\cdot 10^{16}$ cm^{-2}. Ring-shaped regions, up to 30 μm in diameter, with a high density of aluminum, which appear at implantation doses $(5-20)\cdot 10^{16}$ cm^{-2}, are observed. These regions appear as a result of radiation-stimulated segregation processes. A mechanism based on the existence of a low density of dislocations in the initial crystal is proposed to explain the implanted impurity segregation processes. © *1997 American Institute of Physics.* [S0021-3640(97)01601-0]

PACS numbers: 64.75.+g, 61.72.−y

1. One of the most consequential processes induced by intense charged-particle beams (electrons, ions) on the surface of a solid is radiation-stimulated segregation (RSS) — the spatial separation of the constituent components of the subsurface layers. The discovery of this phenomenon in the mid-1970s stimulated a series of theoretical and experimental works on the investigation of its nature.[1,2] It is now known that RSS is caused by the appearance of fluxes of radiation-induced nonequilibrium point defects toward sinks (clusters, dislocations, grain boundaries, free surface). In previous works the study of RSS in alloys was based on the assumption of a one-dimensional composition gradient, when fluxes of defects from the volume of the irradiated sample produce a layer of a new phase near the surface.[3,4] The RSS phenomenon has been analyzed quantitatively by means of depth profiling with the aid of methods such as Rutherford backscattering (RBS) and Auger electron spectroscopy (AES). We know of no works reporting the observation of RSS processes in two other mutually perpendicular directions (in a plane parallel to the surface of the sample).

The present letter reports experimental results on the observation of local surface segregations of an impurity in polycrystalline bcc-Fe samples as a result of implantation of high-energy aluminum ions. Such experiments are especially important for understanding correctly phase-formation processes in implanted layers as well as for the development of a theory of RSS.

2. Ten-keV Al ions were implanted in polycrystalline bcc-Fe samples in the Impul's-4 accelerator (SIMP, Ukraine) with the following parameters: pulse duration

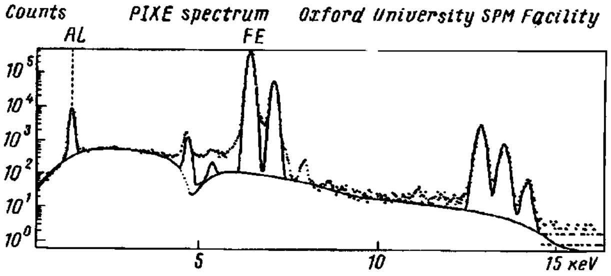

FIG. 1. PIXE energy spectrum for points on the surface of a bcc-Fe sample implanted with Al ions (dose $5\cdot 10^{16}$ cm^{-2}).

$\tau = 20$ μs, pulse repetition rate $f = 50$ s^{-1}, ion current density 0.5–5 mA/cm^2, and vacuum 10^{-4} Pa. The implantation dose was varied in the range $(1-50)\cdot 10^{16}$ cm^{-2}. The accelerating voltage U_a, the ion current density j_i, the repetition rate f, and the sample temperature T_s were controlled during the implantation process.

Samples of bcc-Fe, annealed at 950 °C for 2 h, with initial grain sizes of 1–2 mm were prepared for implantation. The initial dislocation density did not exceed 10^7 cm^{-2}, and the total impurity content was less than 0.01 wt.%. The observation of local surface segregations of the impurity was made possible by the use of a microbeam of protons which were obtained from a megaelectron-volt accelerator (Oxford University).

A quantitative analysis of the distribution of elements in different microregions of the surface of the implanted samples was performed with the aid of color maps of regions ranging in size from 10×10 μm up to 500×500 μm, obtained by RBS and PIXE (proton induced x-ray emission) as a result of scanning of a 3-MeV proton microbeam with a beam diameter of approximately 1 μm. The beam current was equal to 100 pA. Quantitative analysis of the elemental composition from certain points and regions on the surface was performed with the aid of RBS and PIXE energy spectra.

3. Our experiments showed that the character of the surface distribution of the elements along the surface of the Fe samples after Al implantation depends on the implantation dose. For example, at doses of $(1\text{–}5)\cdot 10^{16}$ cm^{-2} aluminum is distributed uniformly over the surface of the sample with an average concentration of 7–12 at.%. The PIXE spectrum obtained after Al implantation with a dose of $5\cdot 10^{16}$ cm^{-2} is displayed in Fig. 1. Besides peaks corresponding to aluminum and iron, a carbon peak is clearly seen in this spectrum (near 13 keV). Carbon penetrates into the subsurface layers of the sample from residual vapors in the vacuum chamber of the accelerator under the action of the high-energy Al ions.

Increasing the implantation dose to $2\cdot 10^{17}$ cm^{-2} results in the formation of characteristic surface nonuniformities in the Al distribution. While the Fe and C distributions are comparatively uniform, ring-shaped formations with a high Al concentration with the outer radius of the ring equal to approximately 10 μm are observed. The up to 5 μm in diameter interior region of these ring-shaped formations is characterized by a low ($\sim$10 at.%) Al concentration. The maximum Al concentration (up to 64 at.%) is observed

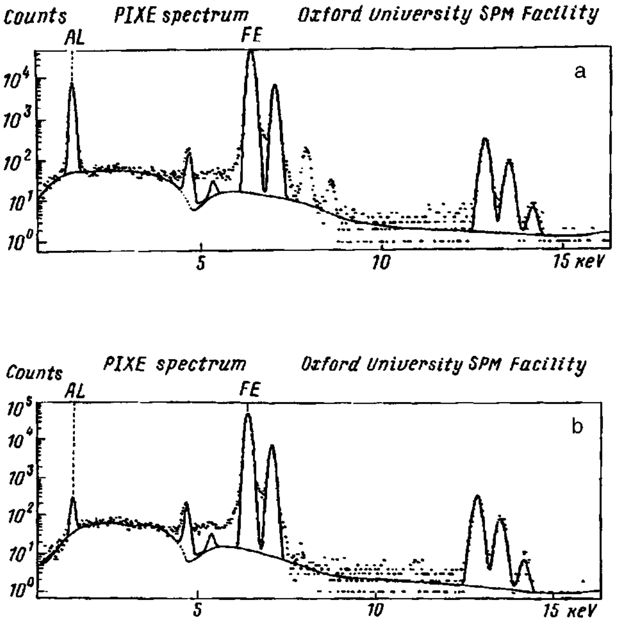

FIG. 2. PIXE energy spectra obtained for a bcc-Fe sample implanted with Al ions (dose $2\cdot 10^{17}$ cm^{-2}) for points in the central part of the ring zone (a) and at the center of the interior region of the ring zone (b).

near the central radius of the ring. The PIXE energy spectra corresponding to two different points of the ring-shaped region (in the central part of the ring and at the center of the interior region) are displayed in Figs. 2a,b. Increasing the implantation dose to $5\cdot 10^{17}$ cm^{-2} causes the ring-shaped Al regions to vanish, and a uniform distribution of elements along the surface of the sample, with a surface Al concentration of up to 28 at.%, is observed once again.

4. The observed surface redistribution of the implanted impurity attests to the occurrence local RSS processes during ion implantation. The distances between neighboring ring-shaped regions suggest that the Al segregation processes are due to dislocations present in the sample before implantation. As a result of elastic interaction, nonequilibrium vacancies precipitate on the dislocations, which results in the formation of a helicoid.[5,6] As a result of the nonuniform depth distribution of point defects arising in the sample during ion implantation,[7] the radii of the helicoid turns will also be different. As the helicoid continues to wind during the ion implantation process, it emits an independent dislocation loop as a result of the interaction of neighboring turns of maximum radius. Absorbing nonequilibrium vacancies, the dislocation loop expands. Implanted Al atoms in bcc-Fe are predominantly bound with radiation vacancies into stable defect complexes[1] which diffuse toward dislocations by means of additional vacancies and precipitate on them. As Al atoms ‘‘are collected,’’ the rate of expansion of the dislocation loop slows down. The head loop is supported by the subsequent dislocation loops with Al atoms distributed on them, thereby increasing the impurity concentration in the ring region.

The absence of observed Al precipitates with implantation doses less than $5\cdot 10^{16}$ cm^{-2} is due in this case to the fact that the density of nonequilibrium vacancies is too low to actuate emission of dislocation loops by the helicoid. At doses above $2\cdot 10^{17}$ cm^{-2} the ring-shaped impurity zones dissolve as a result of the development of thermally activated diffusion under high-temperature (523 K and higher) conditions.[8]

5. The proposed model makes it possible to estimate the parameters characterizing the segregation process. We take as a basis an expression determining the dependence of the radius l of a growing dislocation loop on the time t:[6]

$$l^2=\frac{2\mu b^3 D}{kT}t, \tag{1}$$

where μ is the shear modulus, b is the Burgers vector, and D is the diffusion coefficient of the defects governing the growth of the loop. For the values $\mu=8.4\cdot 10^{11}$ dynes/cm^2 and $b\sim 10^{-8}$ cm characteristic for bcc-Fe[9] and $l\approx 10^{-3}$ cm, $t\approx 300$ s, and $T\approx 400$ K from experiment, we obtain $D\approx 1.1\cdot 10^{-17}$ cm^2/s, which gives for the activation energy $H_m=1.35$ eV. The value obtained for H_m is almost identical to the migration energy of vacancies in bcc-Fe (1.32 eV[10]); this confirms the vacancy mechanism for the growth of the dislocation loops collecting Al impurity atoms.

In summary, in this letter the application of the proton microbeam method for local study of radiation-stimulated segregation processes was demonstrated and it was shown that dislocations play a role in the formation of microregions of the segregating impurity.

We thank Professor J.-P. Hirvonen (VTT, Finland) for a discussion of the results. This work is supported in part by the Ukrainian State Committee on Science and Technology (Projects 7.5.4/73-93 and 07.02.02/035-92).

[a]e-mail: SIMP@demex.sumy.ua

---

[1] F. V. Nolfi Jr. [Ed.], *Phase Transformations During Irradiation*, Applied Science Publishers, New York, 1983.
[2] J. R. Holland, L. K. Mansur, and D. I. Poffer [Eds.], *Phase Stability During Irradiation*, Metallurgical Society of AIME, New York, 1981.
[3] L. E. Rehn, P. R. Okamoto, and R. S. Averback, Phys. Rev. B **30**, 3073 (1984).
[4] N. Q. Lam, T. Nguyen, G. K. Leaf, and S. Yip, Nucl. Instrum. Methods B **31**, 415 (1988).
[5] L. D. Landau and E. M. Lifshitz, *Theory of Elasticity*, Pergamon Press, New York, 1986, 3rd English edition [Russian original, Nauka, Moscow, 1987].
[6] J. Friedel, *Dislocations*, Pergamon Press, N. Y., 1964 [Russian translation, Mir, Moscow, 1967].
[7] M. F. Denanot, O. Popoola, and P. Moine, Mater. Sci. Eng. A **115**, 145 (1989).
[8] M. Kiritani, H. Takata, K. Morijama, and F. E. Fujita, Phys. Mag. A **40**, 779 (1979).
[9] K. P. Yakovlev, *Concise Physicotechnical Handbook* [in Russian], Fizmatgiz, Moscow, 1960.
[10] R. W. Baluffi, J. Nucl. Mater. **69/70**, 240 (1978).

Translated by M. E. Alferieff

Charge mobility anisotropy in hcp ^{4}He crystals

O. A. Andreeva, K. O. Keshishev, and D. I. Kholin

P. L. Kapitsa Institute of Physics Problems, Russian Academy of Sciences, 117334 Moscow, Russia

(Submitted 9 December 1996)
Pis'ma Zh. Éksp. Teor. Fiz. **65**, No. 1, 90–95 (10 January 1997)

A strong anisotropy of the positive-charge mobility is observed in hcp ^{4}He crystals. The mobility activation energies in the principal directions are determined. © *1997 American Institute of Physics.* [S0021-3640(97)01701-5]

PACS numbers: 67.80.−s

Charge carriers in crystalline helium possess a specific intrinsic structure and are a unique test object for investigating the properties of quantum crystals. As in the case of liquid helium, it is assumed that in the crystal a negatively charged complex is an electron localized in a cavity[1,2] and a positive complex is a helium ion located at the center of a region compacted by electrostriction forces.[3] A theoretical estimate of the sizes of complexes of both signs gives values of the order of several interatomic distances. This means that the properties of a charge complex depend strongly on its configuration, which is dictated by the symmetry of the crystal lattice and by the effective size of the complex as a defect formed in a crystal as a result of the presence of a charge. By the properties of charges we mean the characteristic features of their motion in a crystal under the influence of an applied electric field.

According to Ref. 4, the symmetry of a charge complex should be manifested primarily as a dependence of the characteristic features of its motion on the direction of an applied electric field relative to the crystallographic axes of the crystal.

Up to now, all measurements of the velocity of charges in helium crystals have been performed on randomly oriented samples. The most complete review of works in this field up to 1985 has been given by Dahm.[5] As a result of many experiments, it has been established that the temperature dependence of the mobility of charges of both signs attests to an activation mechanism of their motion, and the closeness of the vacancy activation energies and mobilities of positive charges and ^{3}He impurities serves as an important argument in support of a common mechanism for the motion of impurity particles as a result of the motion of vacancies. In a quantum approach to this problem[6], the motion of the charges or impurity atoms is regarded as being the result of inelastic scattering of delocalized vacancies by them. The temperature and field dependences of the drift velocity of the charges contains in this case the parameters of the energy spectrum of the vacancies, such as the activation energy and width of the energy band.

Therefore an experimental investigation of the motion of charges as a function of the magnitude and direction of an electric field as well as the temperature should yield

© 1997 American Institute of Physics

information about the structure of the charge complexes and about the properties of vacancy excitations in helium crystals.

Direct measurements of the drift velocity of charges as a function of the electric field intensity as well as the pressure and temperature were performed by one of us with the aid of a three-electrode time-of-flight method.[7] Later, Golov, Efimov, and Mezhov-Deglin[8] discovered, while determining the drift velocity of charges according to the current setting time in a diode, that the temperature and field intensity dependences of the velocity of positive charges are nonmonotonic.

The characteristic features of charge motion which were presented in Refs. 7 and 8 found an explanation in the quantum symmetry approach to charge motion, developed by Andreev and Savishchev.[4] In the same work, a method was proposed, on the basis of an assertion about the relation between the symmetry of a charge complex and the anisotropy of its motion in crystals, for reconstructing the structure of a charge complex according to the angular dependences of its velocity. This approach requires experimental data on the anisotropy of charge motion. Direct measurements of the anisotropy of charge motion in helium crystals were not performed. Indirect indications of the presence of a sizable anisotropy were noted in Ref. 9. It is obvious that an experimental solution of this problem requires the ability to set in a controllable manner the direction of the electric field relative to the crystallographic axes of the crystal.

This letter reports the first results of a direct measurement of the anisotropy of charge motion in hcp ^{4}He crystals. The results were obtained on an experimental apparatus that makes it possible to change in a controllable manner the orientation of the crystal relative to the electric field and to measure the velocity of charges with the aid of a three-electrode time-of-flight method.

In this work, an optical cryostat equipped with a ^{3}He refrigerator was used. The helium crystals were grown in a metal chamber 25 mm long and with an inner diameter of 19 mm. Optical windows were mounted at the ends of the chamber with the aid of an indium gasket. Arranged horizontally, the symmetry axis of the crystal is also the optical axis of the cryostat. The chamber itself is mounted in a mechanism that makes it possible to rotate the chamber around an axis by an angle of $\pm 60°$ relative to the main position. This construction was used previously for studying the anisotropy of the properties of an interphase boundary in helium[10] and was described in detail in our preceding paper.[11]

The drift velocity of induced charges of both signs was determined with the aid of a three-electrode time-of-flight method based on measurement of the rise time of the collector current in a triode accompanying the passage of the charge front over the drift gap. The details of the triode construction and the characteristic features of the method have been discussed in Ref. 7. In the present case, a plane-parallel triode with the following parameters was employed: The electrode diameter (β^--active tritium source, grid, and collector) was equal to 8 mm, the grid–collector drift distance was 0.26 mm, and the source–grid (gate) interval was 0.10 mm.

The triode is mounted on a hinged suspension inside the chamber. The center of gravity of the triode is displaced so that the angle of inclination of the electrodes relative to the horizontal direction equals 47°. The axis of the hinge is parallel to the rotation axis

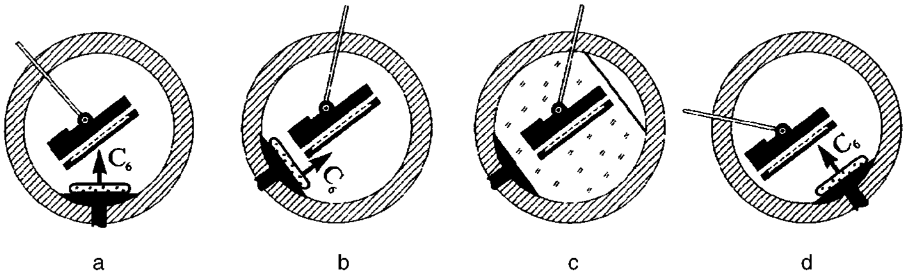

FIG. 1. Diagram illustrating the process used to grow oriented samples.

of the chamber so that the triode maintains its orientation in space, under the action of its own weight, as the chamber rotates.

A sample, oriented in the required manner relative to the electrodes of the measuring system, was grown at a temperature of ~ 1 K (i.e., below the temperature of the first faceting phase transition) in the following sequence. First, a sample whose C_6 axis is vertical to a high degree of accuracy (the deviation does not exceed 10^{-2} rad) is grown with the aid of the well-known ''dropping of a seed crystal'' method.[12] In the process, the crystal fills the bottom part of the chamber without touching the triode (Fig. 1a). Next, the chamber is turned together with the sample so that the visually monitored basal plane of the crystal makes the required angle with the electrode plane. The angles lying in a plane perpendicular to the optical axis are measured to within $3 \cdot 10^{-3}$ rad with a telescopic goniometer. In this position, the chamber together with the triode is overgrown with the solid phase (Fig. 1b,c).

To change the orientation of the sample relative to the measuring system the crystal is melted to dimensions for which the triode is freed from the solid phase. The chamber rotates into a new position and is once again overgrown with the crystal (Fig. 1d). This method makes it possible to obtain samples whose C_6 axis makes a prescribed angle with the direction of the electric field in the measuring triode.

The measurements were performed on the melting curve at temperatures not exceeding 1.1 K. Therefore the molar volume of the crystal remained constant, to a high degree of accuracy, and equal to 20.98 cm^3/mole. The most complete experimental data were obtained for positive charges. The field dependences of the velocities of the charges in the two principal crystallographic directions — parallel and perpendicular to C_6 at temperature $T = 1.00$ K — are displayed in Fig. 2. It should be noted that in the case of the perpendicular direction the orientation of the electric field relative to the C_2 axis in the basal plane remained random. The fact that the curves $v_{\perp}^{+}(E)$ obtained for different crystals are the same attests to the negligibly small anisotropy in this plane, which exhibits a sixfold symmetry. As one can see from Fig. 2a and the inset in Fig. 2b, in fields $E \leqslant 2 \cdot 10^4$ V/cm the velocity of the positive charges in both directions is proportional to the field strength: $v \sim \mu E$, where μ is the charge mobility in a given direction. The mobilities of the positive charges in the two principal directions (straight lines in Fig. 2) are:

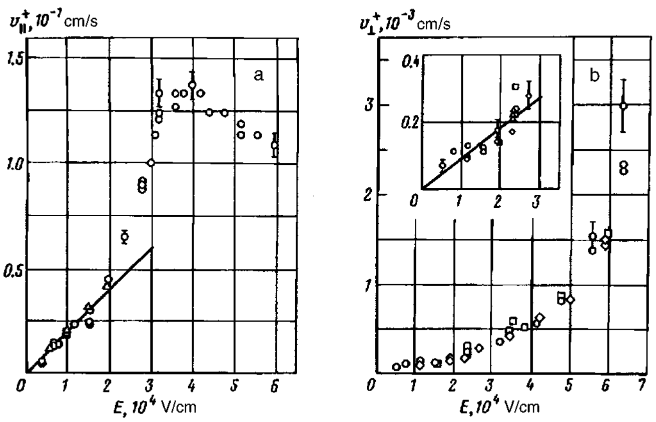

FIG. 2. Velocities of positive charges versus the field strength in the two principal directions: a — Parallel to the C_6 axis, b — perpendicular to the C_6 axis. $T=1.0$ K. The different symbols represent data obtained on different samples.

$$\mu_\parallel^+ = 2\cdot 10^{-6}\ \mathrm{cm^2/V\cdot s}\text{—in a direction parallel to the } C_6 \text{ axis,}$$
$$\mu_\perp^+ = 1\cdot 10^{-8}\ \mathrm{cm^2/V\cdot s}\text{—in a direction perpendicular to the } C_6 \text{ axis.} \qquad (1)$$

Such a large difference (a factor of 200) in the mobilities was an unexpected result. We recall that the hexagonal close-packed structure of helium crystals corresponds most accurately, compared with all other substances, the model of close-packed spheres.

To prove that there are no ancillary effects, we measured the mobility as a function of the angle between the direction of the electric field and the C_6 axis. The general relation between the velocity of charges and the intensity of the field on the linear section of the curve $v(E)$ has the form

$$v_i = \mu_{ik} E_k . \qquad (2)$$

It is easy to show that the dependence of the mobility on the angle φ between the C_6 axis and the direction of the electric field in this case is described by the formula

$$\mu(\varphi) = \mu_\parallel \cos^2\varphi + \mu_\perp \sin^2\varphi . \qquad (3)$$

The mobilities of positive charges measured for three intermediate values of the angle φ (25°, 60°, and 81°) demonstrated excellent agreement with the formula (3). Therefore the observed sizable mobility anisotropy is indeed a property of the positively charged complexes in hcp ^{4}He crystals.

The field dependences of the velocity of positive charges presented in Fig. 2 differ not only by the values of the mobility but also by the behavior of the velocity in strong fields. The curve $v_\parallel^+(E)$ demonstrates a clear maximum at $E \simeq 3.5\cdot 10^4$ V/cm, whereas in the investigated range of fields $v_\perp^+(E)$ is a monotonically increasing function, corresponding to an exponential or a power-law function with a large exponent ($\geqslant 9$).

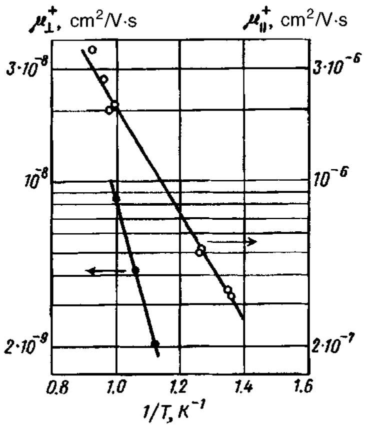

FIG. 3. Temperature dependences of the mobilities of positive charges in the two principal directions: ○ — parallel to the C_6 axis (right-hand ordinate), ● — perpendicular to the C_6 axis (left-hand ordinate).

As noted previously in Ref. 8, the observed nonmonotonic field dependence of the velocity of the charges is explained in Ref. 4 as being the result of phonon-free scattering of vacancies by a charge complex. The threshold electric field intensity corresponds in this case to a situation when in a single scattering event the energy difference between the final and initial positions of the charge complex in an electric field equals the width of the energy band of the vacancy. It is obvious that the phonon-free mechanism becomes impossible in fields above the threshold value. Assuming that the condition $eEu=\Delta$, where e is the electron charge and u is the distance over which the center of the charge complex is displaced in the direction of the electric field as a result of a single scattering event, and Δ is the width of the energy band of the vacancy, holds near the maximum of the curve $v(E)$ and assuming that $u\leqslant a$, where a is the interatomic distance, we can obtain an upper estimate of the width of the vacancy band:

$$\Delta\leqslant 12\text{ K}. \tag{4}$$

We were not able to measure the drift velocity on the linear section of the curve of the velocity versus the field for negative charges. Superlinear growth of the velocity with increasing field is observed in the entire range of fields investigated. About the anisotropy of the motion of negative charges we can only conclude that for the same field intensity their velocity in a direction parallel to the C_6 axis is approximately an order of magnitude higher than in a perpendicular direction. Therefore the ''faster'' direction for negative charges is the same direction as for positive charges.

Besides the results presented above, we also obtained the temperature dependences of the mobility of positive charges in the two principal directions (Fig. 3). For each temperature the value of the mobility was determined according to the slope of the linear part of the curve of the velocity versus the field. The data obtained confirm the thermal-activation character of the charge mobility, satisfying in both directions the relation

$$\mu \propto \exp\left(-\frac{\varepsilon}{T}\right). \tag{5}$$

Here the values of the energy ε are different in the principal directions:

$$\begin{aligned} &\varepsilon_{\parallel}^{+} = 5.3\ \text{K — in a direction parallel to the } C_6 \text{ axis,} \\ &\varepsilon_{\perp}^{+} = 11\ \text{K—in a direction perpendicular to the } C_6 \text{ axis.} \end{aligned} \tag{6}$$

The observed sizable difference in the values of the activation energy has a natural explanation in the Andreev–Savishchev theory.[4] In Ref. 4 it was shown that, depending on the direction of the electric field, the energy ε in Eq. (5) can assume different values in the energy band of the vacancies. Higher mobilities should correspond to lower values of the activation energy; this agrees with the experimental results. We note that the value of $\varepsilon_{\parallel}^{+}$ from Eq. (6) agrees well with previously obtained data[7] on the dependence of the activation energy on the molar volume, confirming its tendency to decrease with increasing molar volume. The value of $\varepsilon_{\perp}^{+}$ is found to be higher than the previously observed values of the activation energy obtained on randomly oriented crystals. As a result of the smallness of the mobility in a direction perpendicular to the C_6 axis, its contribution to the mobility in a given direction (Eq. (3)) is appreciable only for angles φ close to 90°. The probability of obtaining such a sample randomly is quite low. The difference between $\varepsilon_{\parallel}^{+}$ and $\varepsilon_{\perp}^{+}$ can be regarded as a lower estimate of the width of the energy band of the vacancies:

$$\Delta \geqslant 5.7\ \text{K}. \tag{7}$$

We note that the relation (7) together with Eq. (4) comprise an interval of possible values of Δ which agrees qualitatively with the theoretical estimates.[5] Additional data on the structure of a charge complex are required in order to determine Δ more accurately.

In summary, the main result of the present work is the discovery of a strong anisotropy of the mobility of positive charges in ^{4}He crystals and a determination of the activation energies of their mobility in the principal crystallographic directions. It should be noted that the experimental samples were grown under completely different conditions and by a different method[13] than in all previous works (Refs. 7–9; see also Ref. 5). Nonetheless, the absolute values of $\mu_{\parallel}^{+}$ and $\varepsilon_{\parallel}^{+}$ agree well with the previously obtained data. This fact, together with the data on the diffusion of impurity atoms, in our opinion serves as another argument in favor the vacancy mechanism of charge mobility and makes it possible to rule out the presence of nonequilibrium oriented defects (dislocations, twinning boundaries, and so on) in the crystal as a cause of the observed anisotropy. In this case, such a sizable anisotropy can be explained only at the microscopic level taking account of the structure of the charge complexes, to determine which the charge velocity anisotropy must be investigated in strong electric fields.

This work was supported by the Russian Fund for Fundamental Research (Grants 93-02-2551 and 96-02-16348a) and the French Ministry of Higher Education and Research (Grant 94 R 0043).

[1] R. A. Ferrel, Phys. Rev. **108**, 167 (1957).
[2] C. G. Kuper, Phys. Rev. **122**, 1007 (1961).
[3] K. R. Atkins, Phys. Rev. **116**, 1339 (1959).
[4] A. F. Andreev and A. D. Savishchev, Zh. Éksp. Teor. Fiz. **96**, 1109 (1989) [Sov. Phys. JETP **69**, 630 (1989)].
[5] A. I. Dahm in *Progress in Low Temperature Physics*, edited by D. F. Brewer, X, 1986.
[6] A. F. Andreev and A. É. Meĭerovich, Zh. Éksp. Teor. Fiz. **67**, 1559 (1974) [Sov. Phys. JETP **40**, 776 (1975)].
[7] K. O. Keshishev, Zh. Éksp. Teor. Fiz. **72**, 521 (1977) [Sov. Phys. JETP **45**, 273 (1977)].
[8] A. I. Golov, V. B. Efimov, and L. P. Mezhov-Deglin, Zh. Éksp. Teor. Fiz. **94**, 198 (1988) [Sov. Phys. JETP **67**, 325 (1988)].
[9] S. C. Lau, A. J. Dahm, and W. A. Jeffers, J. de Phys. **39**, C6-86 (1978).
[10] O. A. Andreeva and K. O. Keshishev, JETP Lett. **46**, 200 (1987).
[11] K. Keshishev and O. Andreeva, NATO ASI Ser. B: Physics **257**, 387 (1991).
[12] K. O. Keshishev, A. Ya. Parshin, and A. V. Babkin, Zh. Éksp. Teor. Fiz. **80**, 716 (1981) [Sov. Phys. JETP **53**, 362 (1981)].
[13] K. O. Keshishev, A. Ya. Parshin, and A. I. Shalnikov, *Soviet Scientific Reviews*, Section A edited by I. M. Khalatnikov, Physics Reviews **4**, 155 (1982).

Translated by M. E. Alferieff